University of Bath

PHD

Automated and Defect-free Forming of Complex Composite Parts with Machine Learning

Jagpal, Rajan

Award date:
2022

Awarding institution:
University of Bath

Link to publication

Alternative formats
If you require this document in an alternative format, please contact:
openaccess@bath.ac.uk

Copyright of this thesis rests with the author. Access is subject to the above licence, if given. If no licence is specified above, original content in this thesis is licensed under the terms of the Creative Commons Attribution-NonCommercial 4.0 International (CC BY-NC-ND 4.0) Licence (https://creativecommons.org/licenses/by-nc-nd/4.0/). Any third-party copyright material present remains the property of its respective owner(s) and is licensed under its existing terms.

Take down policy
If you consider content within Bath's Research Portal to be in breach of UK law, please contact: openaccess@bath.ac.uk with the details. Your claim will be investigated and, where appropriate, the item will be removed from public view as soon as possible.

Download date: 02. Dec. 2022

AUTOMATED AND DEFECT-FREE FORMING OF COMPLEX COMPOSITE PARTS WITH MACHINE LEARNING

RAJAN JAGPAL

A THESIS SUBMITTED FOR THE AWARD OF DOCTOR OF PHILOSOPHY

UNIVERISTY OF BATH

DEPARTMENT OF MECHANICAL ENGINEERING

April 2022

COPYRIGHT

Attention is drawn to the fact that copyright of this thesis rests with the author and copyright of any previously published materials included may rest with third parties. A copy of this thesis has been supplied on condition that anyone who consults it understands that they must not copy it or use material from it except as licenced, permitted by law or with the consent of the author or other copyright owners, as applicable.

ABSTRACT

Non-crimp fabric (NCF) composites are increasingly regarded as a viable alternative to pre-impregnated composite materials. Favoured for their ability to streamline productivity, whilst offering comparable mechanical properties, these materials are first formed and subsequently infused with a resin matrix. Drape forming processes are typical in production, yet, offer little opportunity to influence deformation. Existing research in the area has focused on laboratory scale processes, with very little work looking at scalability for industrial parts. These concerns not only decrease productivity, but create inflexibility in the design and manufacture of composite components. Coupled with the continuous development of new NCFs, industry demands processes that are adaptable, scalable and purpose-built for predictive modelling.

This thesis first considers the deformation mechanics of a complex NCF, interply shear stiffness, intraply shear stiffness and out-of-plane bending stiffness. Here, the presence of a "veil" layer revealed important characteristics that further exacerbated the material anisotropy. Subsequently, an FEA model using coupled shell and membrane elements was validated. This macroscale model allowed efficient designation of in- and out-of-plane properties via experimental characterisation.

A novel preforming process that can generate in-plane tension through discontinuous blank boundary conditions was established. Distributed Magnetic Clamping allows for highly flexible process control. This method was designed to reduce the human factor in production, and work towards an off-the-roll, intelligent resin transfer system. An efficient two-stage optimisation routine deployed a Gaussian process model for preform deformation, and Bayesian optimisation to find the optimal clamping locations. Results demonstrate that surrogate modelling is viable for magnetic distributed clamping. This lays the foundation for the development of large, translatable data sets that can maximise the impact of statistical tools.

Finally, productivity requirements motivate industrialists to form multiple plies in one stroke. Therefore, DIMAC was employed to experimentally investigate the

feasibility of multiple-ply preforms. An increased number of biaxial plies formed in one stroke was possible through DIMAC, after using the key insights developed through predictive modelling and single-ply experiments. Similarly, the process was able to influence individual ply deformation for stacks with diverse fibre orientations toward the goal of high-rate manufacture.

ACKNOWLEDGEMENTS

It would not have been possible to produce this thesis without the support, guidance and time of so many people. From the beginning, my entire supervisory team inspired me - Thank you. My lead supervisor, Dr Evros Loukaides, never failed to motivate me, allowing me freedom to explore whilst reining me in when it was needed! To Dr Evangelos Evangelou, I am grateful for your expertise and guidance, without which my appreciation for Bayes' theorem would not be the same. I would also like to thank Prof Richard Butler for his steadfast rigour and ability to always see the missing link. Finally, Dr Andrew Rhead, who whilst he wasn't officially my supervisor, was always available for advice and support. Thanks also goes to Prof Prasad Potluri and Dr Fulvio Pinto for their enthusiasm for the project and constructive feedback during my VIVA. A further mention should also be given to Prof Tim Mays and Dr Yanki Keleş for encouraging me over the finishing line.

The technicians, Clare Ball, Steve Thomas, Mark Wellman, Dave Wood and Guy Brace were pivotal in realising the experimental work and also allowed me to sound out my crazy ideas. Clare also encouraged me to not only apply for the PhD, but was always around for a chat. Similarly, the members of the composites research group, in particular Tomas, Lucie, James, Carl, Sophie, Jean, Thomas, Jay and Yang, who always filled the office with good humour. I would also like to extend my appreciation to Prof Michael Sutcliffe, Dr Lee Harper and the wider NCForm - CIMComp group, for all the lively discussions about NCFs. Special mention to GKN Aerospace for not only part sponsoring this project (and me), but for providing sound industrial context and advice. I would also like to thank EPSRC and UKRI for funding this work under the National Productivity Investment Fund.

I am forever grateful to the residents of Abbeyfield, The Plaza and Privet, honorary and none, who would have thought it! To my friends in York, who never failed to make me feel at home and supported me without question, thank you. To my partner George, your ability to make me laugh when work got too much, your keen eye when reading endless drafts, your faith that I could do this, wow.

Finally, at the age of 14 my Dad came to the UK alone and with almost nothing to his name. He always believed in me, but passed just before I started university. This PhD is dedicated to his memory and the notion that anything is possible even if it is improbable. To my Mum, Dad, Bruce, Anecia and each one of the Jagpal/Raju/Perry clan, family is eternal and you have all given me the opportunities, experience, love and selfless encouragement to make me who I am. This is for you.

DECLARATION

I declare that the work in this thesis was carried out in accordance with the requirements of the University's Regulations and Code of Practice for Research Degree Programmes and that it has not been submitted for any other academic award. Except where indicated by specific reference in the text, the work is the candidate's own work. Any views expressed in the thesis are those of the author.

PUBLICATIONS

Publications linked to this work:

I. Jagpal R, Butler R, Loukaides EG. Towards flexible and defect-free forming of composites through distributed clamping. Procedia CIRP. 2019;85:341-6 https://doi.org/10.1016/j.procir.2019.09.008.

II. Jagpal R, Evangelou E, Butler R, Loukaides EG. Preforming of non-crimp fabrics with distributed magnetic clamping and Bayesian optimisation. Journal of Composite Materials. 2022;56(18) https://doi.org/10.1177/00219983221103637.

III. Jagpal R, Evangelou E, Butler R, Loukaides EG. Multiple ply preforming of non-crimp fabrics with distributed magnetic clamping. Composite Communications. 2022;101107 https://doi.org/10.1016/j.coco.2022.101107.

Publications outside the main scope of this work:

IV. Chen Y, Jagpal R, Loukaides EG. Assessment and case studies of UAV photogrammetry for manufacturing applications. International Journal of Mechatronics and Manufacturing Systems. (Submitted).

V. Culliford LE, Scarth C, Maierhofer T, Jagpal R, Rhead AT, Butler R. Discrete Stiffness Tailoring: Optimised design and testing of minimum mass stiffened panels. Composites Part B: Engineering. 2021;221:109026 https://doi.org/10.1016/j.compositesb.2021.109026.

VI. Neville GM, Jagpal R, Paul-Taylor J, Tian M, Burrows AD, Bowen CR, Mays TJ. Freeze casting of porous monolithic composites for hydrogen storage. Materials Advances. 2022. https://doi.org/10.1039/D2MA00710J

CONTENTS

Chapter 3

Chapter 4

Chapter 5

Chapter 6

Chapter 7

Chapter 8

Chapter 9

ABBREVIATIONS

NCF	Non-crimp fabric
ML	Machine learning
UD	Unidirectional
Prepreg	Pre-impregnated fibres
EVaC	Engineered vacuum channel
OoA	Out-of-autoclave
VBO	Vacuum bag only
RTM	Resin transfer moulding
CRTM	Compression resin transfer moulding
RFI	Resin film infusion
VARTM	Vacuum assisted resin transfer moulding
RIFT	Resin infusion over flexible tooling
DDF	Double diaphragm forming
SDF	Single diaphragm forming
HDF	Hot drape forming
RTI	Resin transfer infusion
SCRIMP	Seemann composites resin infusion moulding process
DF	Drape forming
PJN	Pin jointed net
DIC	Digital image correlation
AFP	Automated fibre placement
ATL	Automated tape laying
ANNs	Artificial neural networks
BHF	Blank holder force
FBH	Full blank holder
FMH	Full magnetic holder
BCs	Boundary conditions
XRCT	X-ray computed tomography
OS	Offset
QI	Quasi-isotropic
GP	Gaussian process
DIMAC	Distributed magnetic clamping

CHAPTER 1

INTRODUCTION

Carbon fibre composites have long been chosen for their advantageous in-plane material properties, relative to metals, in the aerospace, naval, automotive and energy industries. With much of the research effort to date focused on pre-impregnated materials, a new move towards utilising dry fibre is apparent. Dry fibre composites are a viable alternative to decrease production cycle times, through the absence of time consuming manufacturing processes. Manufacture of dry fibre components is split into two phases: preforming, where the material is deformed over a target geometry, and infusion, where the resin matrix is added. The research effort of this work is focused on the former. Within the category of dry fibre composites, exists the distinct category of non-crimp fabrics (NCF). NCFs are desired for their low density over comparable woven fabrics, due to their construction that keeps fibres in-plane.

In the aerospace domain many different products can exploit these properties, with wing spars being one example. Often, complex double curvatures, such as ramps and recesses, are present. This necessitates large shear deformation to produce parts free of defects. The literature surrounding NCFs can often simplify the complex material system, which can include layers of randomly orientated fibre mats and diverse stitching. Characterisation work on NCF materials is often not covered by specific standards and is costly to undertake, with each design and change of material requiring new validation. Engineers are limited by experience and simplified academic preforming studies. This creates inflexibility in the production cycle.

Manufacture too has suffered from a lack of standardisation, with numerous protocols developed. Accordingly, composite part production still struggles to reach truly high-rate manufacture. Complex geometrical features remain challenging to produce, leaving manual processes to dominate production. Drape forming has offered the most promise to date towards reduced cycle times and flexible tooling. However, drape forming processes offer little opportunity to control boundary conditions, greatly reducing the flexibility to influence the deformation and react to process-induced defects. The US Department of Energy's Advanced Manufacturing Office [1] interviewed key manufacturers and found five key barriers to composite manufacture: high speed production, low cost production, energy efficient manufacture, recycling technologies, and innovative design concepts. This provides motivation to increase the flexibility of production processes, providing new forming protocols that can be applied to complex material systems and different geometries. Further, by developing optimised protocols, production speed could be increased, at the same time as reducing costs and facilitating more innovative design downstream.

Continuous development of material systems and product geometries demand a solution that is highly repeatable, has adaptable process control measures, is translatable to different materials and offers process flexibility at different length scales. Despite the complexity of NCF materials, their architectures typically result in orthotropic properties and distinct energetically-favourable deformation modes. Hence, there is an opportunity to improve formability through tailored control of boundary conditions during forming operations.

Machine learning is one powerful approach to optimisation. The application of these predictive modelling tools has also surged, thanks to modern computational power and new methodology/algorithms. Techniques such as Bayesian optimisation facilitate efficient evaluation of the objective function, compared to conventional stochastic methods, balancing exploration and exploitation of the search domain. It is proposed that through using increasingly-accessible methods, production of composite parts can also be optimised.

This thesis therefore aims to investigate novel forming controls using statistical methods. Leading to the development of new methodologies to create defect free parts, with higher productivity. Initially, characterisation of a complex NCF investigates the effects of additional components such as toughening veils and binding agents. The study also serves to highlight the multi-scale nature of the material, preceding the development of an efficient macroscale FE model. A virtual model of the material develops the major mechanical properties elucidated through characterisation, including non-linear shear behaviour and transverse bending stiffness. In order to achieve the main objectives of this thesis, a novel forming process is also propositioned, Distributed Magnetic Clamping (DIMAC). Addressing many of the considerations of process flexibility, DIMAC is compared to its closest comparators and validated against benchmark processes. In order to harness the potential of the method, Bayesian optimisation and Gaussian process modelling techniques are developed for use in preforming and validated against experimental results. Finally, a parametric study harnessing the DIMAC platform for multiple ply preforming, indicative of industrial needs, is conducted and an adjusted metric for preform quality is developed.

1.2 SCOPE AND OBJECTIVES

The main scope of this thesis is therefore to develop novel forming controls through statistical methods, creating defect free parts with higher productivity. This will be achieved through characterising the material system, fundamental forming behaviour, and to look at the interaction of the material with geometry. Culminating in the implementation of machine learning algorithms that will develop a flexible approach

to boundary condition generation for complex geometries. Thus, the objectives for this research effort are summarised in the following:

1. To characterise, for the first time, a complex carbon NCF fabric and investigate the influence of additional reinforcements and stitching.

2. To design and implement a robust and efficient FE model that reproduces the characteristics of a novel veiled NCF, incorporating transverse bending as well as non-orthogonal shear behaviour.

3. Develop repeatable active boundary condition controls for forming. This should aim to tailor the production process to geometry and be viable at a range of production scales.

4. Implement machine learning as a predictive tool to efficiently provide global optima in process optimisation, and to increase the learning shared across different material and geometrical choices.

5. To develop preforming methodology that can form multiple ply layups to increase the rate of production.

The objectives are also mapped on to *Figure 1.1,* which shows a flowchart of the thesis structure. Secondary arrows connect Chapter 6 and Chapter 8 with the literature review, as developing flexible boundary control methodology and processes for multiple ply preforming was a key industrial demand. Similarly, Chapter 4 influences the boundary condition choices in Chapter 8, and the FE model developed in Chapter 5 is directly used as the basis for Chapter 7.

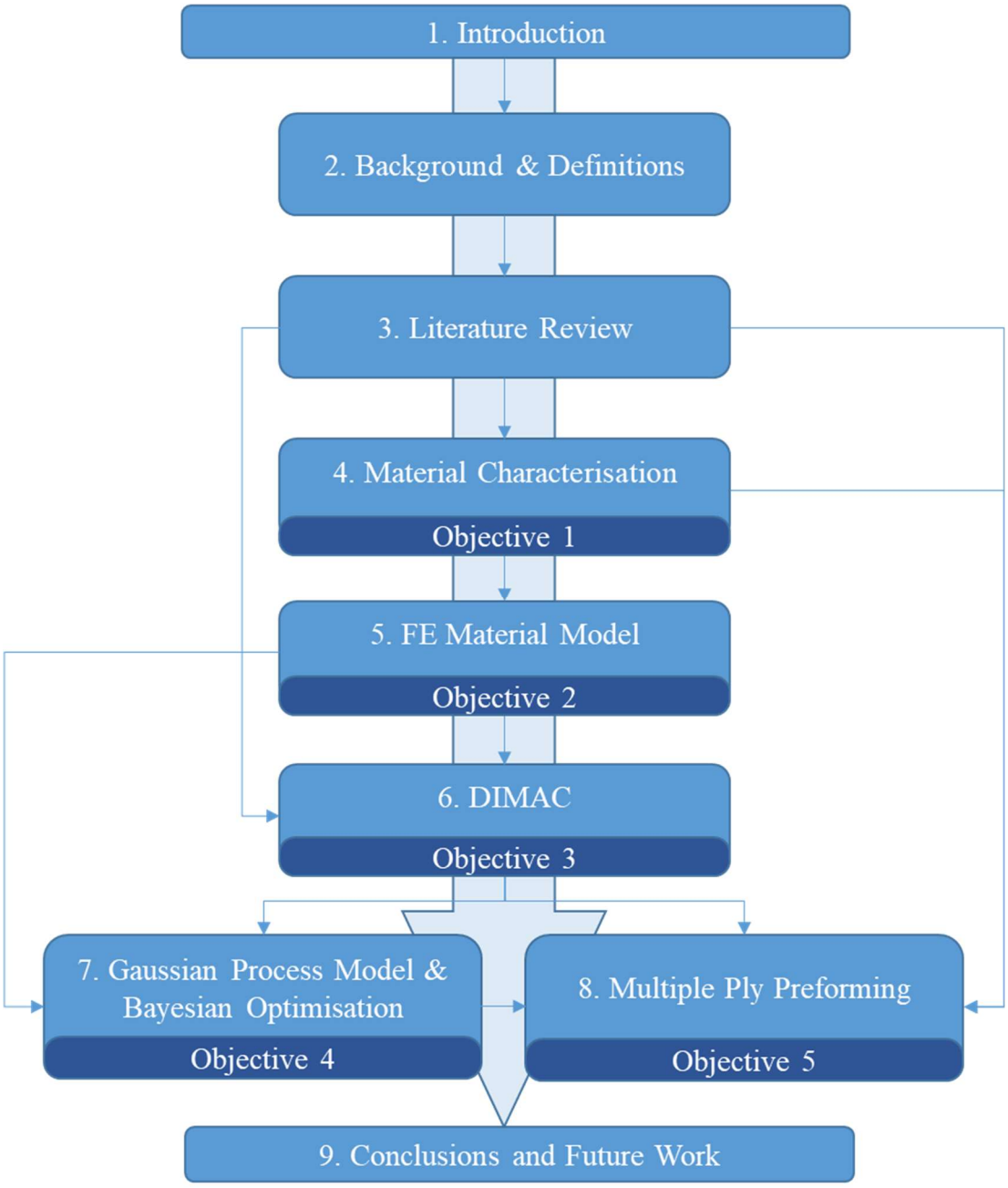

Figure 1.1: Flowchart of thesis structure, highlighting the primary order of the thesis and key secondary connections between chapters. The objectives discussed previously are also mapped to the relevant chapters.

1.3 MAJOR CONTRIBUTIONS

The major contributions of this thesis are summarised as:

- An in-depth investigation of the major deformation characteristics for a veiled biaxial carbon non-crimp fabric was performed for the first time. This included an evaluation of interply shear, intraply shear, transverse bending and a microscopic analysis of the material.

- The proposition of a novel preforming process: Distributed Magnetic Clamping (DIMAC). Which is the first example of deploying permanent magnets for boundary control manipulation. Designed to work towards an intelligent, automated, resin transfer system (RTM), the process allowed adjustment of local material boundary conditions. Developed and validated through experimental parametric studies, DIMAC demonstrated capability in generating diverse preforming data sets, for both single and multiple ply preforming strategies. Magnets were shown to be highly advantageous in material boundary condition control and offer many operational benefits to industrialists and academics.

- Implementation and validation of an efficient virtual macroscale modelling framework that included transverse bending properties in Abaqus. The material model used membrane elements to capture the non-linear shear stiffness behaviour, with coupled shell elements providing the bending stiffness. This represents a computationally efficient solution, with most previous examples of global process optimisation only capable of using membrane models, due to the added computational cost of bending.

- Development of predictive tools that demonstrated the capabilities of DIMAC. This was achieved through a Gaussian process model surrogate, to estimate defect magnitude, and non-parametric Bayesian optimisation, to find the optimal boundary conditions. This is the first known example of Bayesian optimisation for global process optimisation in the composite forming literature.

1.4 THESIS OVERVIEW

This thesis is divided into eights chapters. Excluding the introduction, the seven remaining chapters are structured as follows:

Chapter 2: Background and Definitions

As this work encompasses a juncture between many active areas of research, the key background and definitions found within the literature are first discussed.

Chapter 3: Literature Review

A comprehensive literature review is presented. This first considers the complexities of NCFs, before evaluating the mechanical properties and characterisation methodologies. The review also evaluates the current state-of-the-art in automated manufacture and the application of machine learning to forming.

Chapter 4: Material Characterisation

This chapter characterises the key mechanical properties of a complex non-crimp fabric. A microscopic analysis reveals key, yet often overlooked, characteristics of the stitch, veil and binder. Bias extension tests evaluate the NCFs non-linear shear stiffness and cantilever tests assess the transverse bending properties.

Chapter 5: FE Material Model

Subsequent to the material characterisation, an efficient macroscale homogenisation procedure for the material is implemented in *Abaqus*. This utilised shell elements to capture the transverse bending property and membrane elements to facilitate non-linear shear stiffness. Through adjustment of the constitutive relations, in-plane and bending stiffnesses are decoupled. The model is validated using elementary tests and against the experimental results for both bias extension and cantilever testing.

Chapter 6: Distributed Magnetic Clamping

In this chapter, the novel preforming process, Distributed Magnetic Clamping is presented. An initial scoping study explores the feasibility of using magnets to alter the local boundary conditions of the material during forming. A subsequent analysis of

DIMAC for single ply preforming of complex geometries is discussed and experimental findings are developed to include a metric for preform quality.

Chapter 7: Gaussian process model and Bayesian optimisation

Initially, a parametric FE model that replicates the DIMAC process is developed, with the FE material model in *Chapter 5,* to create a virtual framework. A robust validation of the virtual framework is undertaken, with comparison to the experimental findings in Chapter 6. A two-stage virtual optimisation procedure is implemented for the optimisation of DIMAC. This includes the development of a Gaussian process model that acts as a surrogate to estimate preform quality and Bayesian optimisation to find the optimal magnet configuration. These techniques are first discussed and subsequently validated.

Chapter 8: Multiple ply preforming

To further verify the capabilities of DIMAC and scope the benefits of such a process, *Chapter 8* presents an extension of the process to multiple ply preforming. First, the major considerations for high-rate manufacture are discussed. The metric for preform quality, developed in Chapter 6, is adjusted to facilitate the comparison of preforms with different numbers of plies. Multiple ply preforming is further assessed against a benchmark to highlight the benefits of such a system. Subsequent experimental analysis is undertaken for a range of strategies towards high-rate manufacture: increasing the number of equivalent biaxial plies, increasing the blank holder force, varying magnet placement and varying fibre angles.

Chapter 9: Conclusions and Future Work

This chapter critically considers the work carried out in this thesis and presents the final conclusions, culminating in suggestions for future work.

CHAPTER 2

BACKGROUND AND DEFINITIONS

This chapter introduces carbon fibre composites and the definitions found within the literature. The subsequent discussion introduces and discusses the most commonly used fibre systems, building to a more detailed evaluation of NCFs and their production. Geometry and how it influences the theoretical understanding of fabric forming is also discussed, before a brief introduction to machine learning (ML).

2.1 CARBON FIBRE COMPOSITES

Fibre reinforced composites offer a multitude of advantages. Chosen for their impressive strength to weight ratio, they consist of a fibrous material embedded into a matrix system. In the aerospace domain, carbon fibres are typically used for the structural elements, with boron, aramid and glass fibres also employed. This thesis focuses on carbon fibres. These fibres have a high strength and modulus of elasticity and are the predominant load-carrying element in the composite. The matrix, typically a polymer, serves to hold the fibres in their desired orientation and to transmit load between the fibres. Two main divergent categories exist within composite fibres: continuous fibres and discontinuous fibres. Discontinuous fibres can be further subdivided, with typical examples such as chopped fibre mats and particulate fibres commonly used. For the purposes of this thesis, only continuous fibres will be discussed. Continuous fibres are the most frequently used in the aerospace sector due to their excellent load-carrying properties. These continuous fibres can be orientated in distinct orientations depending on the chosen system, with unidirectional (UD) fibres arranged in a single orientation. Typically, through stitching, weaving or bonding, further orientations can also be added.

2.2 PRE-IMPREGNATED COMPOSITES

Pre-impregnated fibres (prepregs) were developed to assist in the production process, with a single ply consisting of fibres sandwiched between two resin films. This allows a specific volume-fraction of the polymer matrix to be pre-administered onto the fibres, which facilitates better resin uniformity post cure. These resin films are generally tacky at room temperature with a viscosity high enough to remain adhered to the outer fibres in the ply. A schematic and micrograph image of a vacuum-bag-only (VBO) prepreg system, *Figure 2.1*, highlights the resin films surrounding the fibres with the dry central area referred to as the engineered vacuum channel (EVaC).

Through this tackiness, large ply stacks can be fabricated and fixed in place on moulds until curing is required. Under elevated curing temperatures and typically elevated pressure, the resin films reduce in viscosity, allowing its flow through to the

dry fibre areas in the middle of the prepreg. Whilst prepregs were first developed to increase the ease of manufacture, several drawbacks exist that are inherent to this material system. Centea *et al.* (2015) [2] identified three major areas within the literature that reduce the ability of prepregs to form defect free parts: high porosity resulting from inconsistent resin wetting or low applied pressures [3, 4] , quick out-times; the time prepregs can be kept at room temperature (~1 week) [3-5] and significantly lower performance, specifically toughness [3, 6]. Many of these issues relate to porosity. In response, out-of-autoclave (OoA) resins were developed that decreased these negative attributes in vacuum bag only (VBO) prepregs. These prepregs exploit larger areas of dry fibre in the EVaC to allow air channels from which vacuum pressure can be drawn to facilitate increased fibre wetting, in conjunction with developments in resin chemistry to reduce porosity in the parts. Whilst these efforts increased the viability of prepreg materials, the issue of quick out-times remains. Prepregs require storage in a freezer and can generally only be stored at -18 °C for around six months [5], with limited shelf life of the resins, and stringent controls required to ensure high quality material. Through production, the resins also need to be allowed to release any gases to avoid further voids through the cured part, a process called debaulking, adding further production time to the process. Coupled with their inability to be kept at room temperature for more than a limited time frame, the process is costly, thwart with complexity and wastage.

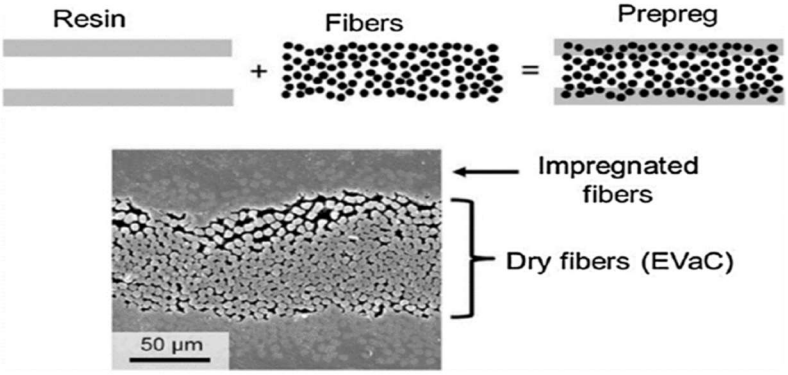

Figure 2.1: Schematic and micrograph image showing the prepreg system consisting of a central band of fibres encapsulated by two resin films with a transition from resin layer, impregnated fibres and finally dry fibre. Image from [2].

One more recent development in the industry is to push towards dry fibre preforms, rather than prepregs [7] that aim to address the concerns identified by Centea *et al*. (2015). This allows the highly sensitive resin system to be infused after fixing dry fibres in their desired orientation, generally through a process of preforming.

2.3 DRY FIBRE FABRICS

With the push to reduce cycle times and an overwhelming drive to increase automation, dry carbon fibre fabrics are increasingly seen as a viable alternative to prepreg systems. Without the inclusion of resin, dry carbon fibre resembles a traditional fabric, albeit of significant stiffness, that is then moulded into the desired geometry. After this process the fabric is infused with the resin matrix to create the composite system [8]. These fibres can then be bundled together to form single dry fibre tows, which can then be fed into a robotic applicator for automated fibre placement (AFP) manufacture, which is sometimes termed automated dry fibre placement (DFP). Whilst this method allows for relative freedom in steering fibres onto a mould, the process is slow and therefore not suited to large-scale automation or production.

In an effort to increase production rates, fabrics have been developed that allow greater amounts of material to be placed in quicker cycle times. How these tows are aligned and fixed together is the main variant in the classification of different dry fibre fabrics. The main fabric material systems are woven and non-crimp fabrics (NCF). Woven carbon fibre fabrics are not dissimilar to a typical woven fabric. They consist of orthogonal fibres 90° to each other which are termed warp and weft directions, woven together to form the fabric. Typically developed from the textile industry, there are many weave patterns, however the three most common types are identified in *Figure 2.2*. What is evident is that the tow must deviate from the plane and curve around the opposing warp or weft tow, a property called crimp. The level of crimp the tow undergoes significantly affects the final material properties, where ideally carbon fibres would remain in-plane to allow for the most efficient transfer of load [9, 10]. The difference between the total un-crimped length of the fibre tow and the length of the tow when woven is defined as the crimp, as described by *Figure 2.3*. Largely the weave type also affects the percentage of crimp present in the fabric, with plain weaves having

the greatest and high order satin weaves having relatively lower levels of crimp [11]. Not only does crimp affect the in-plane properties of the material, it can also negatively affect its intraply shear properties and thus its formability. This means that for a wide variety of aerospace applications, woven fabrics are unsuitable, as the fibres are not optimised for in-plane load transmission, increasing the amount of material needed for a given scenario. As described in the previous section, UD prepregs are also costly and time consuming to produce, this coupled with reduced mechanical properties in woven dry fabrics as a result of crimp, has led to the development of a new class of dry fibre fabrics. Termed non-crimp fabrics (NCFs), these systems have all of the benefits of woven fabrics, namely their ability to be stored at room temperature indefinitely, increased formability and drapeability, without the disadvantageous crimp. Through constructing the fabric without crimp, mechanical properties inline with prepregs can be reached, offering a balanced solution.

Figure 2.2: Examples of three major weave patterns with the corresponding degree of crimp highlighted [11].

$$percantage\ crimp = \frac{total\ length\ of\ fibre\ bundle - length\ of\ bundle\ in\ fabric}{length\ of\ bundle\ in\ fabric} \times 100$$

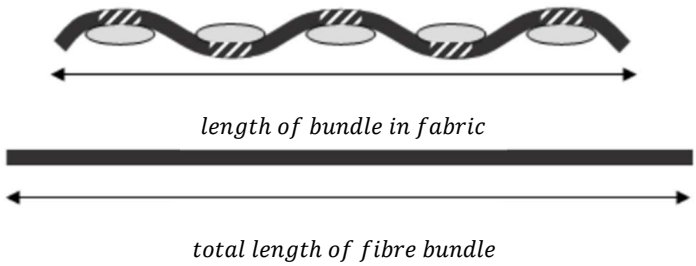

Figure 2.3: Schematic of fabric crimp using a cross sectional view of plain woven fabric and highlighting the corresponding calculation of percentage crimp, adapted from [9].

2.4 NCF MATERIALS

Non-crimp fabric or NCFs have seen rapid development in recent years. Desired for their optimised weight reduction in comparison to woven fabrics, as well as their ease of manufacture, several variations of the material system exist. Typically categorised based on the method of fixation and the number and orientations of fibre tows, Schnabel and Gries (2011) [12] illustrate the different forms of NCFs, shown in *Figure 2.4*.

In the aerospace sector warp knitted NCF, in the required number of axes, are typically used. In its most simplistic form, UD tows are stitched together with a stitching yarn, usually made from polyester or nylon. This stitch pattern gives the fabric structural integrity without significantly compromising the orientation of the fibres, alleviating the requirement for crimp. These UD tows can further be developed to biaxial NCFs where orthogonal tows are placed on top of one another and then stitched in the through thickness direction in the same manner as UD NCFs. Multiaxial NCFs are a further iteration, where multiple UD tows are placed on top of each other in the desired orientations and follow the same process. *Figure 2.5* highlights the fabrication of a multiaxial NCF, with biaxial and UD NCFs utilising the same construction with the relevant number of layers. The warp knitting process involves a roving needle penetrating the fibre tows and forming loops as the fibre tows are moved forward, holding the structure of the fabric. Further designations are found in the literature to distinguish between the most common commercially available NCFs, with biaxial versions with fibres in the 0° and 90° directions referred to as L and T, given the longitudinal and transverse fibre directions [13, 14]. Biaxial NCFs, whose fibres are ± 45° are termed DB or ‘double bias’ and can also be referred to as bidiagonal by manufacturers. Following the same protocol multiaxial fabrics can also be distinguished as LTDB, owing to their construction of varying different angles, most typically 0°, 90°, ± 45°.

Warp knitted NCFs are constructed from three subcategories of thread systems: pillar threads, 0°, weft threads, 90°, and warp-knitting yarns [15]. The pillar thread travels in the through thickness between the tows, whilst the weft threads are the diagonal to the process direction, with the warp-knitting yarns used to fix the two

threads at their intersection. A further addition to the material system, identified in *Figure 2.5*, is a chopped strand mat which is a non-woven material stitched into the assembly to increase fracture toughness and resin wetting.

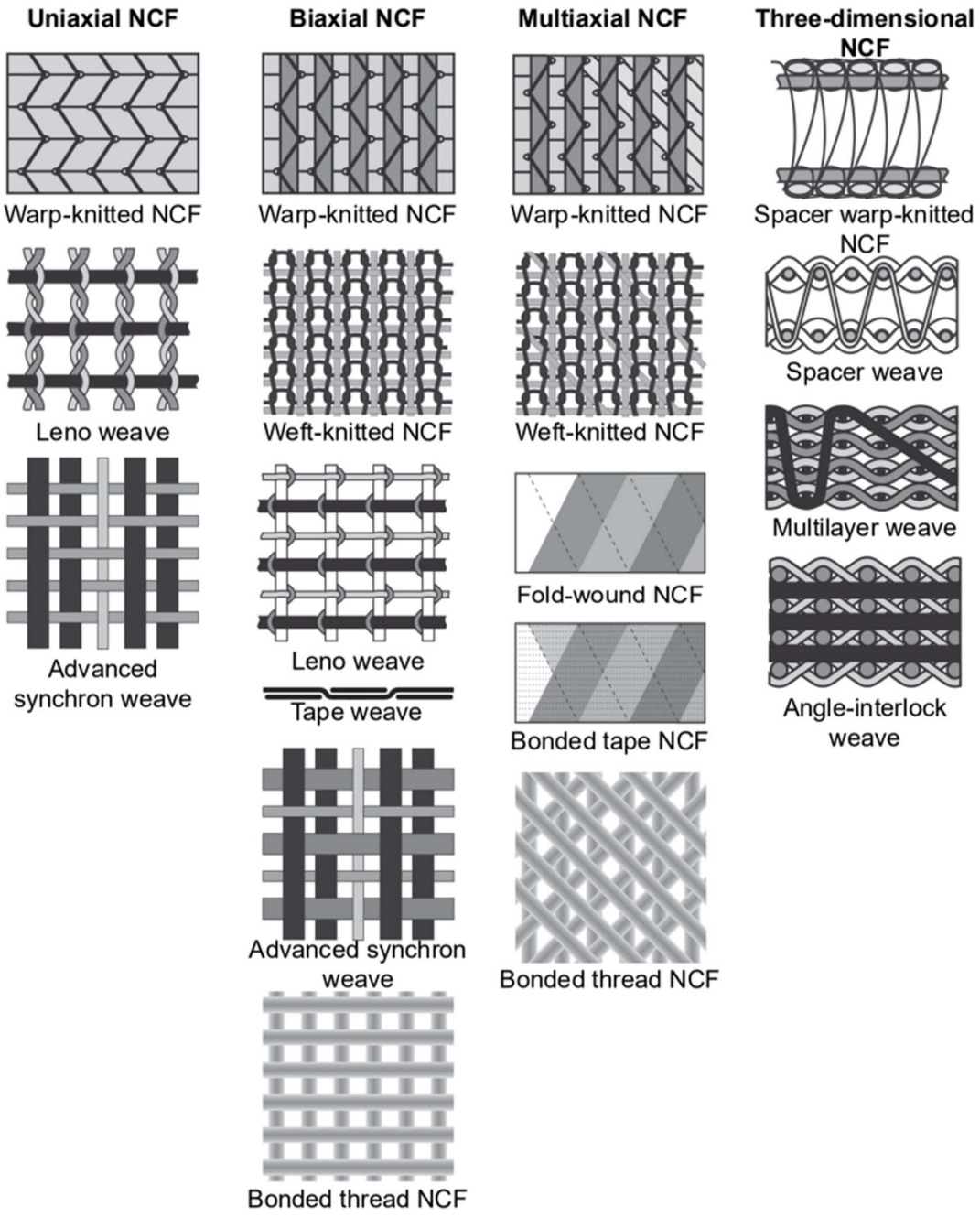

Figure 2.4: Common types of fabric [12], with warp knitted biaxial fabrics the focus of this thesis.

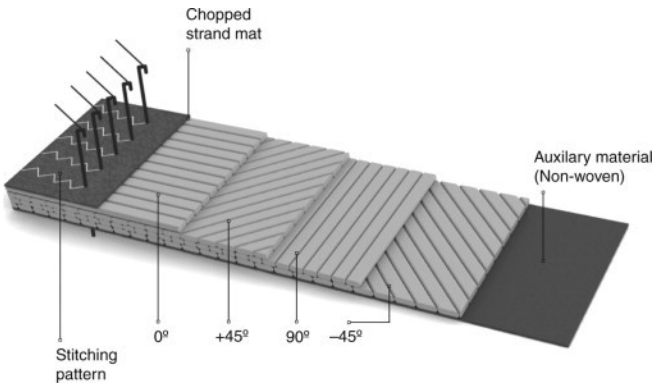

Figure 2.5: Warp knitted multiaxial NCF construction, highlighting the different fibre orientation fixed together through a stitching pattern [15].

2.5 FORMING

The main forming processes that relate to the production of NCF components are discussed in this section. Manufacture, and its increased throughput, was identified in the previous section as one of the primary drivers to the development of NCFs. Through discussing the most common production methods used within NCF manufacture, the background and terminology of NCF manufacture will be introduced. Manufacturing of NCFs has its roots in hand lay-up, a labour intensive process that is commonly used in the architectural, aerospace, automotive, sports and boat-building industries [9]. Whilst the technique is relatively inexpensive in tooling costs, a significant bias is placed on the skill of the laminator in achieving defect free parts. First, a release agent is applied to the mould tool to assist in releasing the cured part. An optional gel coat can then be applied, giving the final part a better surface finish, before NCF fabric is manipulated over the tool into a desired location. The operator then uses a roller, commonly a nip-roller, to apply the resin and compact the assembly, working out air pockets and voids. This process is repeated for subsequent layers until the desired stacking sequence is reached. The part is then left to cure at room temperature before being removed from the tool.

Whilst this process has been used for many years, inherent disadvantages exist. As mentioned previously, the method is extremely susceptible to the skill of the laminator.

Moreover, the process has many health and safety risks that are increasingly regulated, particularly the emission of hazardous styrene, typically used to reduce the viscosity of the resin to enable easier manipulation by the laminator. Further, as the laminate is cured at room temperature under general atmospheric pressure, consistent volume fractions are difficult to achieve and the resulting damage tolerance of the parts are generally lower than for other methods. This makes this method generally unsuitable for aerospace applications, however it is an important precursor to the evolution of production processes used today. One development of the process that can achieve better part quality, whilst still utilising the advantages, is through the addition of a vacuum bag to assist in the final part consolidation. In this process, the technique employed is comparable to hand lay-up, however through the addition of a release film between the top of the laminate and a vacuum bag, pressures of around 1 atm can be achieved. This not only allows for increased fibre wetting, but also decreases the void content in comparison with standard hand lay-up techniques.

The techniques used in hand lay-up of dry NCFs have not been evaluated in the literature. A unique study looking at the techniques used in the hand lay-up of prepregs is provided by Elkington *et al.* (2015) [16]. Whilst some differences in prepreg and NCF lay-up exist, many of the processes discussed in the work by Elkington *et al.* are transferable to the skills used by NCF hand laminators. Complex tasks were categorised with ascending complexity into: one handed guiding, two handed guiding, manual folding, hoop shearing, double tension shearing, tension-secured shearing, tension and sticking and finally mould interaction shearing. A full description of these tasks is not presented here; the reader is referred to [16] for a compressive assessment. These tasks do however highlight the complexity involved in hand lay-up and the dependency on the laminator in achieving the required material deformation to achieve part quality. This emphasises that for repeatability of parts and quality assurance in the aerospace sector, hand lay-up is not the optimal choice. Ward *et al.* (2011) [17] agree, and discuss the need for more efficient manufacturing processes to reduce costs and increase quality.

In a push to increase efficiency and part quality, NCFs and the wider dry fabric manufacturing processes can be split into two main stages: preforming and forming.

During the preforming stage, a NCF stack is deformed over a mould tool to achieve conformity to the desired geometry, this preform can then be set in place through the activation of the polymeric binding agents discussed in the next sections. This semi-formed structure allows better control of the fibre orientations as the part is fabricated. After the preforming stage, resin is infused over the part, generally but not exclusively, through the use of a vacuum. This increases the level of control over the wetting of the fibres and increases the quality of the final part.

One popular manufacturing technique that is used throughout industry is resin transfer moulding (RTM). In this arrangement, the preform for the part is built up over the female mould tool, this can be either through hand lay-up techniques, or more commonly, through automated robotics which will be discussed in more detail later. The upper male mould is then lowered over the preform to the desired final part thickness, compacting the preform to allow consolidation over the geometry. Resin is next injected under pressure through the mould cavity, wetting the fibres and filling the voids. The part is then cured, depending on the resin system this could be at room temperature or under elevated temperatures through heating the mould. Through this process, high fibre volume fraction can be achieved with reduced void content, as well as the double mould surfaces imparting better surface finishes on the finished part. The method however does mean expensive tooling is required, with tools capable of thermal stability under the elevated curing temperatures. This also makes the process less flexible to changing geometries. A variation of this process is compression resin transfer moulding (CRTM) and follows the same protocol except that the resin is infused in an unpressurised state. Only when the male tool is lowered onto the preform is pressure reached in the system. This allows the resin to infuse over the part and allows for a more uniform part thickness. Full details of this process can be found in [18], which evaluates the full process.

Resin film infusion is a further NCF forming process used in industry. The process involves interleaving NCF plies with resin films in the preform. The entire preform is then vacuum bagged and heated, either through the use of an oven or by heating the tooling. This process is very similar to the production of prepreg materials, with the resin films in the NCF process decoupled from the dry fibre cores. This method,

however, does mean that complex geometries are more difficult to fabricate, as the resin films will not deform in a uniform manner over double curvature. This can mean the final part will have resin-rich zones and the inclusion of voids. In this light, parts fabricated from RFI are typically less complex in design.

Infusion processes have since been developed from RTM that aim to address some of the disadvantages of the process, making it more efficient and cost effective. Many variations exist with the most common, vacuum assisted resin transfer moulding (VARTM), resin infusion over flexible tooling (RIFT), double or single diaphragm forming (DDF/SDF), hot drape forming (HDF), resin transfer infusion (RTI) and Seemann Composites resin infusion moulding process (SCRIMP), with the latter covered under multiple patents. Double and single diaphragm forming are compared in *Figure 2.6-2.7*. These process all bare resemblance to RTM, with the upper mould tool being replaced by some sort of membrane. For the purposes of this work, these processes will be referred to as drape forming techniques (DF). In most examples, this is through using a vacuum bag to allow conformation to the lower mould tool, however further developments have utilised elastomer-based membranes. These membranes were developed to allow for reduced wrinkling on the upper surfaces as the membranes are capable of much larger elastic deformations than standard vacuum bags. By utilising a double diaphragm configuration, further control of the pressure applied to the upper surface can be achieved, facilitating better part quality.

The basic principle of all NCF infusion processes starts with the dry fabric material being laid over the lower mould tool to create the preform. This preform can also undergo binder activation to fix one ply to another to form a stack. A peel ply is placed on the top surface to help in part removal, and also none structural material, typically a honeycomb-like structure or knitted material [19]. This addition helps during the infusion of resin and enables a controlled resin flow over the top surface. The entire assembly is then sealed inside a vacuum bag, or the membranes are lowered to create a vacuum chamber over the tool, before the vacuum is drawn and the part is further consolidated on to the geometry of the mould. Finally, resin is allowed to enter the sealed chamber through a resin pump, and facilitated by the vacuum and the resin

distribution fabric, begins to penetrate the fibres from above. The volume of resin can also be easily tailored in this process by only including adequate resin in the tank.

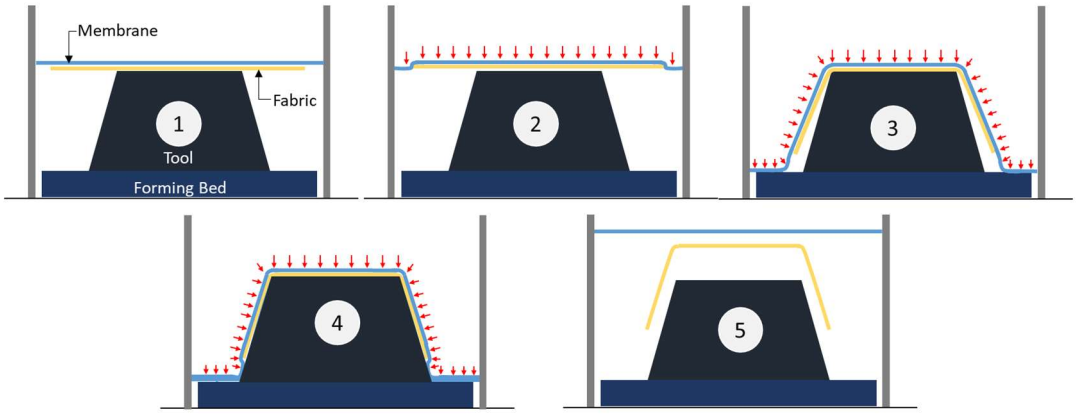

Figure 2.6: Single diaphragm forming schematic stages. 1. Fabric is placed on top of tooling, 2. Vacuum is drawn in forming chamber, pulling the diaphragm in contact. 3. Diaphragm continues to lower over the tooling, typically this first pins the membrane to the forming bed, creating a space between the tooling. This will continue to be evacuated by the vacuum in stage 4, until the part can be removed post-cure, in stage 5.

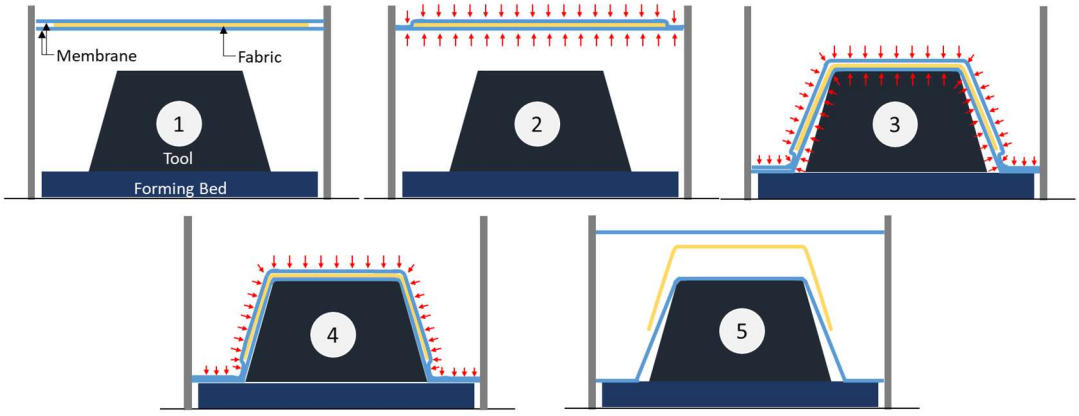

Figure 2.7: Double diaphragm forming schematic stages. 1. Fabric is placed between the two membranes, 2. Vacuum is drawn between the membrane. 3. Vacuum is drawn between the tooling and lower membrane. 5. Diaphragm lowers over the tooling. 6. The part is cured and finally removed

2.6 PROCESS DEFECTS

Inherent to all forming techniques for carbon fibre composites, particularly as a result of complex geometry, is the formation of defects that could reduce the damage tolerance of the cured part [20]. However, biaxial NCFs exhibit a different shear mechanism than that of their woven counterparts, relying on intraply stitching, opposed to the interlacing of the woven fibres [21]. Further, it is understood that tension in the in-plane stitching yarns contributes to the shear resistance of the fabric. As the in-plane stitch orientation in a NCF is often ±45° to the fibre directions, negative and positive shear is induced as a result of the stitches being in compression or tension, respectively, facilitating an unsymmetrical shear deformation. Chen *et al.* (2016) [21] highlight this phenomenon, where positive and negative shear is shown to place the stitches in tension and compression. They describe that through large shear angles inducing large shear strains on the stitching yarns in positive shear, the stitches can fail and cause damage to the fabric architecture.

In negative shear when the stitches are in compression, many of the same modes exist that are present in woven fabrics [22]. The NCF architecture therefore facilitates different formations of defects over woven fabrics. Primary defect mechanisms are in-plane fibre buckling, or waviness, and out-of-plane wrinkling [23]. When forming, shear necessitates that the fibres must compact, reducing the gaps between them, which causes compressive strain on the fibres. The point at which compaction is no longer supported, as the gap has reached its minima, is described as the shear locking angle [21]. Once this is surpassed, out-of-plane wrinkling and compression folding is to be expected. This highlights the major defects during forming, with further defects arising from forming a full ply stack discussed by Lightfoot *et al.* (2013) [20] who looked at corner radii. It was shown that stiffer 0° plies at the outer surface did not allow conformity into a recess or corner. This is due to a larger frictional shear force in the interfacial region. This in turn can facilitate corner bridging, where the 90° ply on the inner tool surface, or throughout the stack, does not correctly conform to the mould shape. This was described as a result of movement in the first ply caused by shear forces rising above that of the first ply and the tool. It is therefore highly beneficial to deliver

a forming protocol that can reduce the prevalence and increase the prediction of these defects.

2.7 GEOMETRY

As with most forming actions, part geometry plays a crucial role in understanding the material shear deformations and thus the resulting structural integrity of the formed material. Examples of dry fibre tooling used in the aerospace and automotive sectors are rising. Two forerunners of dry fibre fabric composite parts are *BMW* and *Bombardier*. The *BMW i3* used dry fibre reinforcements through RTM manufacture in the fabrication of the complex body frames [19]. Within the aerospace domain, the *Bombardier C Series* aircraft uses around 80% composites in the construction of the wings, with much of the assembly utilising resin transfer infusion (RTI) [24]. These parts have all undergone certification, and serve to highlight the possibilities of NCF materials in the aerospace domain. Typical structures in aerospace can include spars, stiffeners, top hats and winglets. Much of these parts can have large amounts of complexity, with drops, rises and double curvature.

2.7.1 CURVATURE

An understanding of curvature is essential in describing the behaviour of the fabrics in forming. Curvature in 2D is best described by *Figure 2.8*, where curvature can be expressed as the rate of change of direction of the curve [25]. Through defining a circle that has the greatest contact with the curve, having common tangent T at point P. The radius of this circle can then be used to determine the radius of curvature for the given curve. Through this definition, *Equation 2.1*, curvature can be expressed as the reciprocal of the radius of curvature. This relationship defines the basis for all calculations of curvature. A more detailed derivation can be found in Roberts' work (2001) [25].

$$K = \frac{dW}{dS} = \frac{2\pi}{2\pi R} = \frac{1}{R} \tag{2.1}$$

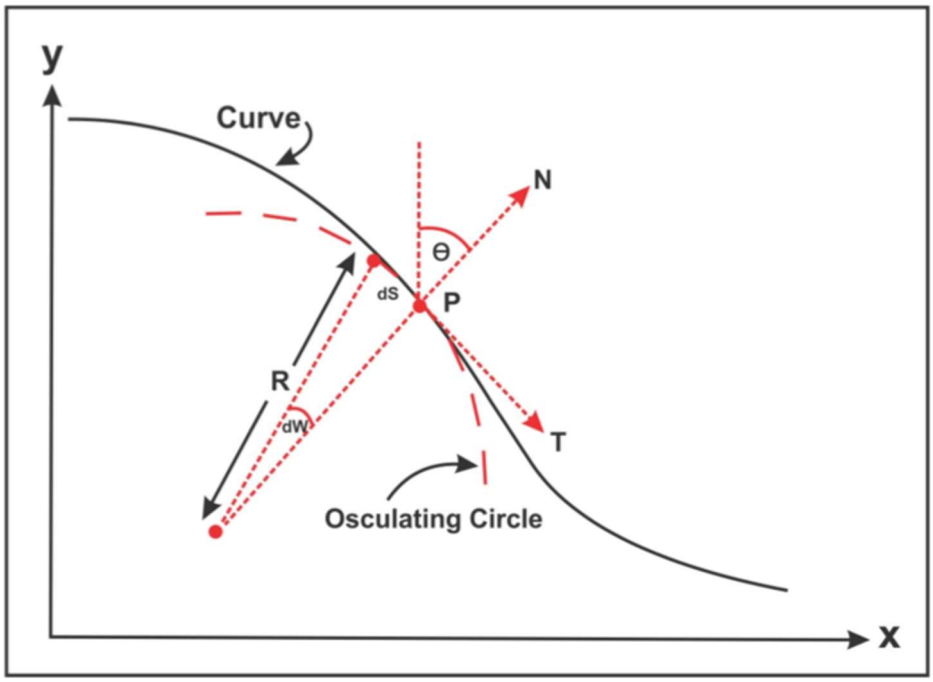

Figure 2.8: Defining curvature. 'For a particular point P on a curve, the curvature can be defined in terms of the radius of curvature, R *of the osculating circle. This circle possesses a common tangent* T *with the curve.* N *is the vector normal to the curve at point* P*, which defines the local dip angle* θ*. The curvature at point P is defined as the reciprocal of the radius of curvature.'[25]*

If we are to visualise 2D curvature on the cross-section of a given surface, sign conventions can be established, see *Figure 2.9.* Where surface normal vectors (represented by grey arrows) diverge over the anticlines, we can define this curvature as positive. Where the surface normal vectors converge over synclines, negative curvature is established. On flat or planar surfaces these vectors are parallel to each other, allowing for the description of zero curvature. To develop this principle to 3D curvature, owing to the fact that 2D curvature could be expressed differently depending on where the cross-section is taken, planes that are orthogonal to the surface are used (see *Figure 2.10*). These planes represent the normal curvatures and allow for a detailed description of the surface.

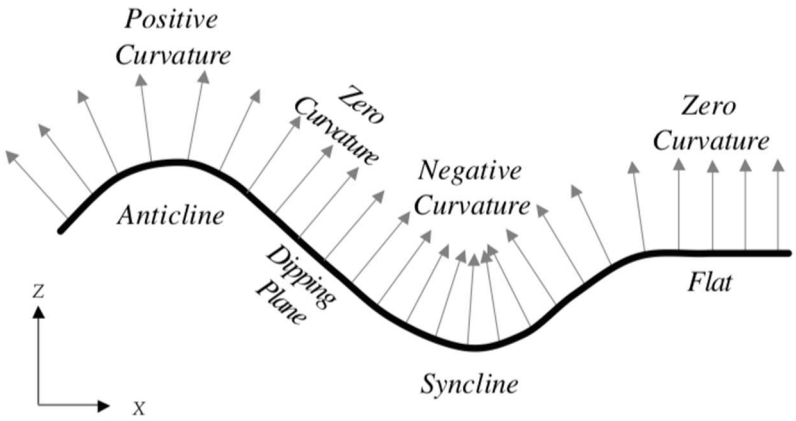

Figure 2.9: Sign convention for 2D curvature, in the engineering domain anticline is typically termed anticlastic and syncline, synclastic. Grey arrows indicate surface normal vectors [25].

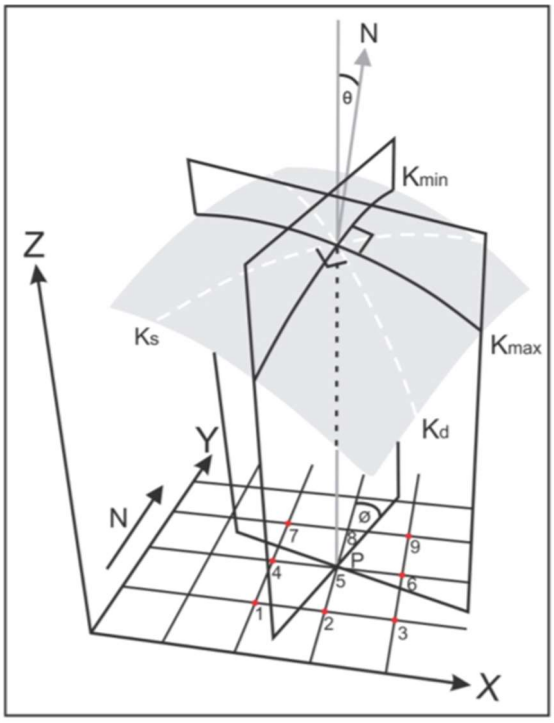

Figure 2.10: 'Curvature in three-dimensions. x and y represent the map axes, with z representing the time or depth axis. Note the intersection of two orthogonal planes with the surface, which describes the maximum curvature, K_{max} *and the minimum curvature,* Kmin. *Two other orthogonal normal curvatures, the dip curvature,* K_d *and the strike curvature,* Ks *are also drawn on the surface.* N *is the vector normal to the surface at point* P, *which makes an angle* θ *with the vertical, called the dip angle. The orientation of any normal curvature can also be extracted, with the angle φ being the orientation of minimum curvature.' [25]*

By combining any orthogonal normal curvatures on a surface, K_s and K_d, the mean curvature K_m can be calculated, similarly the principal curvatures K_{min} and K_{max} can be used as described by *Equation 2.2.*

$$K_m = \frac{K_s + K_d}{2} = \frac{K_{max} + K_{min}}{2} \tag{2.2}$$

Principal curvature K_{max} is defined as the curve on the surface with the largest curvature, the curvature perpendicular to this is defined as K_{min}. These curvatures are described by Euler's curvature formula, *Equation 2.3, where* K_i is the normal curvature in a direction. Gaussian curvature, K_g, allows a surface to be defined by the product of its two-principal curvatures K_{min} and K_{max}, see *Equation 2.4.*

$$K_i = K_{max} \cos^2 \theta + K_{min} \sin^2 \theta \tag{2.3}$$

$$K_g = K_{min} K_{max} \tag{2.4}$$

If the principal curvatures have the same sign $K_{min}K_{max} > 0$ and therefore is defined as positive curvature. If the principal curvatures have different signs $K_{min}K_{max} < 0$ and therefore is said to have negative curvature. Similarly, if one of the principal curvatures is equal to zero, $K_{min}K_{max} = 0$ and thus has zero Gaussian curvature. If a surface has zero curvature, that surface would not require any tension or compression of the material to be formed and is said to be developable. If a surface has negative or positive curvature, the material would require stretching or compressing to allow it to fit over the geometry; both are termed double curvature and stem from a Gauss' theorem egregium [26]. By deforming materials in this manner, the strength and stiffness of NCFs are affected, and the overall geometry can also be affected. This can be due to fibre slippage and disorientation of fibres during consolidation or draping, as the plies

attempt to conform to the doubly curved surface. This makes Gaussian curvature an important aspect of geometry to consider in dry fabric forming of any kind.

2.7.2 PIN JOINTED NET THEORY /KINEMATIC MAPPING

The pin jointed net theory (PJN) is the simplest model of NCF deformation. This allows a kinematic understanding of tension and compression exerted onto the material when consolidating the material over positive or negative Gaussian curvature. First developed by Mack and Taylor (1956) [27], the theory looks at conforming woven cloth to a surface. The theory was then further developed with respect to woven fabric and describes the cross over points of the yarns as nodes. Assumed in theory is that the yarns are inextensible, although some models do add stiffness, no fibre slippage is present but they are free to rotate and are represented by lines with no thickness, see *Figure 2.11.* Whilst the theory was developed for woven fabrics, as NCF materials use pillar stitching, the theory can be extended and has been shown to successfully model the deformation [28]. This is because the stitching yarns separate the fabric into cells, joined by the pillar stitch through its thickness. In a real material system, the fibres and stitching yarns do have thickness. This necessitates that the cross over points will stop rotating, or the fibres must cross over out of plane. This limiting factor is described as the shear-locking angle, the angle at which the fabric is capable of shearing without out of plane deformation.

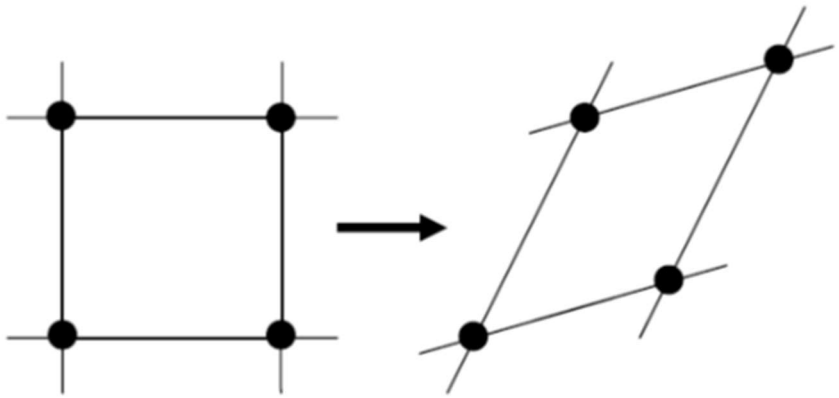

Figure 2.11: Pin jointed net theory. Showing the deformation of the net as the crossover points rotate [11]

2.8 MACHINE LEARNING

Machine learning (ML) is a rapidly growing field of computer science and statistics. Allowing computer algorithms to learn autonomously [29], ML is a powerful methodology. Typically, they consist of a training data set, allowing performance optimisation and output generation. Second, test data is used to validate the model, testing input parameters against known outputs. Wide arrays of algorithms have been developed that suit particular applications with three main different categories: supervised learning, unsupervised learning and reinforcement learning.

Supervised learning describes ML algorithms that have known training examples. These examples all have known inputs and outputs, but do not require knowledge of how the inputs and outputs relate to each other. Through having large data sets of input parameters and known output parameters, the model can develop a model of how to get to those outputs. In composite forming, we may start with the question, 'Which material system should I choose to form a hemisphere without defects?'. Here the output is defined as 'Chosen material', through evaluating 'Will material X cause defects'. This data set would have to be large, with many variables to allow the algorithm to learn which scenario would create defects. The model can then begin predicting which of the remaining materials would create a defective part, which can be subsequently validated. This allows the accuracy of the model to be assessed against the known outputs and can, providing a valid accuracy, begin predicting outputs for materials where the outputs were not previously known.

It is evident that through ML, significant time can be saved in the development of flexible forming approaches, where parameters could be changed much faster and the understanding of the outputs that describe the formability of NCFs over complex geometries could be assessed. Some examples of supervised learning algorithms are: linear and logistic regression, support vector machine, naive Bayes, neural networks, gradient boosting, classification trees and random forest. Unsupervised learning differs in its approach. This type of ML does not have a predefined training data set, and thus only the inputs are known [30]. Thanks to the digital revolution, a wealth of data is available in many new areas, giving rise to the term 'big data'. Understanding these

vast amounts of data and making sense of the complexity involved is a laborious task, if not impossible, without the help of unsupervised learning algorithms. These models work on the basis that the output is unknown allowing the algorithm to find appropriate relationships that interconnect the data. Clustering algorithms, dimensionality reduction algorithms and anomaly detection algorithms are the most common types [29].

The final category is reinforcement learning. These algorithms are somewhere in between supervised and unsupervised learning, with no training data set used and a known output in the form of a known reward. The model works on the basis that it is attempting to maximise a reward by cycling through and making autonomous decisions, learning and developing its understanding of how to maximise the reward in parallel. These approaches have proved popular with typical reward based applications such as winning money or a game, with the popular example of a reinforcement algorithm that could beat human players of Atari [31]. ML and artificial intelligence is a rapidly growing field in manufacturing, with its ability to process large amounts of data and make sense of complex situations. Inherent to this, however, is the need for significantly large data sets, with large amounts of parameters. This forms the basis for much of the subsequent work planned for this thesis, with the generation of valid data paramount to allowing appropriate ML algorithms to be exploited in the pursuit of optimised forming operations.

2.9 CONCLUDING REMARKS

This chapter set out the key background and definitions used within this thesis and produced the following remarks:

- Dry fibre fabrics, in particular, NCFs are seeing rapid deployment in industry due to an improved strength to weight ratios compared to woven materials and also reduced dwell times, increased shelf life and processability.
- Biaxial warp-knitted NCFs are most typical.
- There are numerous forming processes, however, most still have large manual elements in the process.

- Common NCF preforming defects include in-plane fibre waviness, out-of-plane wrinkling, compression folding, tow gapping and tow slip.
- Machine learning methodologies could prove potent in preform optimisation.

CHAPTER 3

LITERATURE REVIEW

This chapter presents a review of the surrounding literature, first considering the complexities of NCFs, before evaluating characterisation methodologies. The review also evaluates the current state-of-the-art in automated manufacture and the application of machine learning to forming.

3.1 COMPLEXITY OF NON-CRIMP FABRICS

Biaxial NCFs have several characteristics that make the material system more complex than just a simple laminate of two UD layers. Much of the reason for this is because NCFs were developed from conventional woven fabrics and also from prepreg materials to keep woven fabrics quicker cycle times and simple processing, while reducing the negative effect of crimp. Through the development of prepreg materials, it was shown that with the inclusion of a toughening veil, much larger part toughness and damage tolerance could be expected [32]. This veil is typically a discontinuous fibre mat stitched into the NCF assembly on the outer ply, identified in *Chapter 2, Figure 2.5.* In the most part, this is because the veil facilitates greater resin wetting of the fibres at the infusion stage, it also reduces the ability for cracks to nucleate in voids and thus stops a crazing effect, where multiple cracks initiate at these voids. There is, however, no known literature that looks at the effect of the veil at the preforming stage. This highlights the need for characterisation work including this additional veil. Further additions to the material assembly can typically include polymeric binders. These binders are commonly powdered resins applied to the outer surfaces of the fabric to assist in fixing a stack of NCF plies in their desired orientation on a preform. They can also be applied after, as a resin film or sprayable fluid, however powdered binder derivatives seem to be the most common choice in industry as they are safer to apply (free from styrene emissions) and allow better control of the matrix volume fraction [12]. The effects of the binder on the preforming stages of production are also not yet fully studied in the literature. Mulvihill *et al.* (2017) [33], commented on the complexity of evaluating the contact area for a carbon fibre tow with an added binder through Hertzian analysis – classical contact analysis, and concluded that the assessment was not feasible.

The stitching parameters have a significant influence on the final NCF material created. Firstly, when the stitching pillar yarns are threaded through the thickness of the material, the needle must push the adjacent tows apart, allowing a channel for the yarn to pass through [34]. This parameter induces openings between the carbon fibre

tows as the fibre bundles are forced to deviate around the thread. *Figure 3.1* shows this characteristic in greater detail.

When the fibre direction is not 0° or 90°, the openings form diamond shapes whose axis are aligned with the fibres. When the fibres are 0° or 90° the openings form continuous channels [9, 34]. These characteristics add what can be termed a level of crimp within the fabric, the very property that NCFs were developed to mitigate. However, the level of crimp that the tows experience is still relatively small in comparison with their woven counterparts. The magnitude of the openings can also be controlled through further stitch parameters. Stitching yarn thickness and yarn tension all play a role in the formation of the channels, with larger diameter yarns requiring larger deviations from the optimal fibre path. In the same manner, stitching yarns fabricated with greater tension, bundle the fibres into more tightly packed tows, creating larger opening at their intersections. Not only do these openings have the same effect as crimped fabrics, where mechanical properties are reduced as the fibres are not in full alignment. They also facilitate areas that can become resin-rich during the infusion stage. Truong *et al.* (2005) [7] showed that these resin rich zones reduced the damage tolerance of parts and facilitated the nucleation of cracks. However the openings created by the stitches also have been shown to have benefits in resin permeability, with an increase upwards of three times the permeability in relation to the stitch openings [35]. These findings both highlight that NCF properties can be somewhat tailored to balance

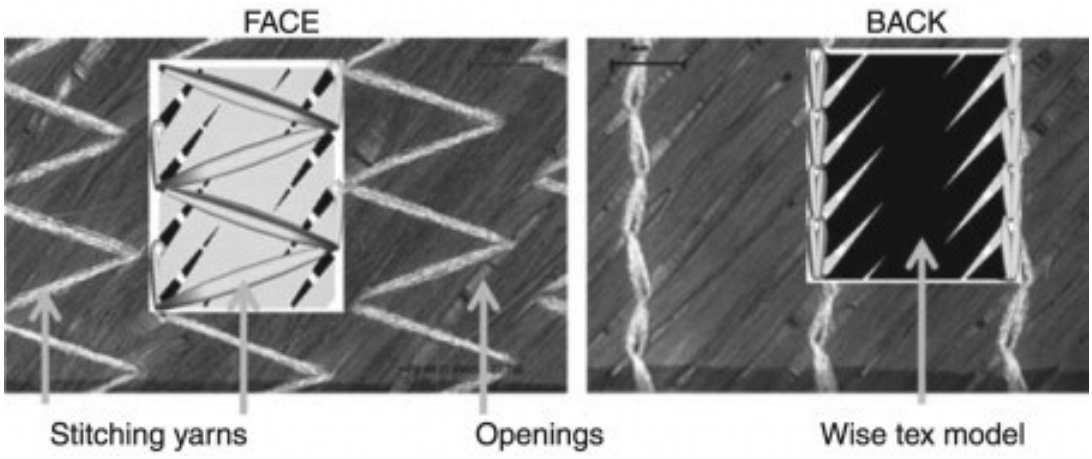

Figure 3.1: The effect of stitching on the formation of openings between the carbon fibre tows [34]

damage tolerance and permeability through appropriate stitch choice. Comparing this with woven fabrics, where permeability changes are affected by fibre path, NCFs allow, for the most part, a decoupled parameter, the stitch, to be modified without affecting the fibre paths significantly.

3.2 INTRAPLY SHEAR

The complexity of NCFs necessitates complex shear deformations through forming, with intraply and interply shear considered the primary modes. In-plane shear deformation of a composite at ply level is termed intraply shear. A key deformation mode, intraply shear describes relative sliding of parallel tows and the rotations of these tows at the crossover points [36]. Through this in-plane deformation, NCF materials can conform to doubly curved surfaces without folding, wrinkling or cutting. Intraply shear allows for formability to be assessed from this perspective, allowing for the calculation of the shear locking angle, and thus allows evaluation of whether a doubly curved geometry will form without defects. In NCF materials, these crossover points follow the PJN assumptions evaluated in the subsequent sections and relate to the pillar stitch location. Much of the characterisation work has its basis in woven fabric characterisation and was extended for use into prepregs. For dry fibre, existing tests are heavily dependent on the ability to apply the PJN assumptions to allow for an understanding of deformation. This necessitates that any material without a woven interface, or a NCF without a pillar stitch, cannot be studied through these methods. In practice this limits material choice to these variants to allow for a fundamental understanding to be achieved. This is particularly pertinent in the aerospace industry, where a full understanding of material characteristics is required. Two tests have been used in the literature to study intraply shear: The picture frame test and the bias extension test.

3.2.1 THE PICTURE FRAME TEST

The picture frame test fixes a square section of material in four hinged clamping set-ups resembling a diamond picture frame. *Figure 3.2* shows a schematic of the standard test rig. The material can undergo pure shear over the entire specimen area, particularly

with dry fibre as the material can be clamped via clamping pins, allowing rotation. The test-rig is fixed to a tensile testing machine via the crosshead mounting brackets, and then pulled apart at a set strain rate until the maximum deformation is reached. The load required through the test to reach this point is recorded and an assessment, either visually, or through digital image correlation (DIC), of the shear locking angle is made. This looks at the maximum angle the fabric will deform to without out-of-plane deformation.

Shear force can be calculated from the axial load readings from the load cell using *Equation 3.1*. Where F_{pf} is the axial load and Φ is the frame angle.

$$F_s = \frac{F_{pf}}{2\cos} \tag{3.1}$$

Test data can then be normalised by dividing the shear force F_s by the picture frame length L_{pf} [36]. *Equation 3.2* highlights the shear angle definition.

$$\theta = \frac{\pi}{2} - 2\Phi \tag{3.2}$$

Shear angle can also be calculated from the crosshead displacement, d_{pf}.

$$\theta = \frac{\pi}{2} - 2\cos^{-1}\left[\frac{1}{\sqrt{2}} + \frac{d_{pf}}{2L_{pf}}\right] \tag{3.3}$$

Concerns have arisen over how small misalignments in fibre direction in the clamps can affect the results, repeatability of tests and induce non-pure shear [36-41]. Further, by fixing all boundaries, the validity of the test is questioned, as generally, in forming, boundaries are free to move. This translates into the specimen generally having some magnitude of pre-tension in the fibres and stitches. Work has shown that this tension can increase the shear values and locking angle magnitudes significantly, reducing the precision of the test [37, 41]. Launay *et al.* (2008) [41] highlighted that by using a modified picture frame that allows for pre-tension to be measured and then zeroed, results were far more in line with what is to be expected and repeatability increased. This test rig included load cells on the lower clamping plates, with torque screws on the upper plates. This also goes some way to highlighting the lack of a standard picture frame test protocol. A collaborative effort, by seven international research

organisations [40], looked at this lack of standardisation. Large variations in results were found after each organisation characterised the same material through varying clamping mechanisms, and showed that these large variations were attributed to fibre misalignments and differing test protocols. This means that for any picture frame test, stringent control and documentation of both fibre orientations, sample preparation and test protocols are needed to increase the precision of tests.

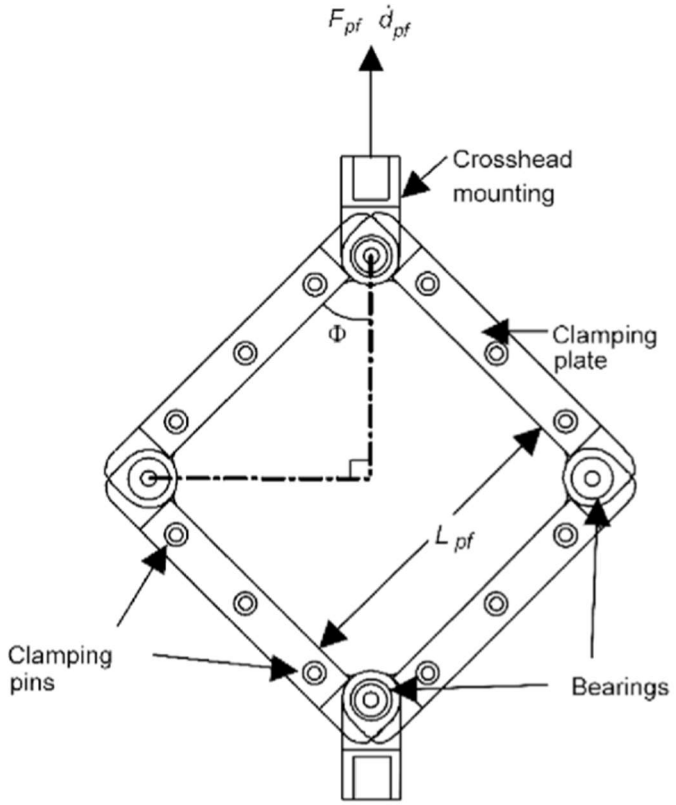

Figure 3.2: Schematic of the picture frame test rig. L_{pf} is measured between the bearings and is the side length, F_{pf} is measured by the load cell and is the axial load, d_{pf} is the crosshead displacement and Φ is the frame angle. The fabric is aligned such that orthogonal fibres are parallel to the clamping plates allowing intraply deformation when an axial load is applied via the top crosshead mounting bracket[36].

3.2.2 THE BIAS EXTENSION TEST

The bias extension test is another widely used characterisation test that looks at intraply shear deformation. This test places a rectangular specimen in two clamps on a tensile testing machine whose fibres are aligned ± 45° to the applied tensile load. Figure 3.3 shows a standard test with an aspect ratio of 2, specimen widths are generally reported >100 mm [36]. The specimen is segmented into seven distinct zones, with only zone A undergoing pure shear. Whilst this means the entire specimen is not subjected to pure shear, the benefits of the test include the fact that only two edges are fixed and none of the pure shear zone is clamped. This better represents the behaviour at the intraply level, compared with the picture frame test. Misalignment of fibres is still however a concern, with fibre crimping in the clamps and small misalignments accounting for wide variation in results [37, 40, 42]. Wide strip bias extension tests, which use a sample width wider than the clamps, has shown promise reducing tow slip before shear locking however [43]. No standard methods of clamping have been developed and so careful sample preparation that avoids misalignments is necessitated. The calculation for shear force and shear angle follows the same protocol as for the picture frame test. Whilst the bias extension test has a more complicated shear mechanism, the pure shear zone is a much improved representation of intraply shear without boundary control.

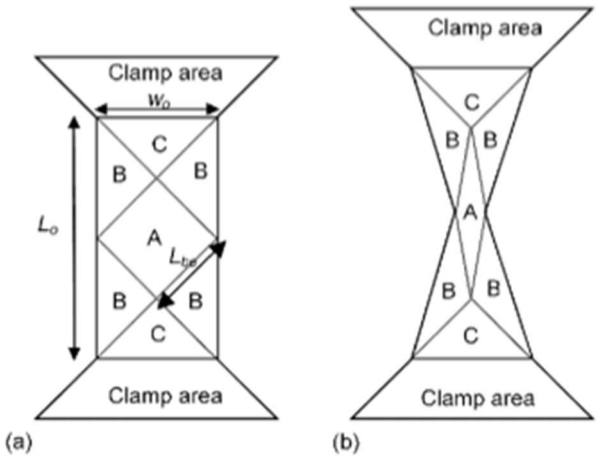

Figure 3.3: Schematic of bias extension test. Where L_0 is initial length, W_0 is initial width and the aspect ratio $\lambda = L_0 / W_0 = 2$ [36].

3.3 INTERPLY SHEAR

The second fundamental forming characteristic is a material's interply shear property. This is particularly so for composites where large ply stacks are typically used to create a final part. Through forming, these plies will have to shear over tooling and also over subsequent plies. Interply shear is therefore characterised at either the fabric-fabric level or fabric-tool level. Much of the interply shear behaviour is governed by the frictional response of the material. As the focus is dry fabrics, friction is usually modelled using the Coulomb friction model. However, this assumes that the material undergoes little elastic deformation prior to yielding. Work by Erland [11] (2016) showed that by using the Mohr-Coulomb yield criterion, a better model of friction could be developed. This allows the full frictional response to be evaluated, with respect to various normal clamping forces.

The existing literature on interply focuses primarily on prepregs, with a few studies looking at NCF in contact with a forming tool [44]. There is also some significant work looking at single carbon fibre tows and the frictional response at the tow-tool and tow-tow level, with an assessment of contact area [33]. So far no work has looked at the influence of interleaving or veils at the interply level, as well as little work looking at the effects of binding agents. Mulvihill *et al.* (2017) [33] did study a carbon fibre tow with binder, however, due to the added complexity and it breaking the assumptions for valid Hertzian analysis, the bindered tow was not included in the calculation of true contact area. There is also no standardised test method for investigating interply shear. There are, however, two main variants for looking at fabrics in the literature and also a further for looking at single tows.

The first test method utilises a fixed surface of material, with a sled arrangement on top with the interface also wrapped in material, see *Figure 3.4*. Many of these frictional tests have been developed from ASTM D 1894 (ISO 8295), which was originally developed for friction determination of plastic films and sheeting. Whilst this method has proved useful for simple analyis, it requires a lot of space and a fabric that is relatively flat in topology to allow free movement of the fabric that is constrained in

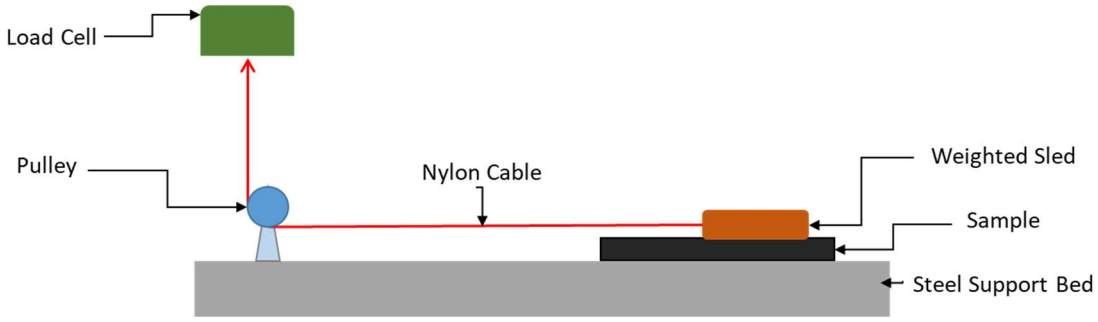

Figure 3.4: Schematic of friction sled test. A nylon cable is attached via a low-friction pulley to a load cell and a weighted sled. The weighted sled applies a known normal force. The sample is first placed between the sled and a steel support bed. The load cell then moves up and records the interply shear force, allowing the calculation of the interply shear stress by using the surface area of the sled.

one direction. The sled is weighted to induce a typical normal force on the interface and then pulled via a tensile testing machine. This allows the calculation of the coefficient of friction for the material from the load and extension data. An assessment of NCF-tool interply shear was made by Avgoulas *et al.* (2018) [44]. Whilst this sled method is not seen as the optimal method, it was used in the previous study to allow a novel assessment of contact area via a semi-reflective coating applied to a glass slide (used as the forming tool).

A second technique is termed a pull through test, see *Figure 3.5*. This involves clamping a fixed material in a tensile testing machine, then using a pneumatic pump that controls the normal force connected through a hinged array, to plates that are allowed to move up the surface. Studies using this set-up have typically been prepreg materials, owing to the reduced test space required allowing for set-up in an oven [11, 45, 46]. From the load and extension data, the coefficient of friction can be calculated. This test method allows a greater control of the normal force, and also allows for a more condensed testing space, without the requirement of flat topology.

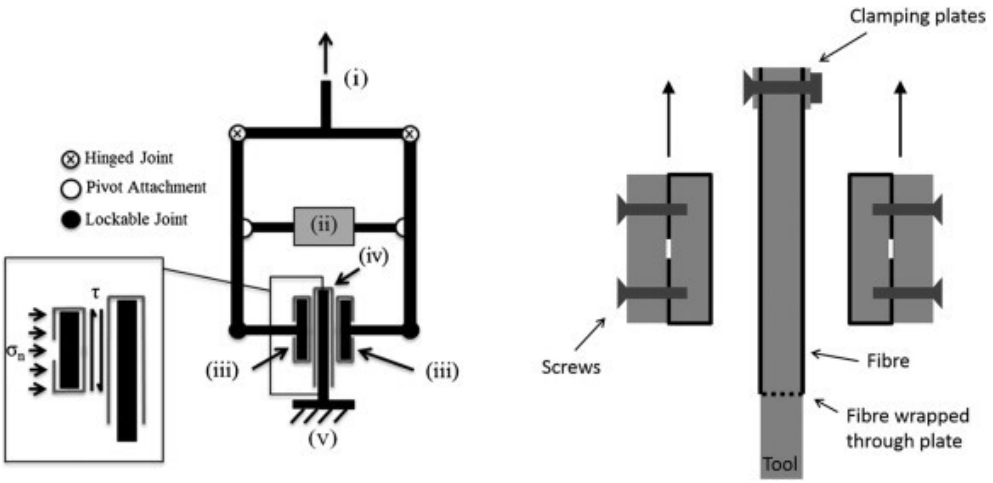

Figure 3.5: Schematic of pull through friction test [11]. The sample is fixed to two clamping plates, which via a hinged array, apply a normal force. A third fixed plate is attached to a lower tensile testing machine fixture, and the top hinged array is raised, recording the force. The interply shear test is calculated taking into account the surface area of both clamping plates.

Both these tests have been employed to look at the frictional response, with more studies looking at the ply-tool friction than that of ply-ply. The majority of studies highlight that by increasing the interface angle, friction decreases [11, 44-46]. This is said to be a factor of reduced contact area as the fibres are not aligned and therefore reduced fibre meshing is present. However, most studies have not looked at the influence of stitching, which are a dominant factor in NCFs. Much of the literature shows that contact area could significantly affect the interply shear response, with lower pressure reducing the contact area. Under higher pressure, more intermingling and meshing of fibres is expected. This is particularly pertinent for fabric forming over complex geometries where significantly low local pressures can exist. The way in which frictional response is measured tends to implement a unit cell approximation method, where the response is purely characterised in the meso scale. The frictional response of the material could also be studied on the micro scale, looking at individual fibre friction over one another. This method is far more complex however, and may prove unnecessary when looking at the macro forming behaviour of NCF materials. As was mentioned previously, no studies have looked at the influence of a discontinuous fibre veil or toughing layer on interply shear, as well as the contribution of binding

agents or stitching in NCFs. These are all areas where more research is required, allowing for a fundamental understanding of the NCF materials used in industry. Further, to understand interply shear, and also intraply shear, the manufacturing techniques typically used by industry to increase productivity, requires evaluation.

3.4 AUTOMATED MANUFACTURE

As decreasing the cycle times for composite part manufacturing is a paramount concern, automated techniques for preforming and curing are vital. Many of the manufacturing processes identified in *Chapter 2* have a multitude of process steps that can reduce the manufacturing throughput. Specific considerations in manufacture are needed to create processes that have high-cycle rates, whilst also providing an economically viable solution. In many manufacturing situations with many mating parts, part complexity cannot be dramatically altered after the design stage to take into account formability issues. Creating formable parts requires processes that are amenable to adaption, with flexible systems that can be simply reconfigured with unique boundary conditions during forming. Manufacturers such as tier 2 aerospace suppliers, are motivated to move to these flexible systems in line with the idea of Industry 4.0. By automating certain aspects of production, expensive high-skilled labour can be redeployed and modern computational power, coupled with statistics and digitisation can improve production efficiency. Antecedent to automation however, is identification of the key requirements from such a system, here, these are defined as *ideals*:

- Highly flexible process control
- High throughput/ low dwell times
- Reduced cycle times
- High damage tolerance/ quality/ repeatability
- Capacity for complex geometries and tooling
- Developable (i.e. is modular or expandable)
- Computationally modelable (i.e. *viable* FEA/digital twins)
- Boundary condition control or deformation control
- Economically viable

The applicability of automated manufacturing processes, is highly dependent on the complexity of the desired part as well as the quantity required. Automated fibre placement (AFP) is one development that aims to achieve some of these ideals. The process utilises carbon fibre tows held in tension, usually on a five axis robotic arm, this tow is then fed onto a mould and placed in the desired orientation [47]. These machines often have moving moulds that allow the robot dexterity in placing the dry fibre tows down. This is beneficial in permitting fibre steering, however, cycle times are greatly increased [19]. AFP process defects are also well researched, with 10 key classes identified, which include gapping, and overlaps predominate [47]. The tow architecture after fibre placement has also been shown to influence the resin wetting during infusion [48]. Automated tape laying (ATL) reduces some of these effects by having larger carbon fibre tapes, usually NCF rectangular strips, which are held by a robotic end effector and placed onto the mould [19, 49]. This increases the volume of fibre that can be placed with respect to time, however this technique means that the fabric is cut into small panels, with joins in between. This greatly reduces the strength and stiffness of the final part. Both of these processes can, however, be used to develop preforms. In the case of NCF materials, only ATL is appropriate in automated preforming. Whilst the system is proven in industry, it does mean that the mechanical properties of the final component are reduced and mitigates many of the advantages NCFs were designed to overcome. Further considerations around the minimum turning radii [50] have to be accounted for, particularly in parts with high curvature or double curvature. Dirk *et al.* (2012) [51] reviewed the literature surrounding ATL from the perspective of prepregs, which is much the same process as is used for NCFs. Whilst they identify that high lay-up rates can be achieved and large parts can be fabricated, they also stress that the process has limited formability over double curvature. Mills (2006) [52] however studies ATL of NCF material in the production of a demonstrator aileron and through cost modelling evaluates the process to have a 20% reduction in cost in comparison with RTM. This highlights the need for new processes in the preforming of NCF parts that allow the material to have increased damage tolerance whilst still increasing formability over complex geometries and reducing cycle times.

Further strides to automate the manufacture of composite components have been made. Many examples aim to create more automated lay-up of fibres over more complex tooling. Reinhart and Ehinger (2013) [53] developed a robotic end effector with vacuum assisted gripping and heat cells to activate the binder. Whilst the concept only proved viable on single curvature, extension to double curvature is in progress. Larger components such as a 4 x 3.5 m doubly curved dome have been successfully produced with an automated preform and gripping systems [54], in a similar manner to [53], see *Figure 3.6-3.7*. Here double curvature was achieved, however as the demonstrator was so large, the shear deformations required of the fabric were relatively small. Eckardt *et al.* (2016) [55] use collaborative robots to pick and place NCF plies over single curvature fuselage demonstrators. Whilst these geometries do not require intraply shear of the NCF, they do help to show, along with [53, 54] that automation of the preforming stage is viable. A state-of-the-art review of robotic grippers and their applications is undertaken in [56].

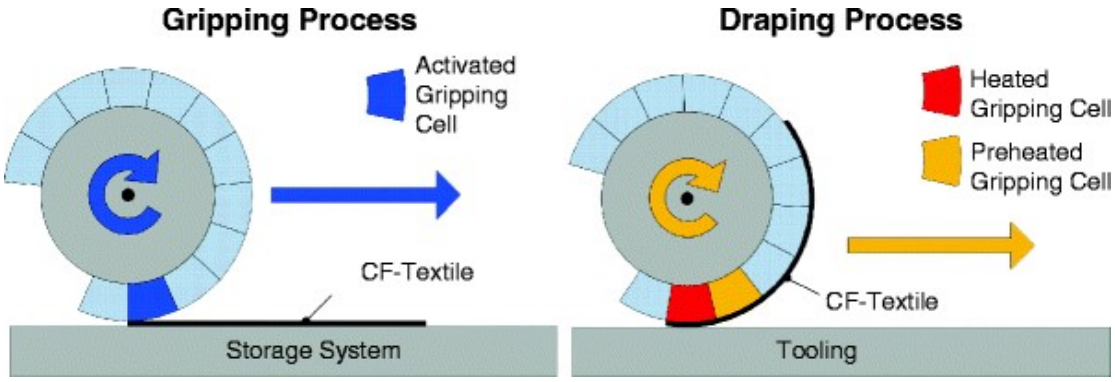

Figure 3.6: Schematic of a robotic end effector gripping and draping process with integrated heating cells [53].

Further techniques such as *automated profile preforming* have seen increased development of late. The technique is usually based on fixed cross-section parts which are fabricated in a method analogous to metal extrusion. Here, fabrics are typically compacted onto a tool with the use of fixation aides such as rollers [57]. The dry fabric preforms can bring further speed savings through the use of braided or woven preforms.

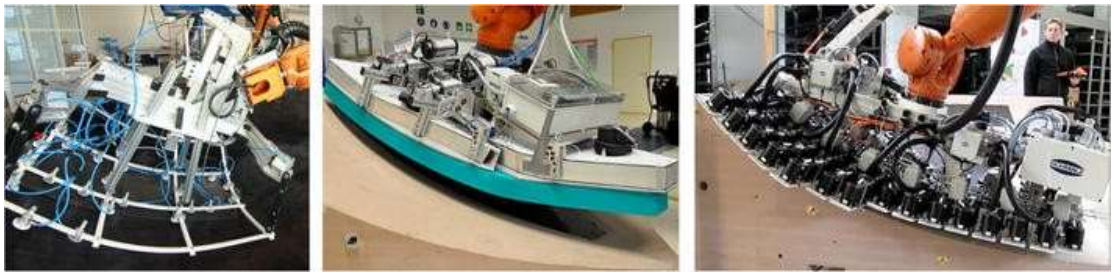

Figure 3.7: A second example of a robotic end effector gripping and draping system with integrated heating cells. This example highlights a much larger end effector array and the double curvature target geometry [54].

Whilst the parts are relatively simple, automation of primary and secondary structures such as those with continuous cross-sections, allow more time to be spent on more complicated parts. One such method that is gaining popularity in recent years, is *bladder-assisted moulding, Figure 3.8*. Bladder assisted moulding takes much of the learning from membrane forming and vacuum assisted processes. Here elastomeric bladders are inflated to provide a geometrically flexible mould tool. Here the inflated bladders add normal pressures to carbon fabrics against a usually metallic mould [58-60]. The benefit of this type of manufacture stems from the ability to add many different bladders to one part, tailoring the inflation and compaction pressures to optimise boundary conditions during forming. These systems allow complex forming protocols, often aided by efficient preparatory 2D or 3D preform cutting and assembly, including the use of braided preforms and sleeves. Bladder assisted manufacture can however prove problematic in some circumstances, such as proper material compaction in sharp

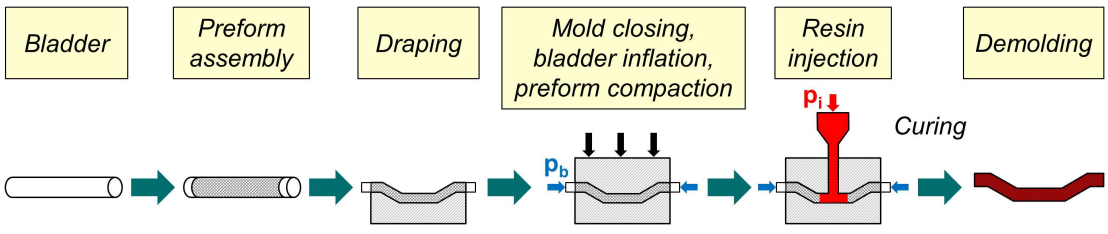

Figure 3.8: Schematic representation of a simple bladder assisted moulding process [58].

internal corners and a difficulty in assessing compaction pressures [59]. However, the method does suggest, coupled with the increased uptake in real world production settings, that the ability to tailor boundary conditions in a simple manner is paramount to building production complexity.

3.5 DRAPING

Draping is the process of forming an originally flat ply over geometry, through interply and intraply mechanisms. Experimentally draping tests have been conducted over relatively simple geometries; typical shapes include hemispheres [10, 54, 61-65] , tetrahedral [58-60, 66, 67] and extended hemispheres [68-70]. These geometries generally allow some degree of Gaussian curvature and therefore require a material to stretch or compress to conform. Hemispheres and extended hemispheres are generally shown to have shear angles up to 50°, whilst tetrahedral geometries up to 60°. The majority of these examples have been studied from an experimental approach and an FE approach, this generally allows verification of experimental results but also allows tests to be extended to more complex scenarios. Differing approaches have been taken in the literature and are generally categorised as macroscale, mesoscale and microscale modelling. Macroscale models represent the material as a continuum and will be discussed in more detail in *Chapter 5*. In micromodels, attention is placed on modelling interactions right down to the fibre level. Software packages such as *AniForm, PamForm,* and *TexGen* have been developed that allow for efficient modelling at this scale. Meso modelling looks at using the unit cell approach to approximate behaviour over a predefined cell. This approach allows much faster modelling with less computational expense, however it cannot distinguish defect location and only allows for validation of defect likelihood. In many cases this is sufficient for developing a fundamental understanding of material deformation over a given geometry. However, much of the draping work to date requires extensive material characterisation work and full understanding of the deformation mechanics, which most often are simplified and do not include the full effects that the complexities of NCFs bring. This serves as a precursor to the development of ML in this field, allowing much greater flexibility in the production of defect free parts.

3.6 MACHINE LEARNING

Whilst ML techniques are in their infancy with respect to composite forming, several studies have developed supervised learning algorithms to study the mechanical properties of cured parts and also the resin infusion stages of forming. Artificial neural networks (ANNs) have been the algorithms of choice within the sector. Whilst the full mathematical understanding of ANNs is not presented in this work, a compressive review of the algorithm, with respect to polymer composites can be found by Zhang and Friedrich (2003) [71] and also El Kadi (2006) [72]. Zhang and Friedrich (2003) [71] determined that through well-trained ANNs, the need for experimentation could be significantly reduced. This is particularly pertinent for future flexible manufacturing processes, where ANNs could facilitate the prediction of material properties and other manufacturing parameters without the need to test every new component developed. Here, a review of current ANNs and the applications within composite materials will be discussed.

Zhao *et al.* (2016) [73] used ANNs to create a carbon fibre fabric classification model. The model was developed using 229 data groups, with 85% used as the training data set and 15% as the test set. The independent variables were sample width, breaking strength and breaking tenacity. However, as the ANN operated in the standard 'black box' manner, the link between manufacture and classification was not made. Other examples in the literature focus on the permeability of carbon fibre preforms and on resin flow during RTM [74, 75]. The latter, Rai and Pitchumani (1996) [75], showed that an accurate model could be developed from validated processes models that increased the computation speed by around seven orders of magnitude. This highlights the effectiveness of using ANNs and offers an insight into the reduced cycle times it could offer carbon fibre preforming.

Further applications are found in machining and mould surface finishes of parts. Erzurumlu and Oktem (2007) [76] looked at predicting surface roughness of aluminium moulded parts for the aerospace industry using cutting parameters of feed, cutting speed, axial–radial depth of cut, and machining tolerance. Whilst this was demonstrated successfully on aluminium and not composites, it did show that through using

MATLAB's machine learning toolbox and a large experimentally derived training data set (243), successful prediction of surface roughness with 1.48% maximum ANNs test error. This highlights the possibility of similar prediction of surface morphology during composite forming, where out-of–plane wrinkling could be analogous to surface roughness in metallic parts. One study by Heider *et al.* (2002) [77] used process simulation to build a training data set for an ANN that outputted set points for prepreg tows in an AFP process. The ANN predicted that quicker cycle times of 50% of the existing AFP process could be achieved with greater head velocity, thus reducing manufacturing costs.

3.7 BOUNDARY CONTROL

One area of NCF forming that has received little attention, particularly from the perspective of drape forming (DF), is that of optimised boundary control. It is well understood that NCFs exhibit asymmetric intraply shear behaviour due to the imbalanced stitch architecture, which causes resistance to shear in the stitch direction [23, 78-80]. This asymmetry has been shown to induce significant wrinkling in both experimental [23] and simulated results [80] of NCF materials over hemispheres. Hemispheres are used due to the axisymmetric geometry, allowing evaluation of the stitch influence on the intraply shear behaviour. One avenue researchers have explored in controlling this behaviour is through applying a blank holder force (BHF) to the NCF in RTM forming processes, where a solid upper male mould tool is lowered into the female, termed stamp forming. These processes are analogous to DF in the way the material deforms. Lee *et al.* (2007) [23] experimentally studied the effect of BHF on glass fibre NCFs produced through stamp forming and showed that through increasing the BHF, the asymmetry reduced. They also highlight the wrinkle size reduced significantly with increasing BHF. *Figure 3.9* highlights their findings, with the researchers commenting:

> "…it may be concluded that BHF is an important factor to determine the NCF's forming behaviour and furthermore, optimization of BHF may enable the forming of an NCF with no or few wrinkles."

Their study also found correlation with simulated results. However, they found that a much larger BHF (>1000 kgf) caused defects due to the severe shear deformation. This shows promise for BHF optimisation to minimise defects and improve formability.

A further study conducted by Tanaka *et al.* (2014) [81] evaluated BHF and the effect of changing the boundary conditions (BCs) of the blank holder to optimise the same forming process over a hemisphere. The study looked at biaxial carbon fibre NCF with four different BCs tested, *Figure 3.10.* (a) Applied a uniform BHF across the fabric, (b) a BHF was only applied in the ±45° direction and not in the 0/90° direction, inducing tensile forces, (c) no BHF was applied and (d) BHF applied in the 0/90° direction and not in the ±45° direction. Albeit whilst not reporting the magnitudes of BHF, it was however concluded that by applying BHF, formability increased, and more interestingly, shear deformation was improved in the 45° direction by applying the tensile load in test (c) and removing it in the 0/90 direction. Further, they showed that there was significant variation between the shear deformation as a result of changing the BCs and BHF of the forming operation. This, when combined with the work of Lee *et al.* (2007) [23], highlights that optimisation of BCs and BHF could facilitate better forming with reduced defects.

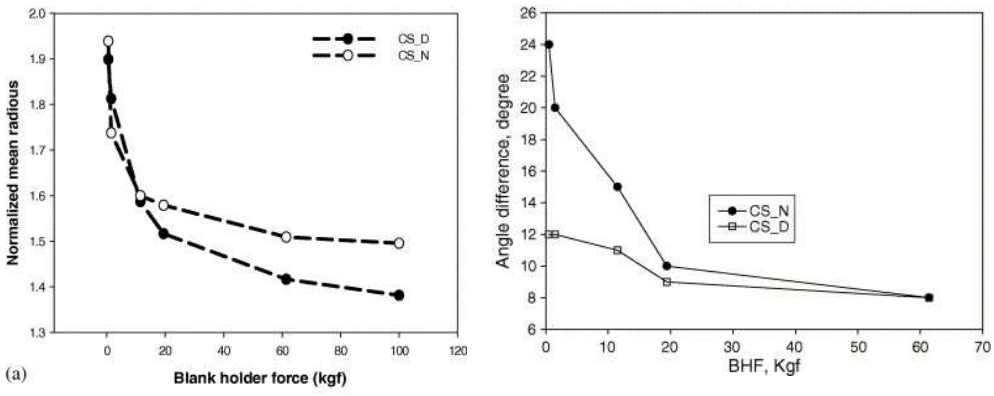

Figure 3.9: Both from Lee et al. (2007)[23] for two materials, CN_N & CS_D, (a), Highlighting the reduction of the wrinkle mean radius with increasing BHF, (b), Showing a reduction in asymmetry as a result of increasing BHF.

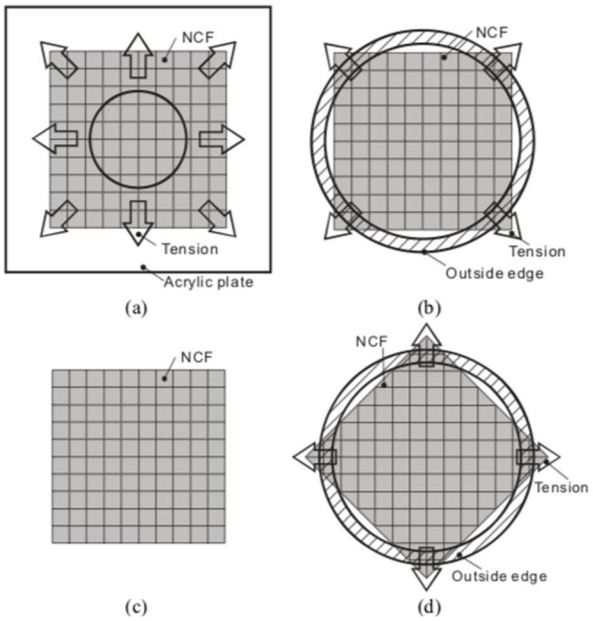

Figure 3.10: Tanaka et al. (2014) [81] different experimental BCs for forming experiments.

3.8 CONCLUDING REMARKS

The deductions made by the researchers offer an interesting opportunity for novel optimised active boundary control through the implementation of ML. Through MLs powerful analytical capabilities, an innovative approach to preforming is hoped to be developed, increasing productivity whilst simplifying production complexity. Insights from the preceding literature review can be summarised as:

- Non-crimp fabrics are highly complex, with additional reinforcements such as the veil adding further anisotropy. Characterisation of NCFs including these aspects is not found in the literature.
- NCFs predominantly deform through shear. There is an opportunity to implement active boundary controls that harnesses the deformation.
- Automated manufacture of NCFs remains challenging. Several key aspects were identified that such a system should fulfil. These are summarised as:

Highly flexible process control, high throughput/low dwell times, reduced cycle time, high repeatability and quality, capacity for complex geometries, developable (i.e. modular), computationally modalable and boundary condition control.

CHAPTER 4

MATERIAL CHARACTERISATION

This chapter characterises a complex NCF. Complex in this regard refers to the additional components in the biaxial fabric, such as the veil, binder and tricot-pillar stitch, that further deviate the material from biaxial woven materials. First, in S*ection 4.1*, the material system selected for the main body of research is set out and evaluated through microscopy. This is to identify the key topological elements that may contribute to the analysis of mechanical properties. Secondly, interply shear is discussed, with experimental analysis of the frictional effects of interply sliding. Third, out-of-plane cantilever bending experiments provide evaluation of the transverse bending stiffness. Finally, this chapter will set out the in-plane intraply shear properties found through bias-extension experiments.

4.1 A COMPLEX BIAXIAL NCF - MICROSCOPIC ANALYSIS

As discussed in the literature review, NCF materials exhibit complex anisotropy governed by the material architecture. Unlike the closest comparator, woven fabrics, the carbon fibres in NCFs do not provide intraply structure in the transverse direction. This requires a further stitching yarn in place of fibre crimp, however the stitching adds further anisotropy to the fabric. Moreover, additions such as toughening veils (random orientation) and pre-applied polymer binders (PB), further complicate an already complex material system. Material systems including veils, to the best of the author's knowledge, have never been characterised fully in the literature. With increasing use of these materials, an understanding of the major deformation mechanics and material characteristics is essential.

All studies were conducted with a *Tenax* biaxial NCF (*Teijen IMS65 E23 24K*). This material consists of 0° and 90° unidirectional (UD) fibres with a polyamide copolymer (CoPA) tricot-pillar stitch. Below each UD ply, chopped strand toughening veils (ET205) are present. A powered binding agent (*EPIKOTE™ Resin 05311* – 15 g m^{-2}) was also applied to the outer veil by the manufacturer. *Figure 4.1* shows a schematic of the material composition and constituent plies [90v0v], with both front and back views. *Figure 4.2* shows images of the chosen material. The front is distinguished as the 'fibre side', with stitches orthogonal to the 90° fibre, the back is

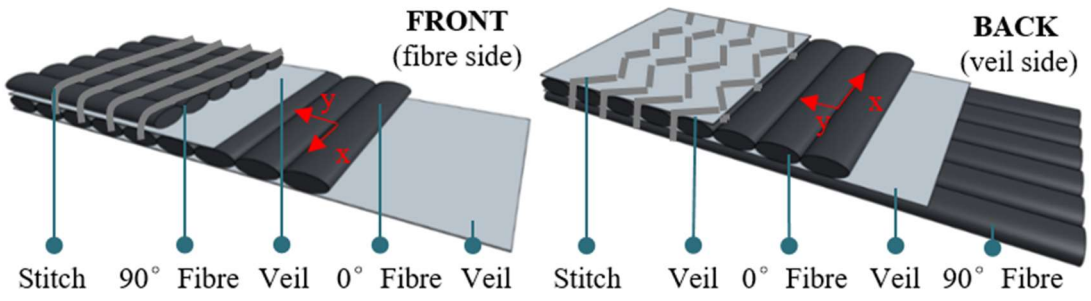

Figure 4.1: Biaxial NCF [90/v/0/v] schematic of the material employed in this thesis.

defined as the 'veil side', faced with a veil and tricot stitches $\pm 45°$ to the 0° fibre. The fibre elastic modulus, as stated by the manufacturer was 290 GPa, with the measured fibre volume fraction of the NCF, V_f = 0.33. The remaining volume is taken up primarily by air but also by the non-structural elements such as the veil and stitches. Table 4.1 describes the material composition.

When examining the material, it became apparent that the stitches on the fibre side were much more prominent than the stitches on the veil side. This is highlighted in *Figure 4.2,* where the veil appears to mitigate the prominence of the ±45° tricot stitch. The fibre side 0° stitches are more prominent and further serve to highlight the intricacies of NCFs as they were identified in the literature review. The binding agent is also visible as particulates on the veil side, identified in the magnified image. To assess these additions in more detail, microscopy was employed.

Table 4.1: NCF material construction and composition used for this study.

Layer	Material	Material Designation	Areal Weight (g m^{-2})
5	*Powder Binder*	*EP05311*	*15*
4	*Veil*	*ET205*	*8*
3	*90°*	*Tenax®-E IMS65 E23 24K 830tex*	*268*
2	*Veil*	*ET205*	*8*
1	*0°*	*Tenax®-E IMS65 E23 24K 830tex*	*268*

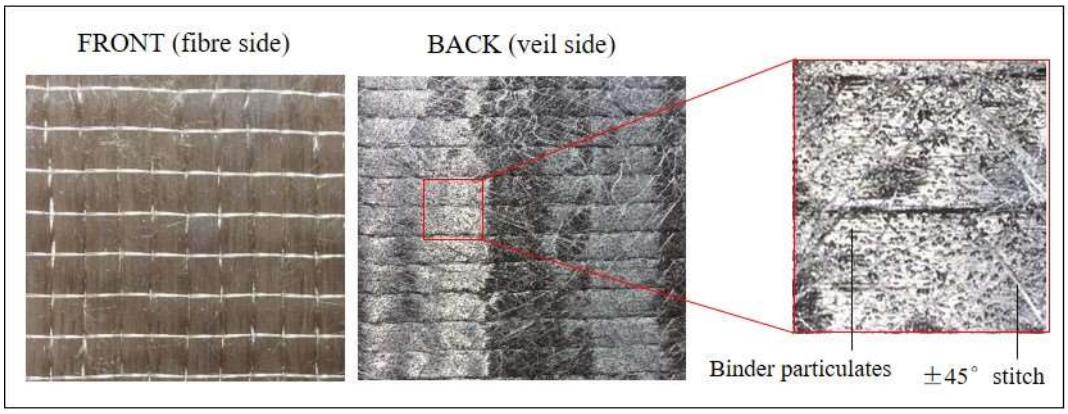

Figure 4.2: Images of the NCF material highlighting the reduced prominence of the ±45° stitch obscured by the veil. The presence of binder particulates (magnified image) and the greater significance of the stitch on the fibre side are also presented.

4.1.1 MICROSCOPY METHODS

Digital 3D microscopy was carried out using a Keyence VHX-6000 microscope, fitted with a VH-Z20R/W/T lens. Images were subsequently analysed and plotted using Matlab.

Field Emission Scanning Electron Microscopy (SEM) was undertaken using a JEOL JSM-6301F. A low accelerating voltage of 5 kV was used in secondary electron imaging mode. NCF samples were sputter coated with 20 nm of conductive Cr film using the pumped coater Quorum Q15OTS before allowing the samples to degas under vacuum for 24 h before scanning. This chromium layer dissipates charge build up and prevents overly bright images.

4.1.2 MICROSCOPY ANALYSIS

Optical microscopy revealed key differences in the topology of the front and back faces of the NCF. *Figure 4.3* shows the measurements undertaken and reveals the key differences between each side of the material. The fibre side stitches were shown to be more prominent as expected, with the fibres (along the length) comparatively smooth. This is in contrast to the veil side. Here, additions such as the randomly orientated chopped stand toughening veil and the polymer binder provide further surface roughness than carbon fibres alone. This in turn means that the $\pm 45°$ stitches on the veil side are much less prominent. With the single yarn stitch amplitude similar to the amplitudes of the veil and binder.

SEM micrographs of the material are presented in *Figure* 4.4a-h and highlight the complexities at various length scales. The fibre side of the material (*Figure* 4a –b) exhibits few features other than the stitches. The veil side, *Figure* 4c –d, shows the additional elements within this NCF, namely the polymer binder, which shows evidence of pre-curing at room temperature, *Figure 4.4e* and *4.4f.* This binder pre-curing is most notable as the binder appears to have fractures. The veil is applied beneath the stitches and shows the more random nature of the surface morphology. The micrographs also reveal the fibre to be around 7 μm in diameter (see *Figure 4*g), around

a tenth of a human hair. They also show evidence of shear compression in *Figure 4.4h* which evidence the cut line made by the shears in sample preparation.

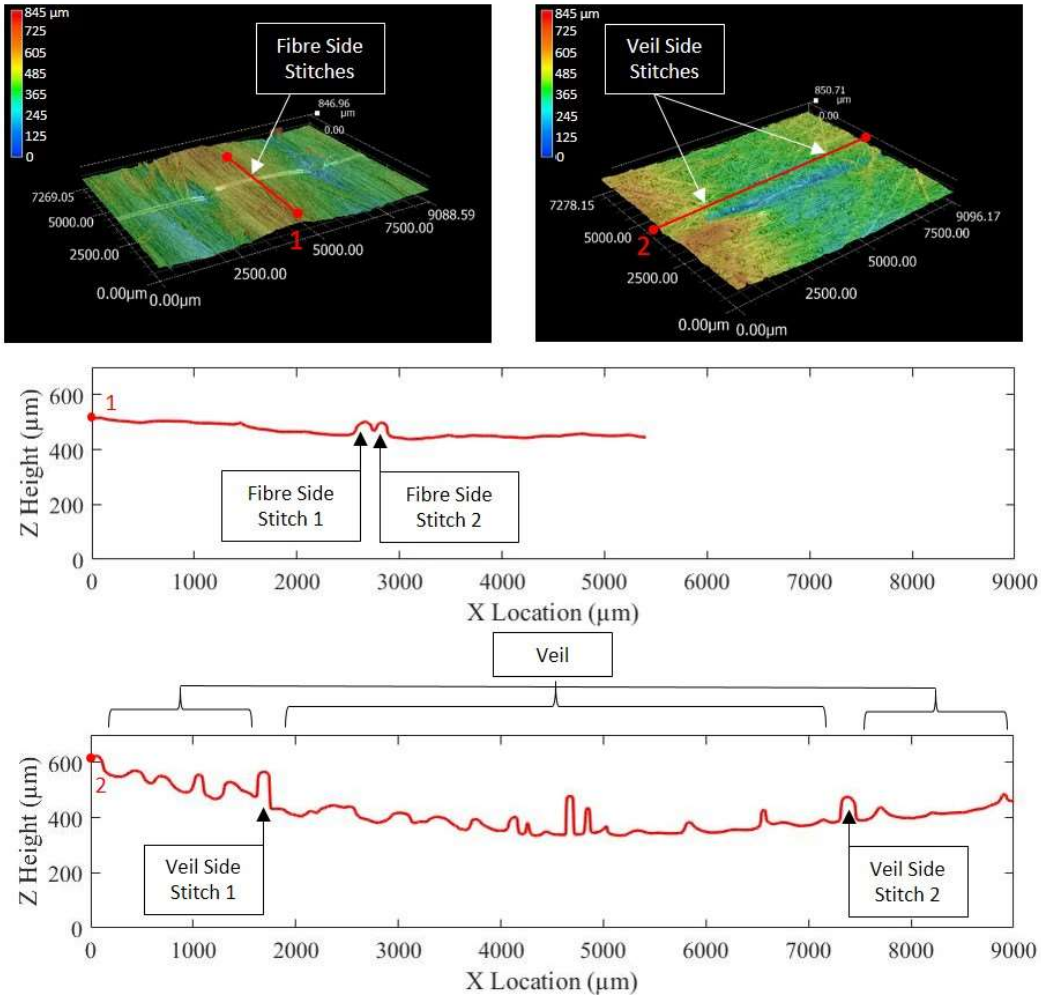

Figure 4.3: Optical microscope result. Top images show the microscope path in red, with the bottom two graphs revealing the differences in the Z height measurements and the prominence of the fibre side stitches in comparison with the veil side.

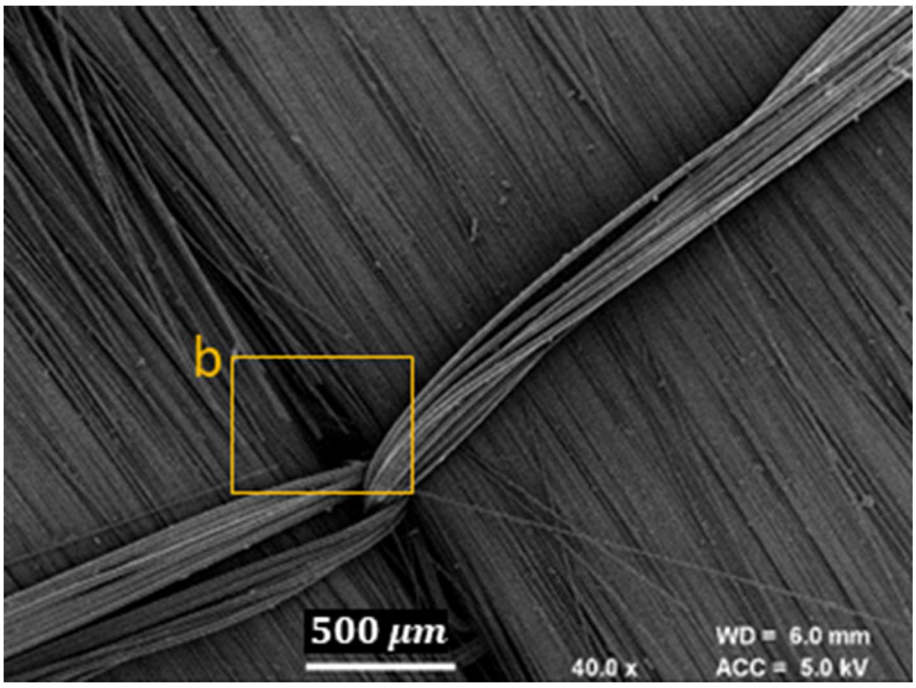

Figure 4.4a: SEM micrograph of the studied NCF showing the fibre side carbon tows highlighting the stitch loop and pillar stitch. The highlighted box indicates Figure 4.4b.

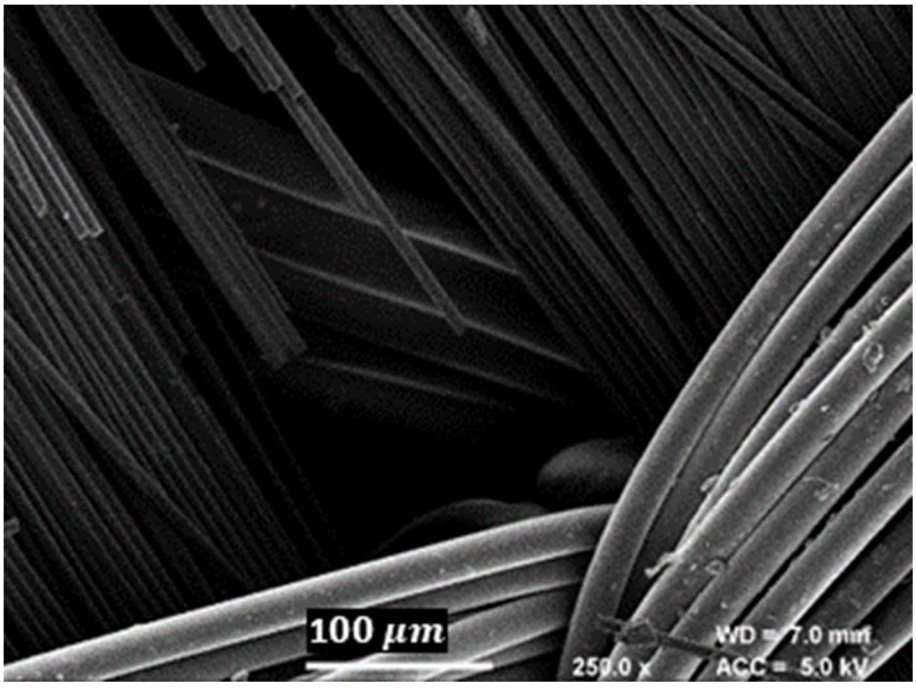

Figure 4.4b: SEM micrograph of the studied NCF showing a 5× magnification of the stitch point in Figure 4.4a with broken fibres in the background, likely caused by the stitching needle during fabric manufacture.

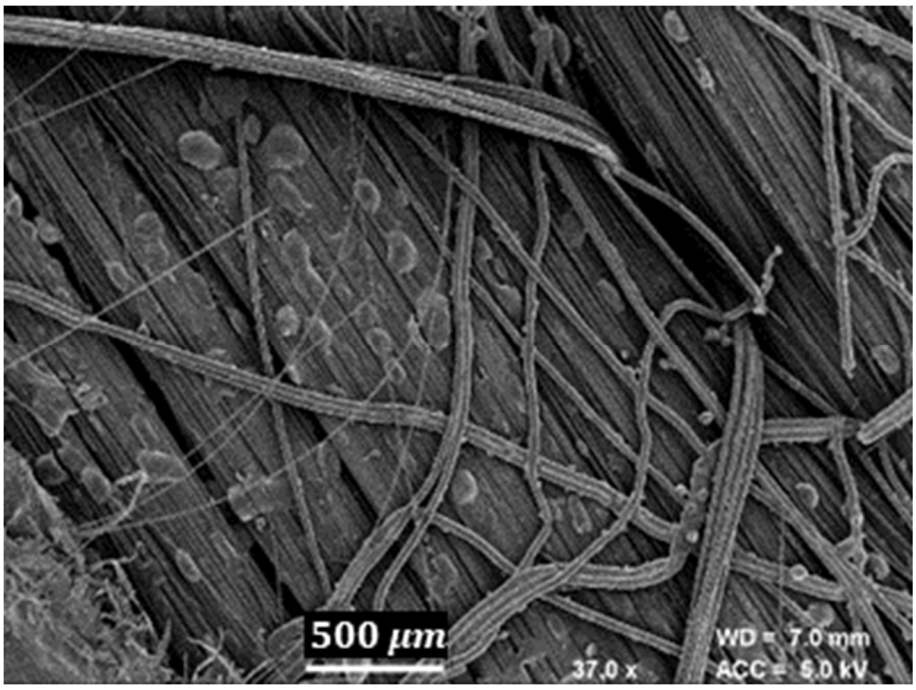

Figure 4.4c: SEM micrograph of the studied NCF showing veil side carbon tows with tricot stitch, veil and binder.

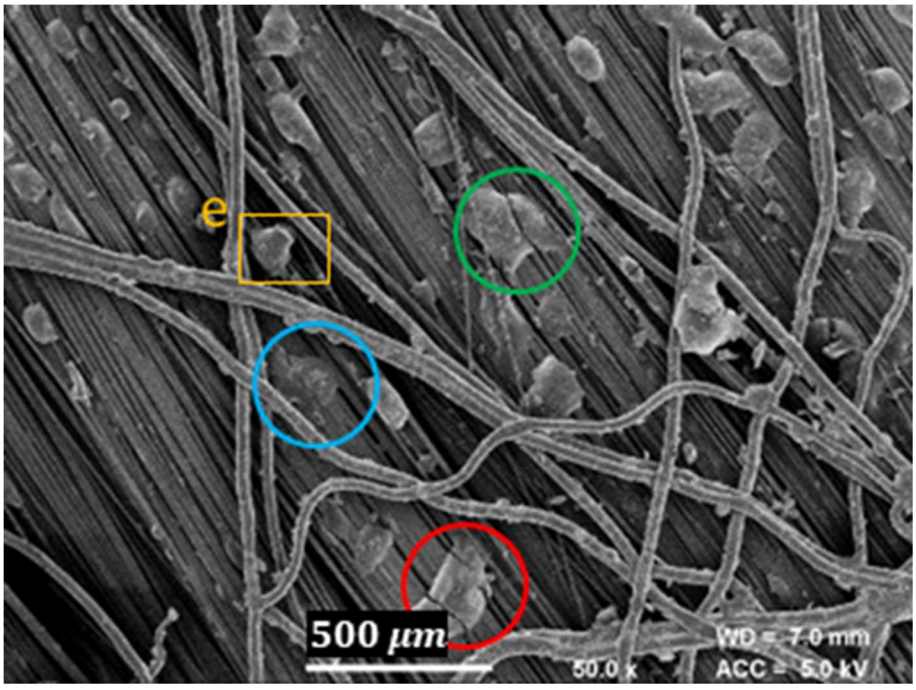

Figure 4.4d: SEM micrograph of the studied NCF showing veil side with evidence of binder polymerisation.

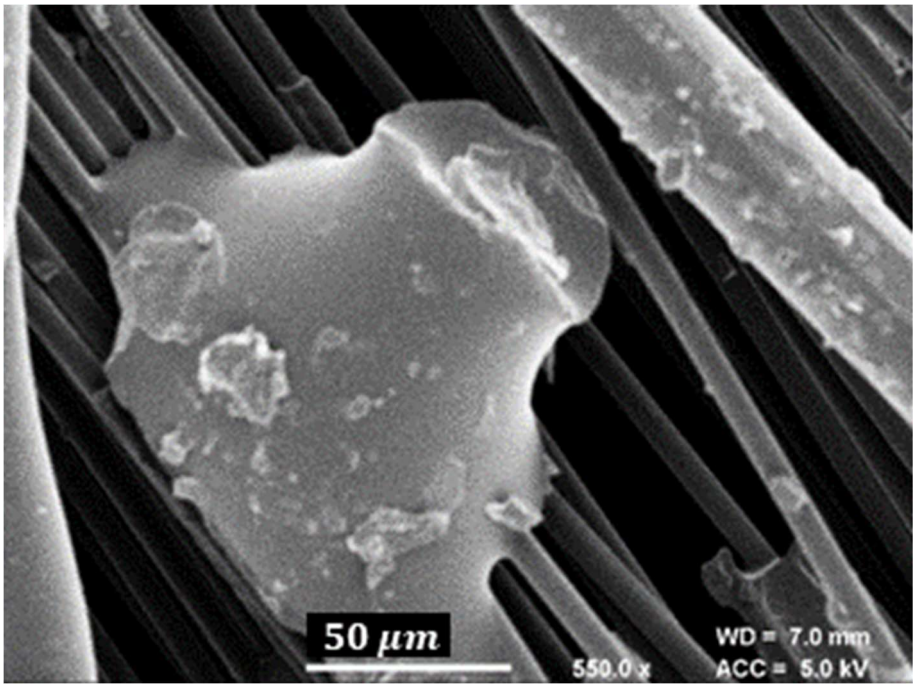

Figure 4.4e: SEM micrograph of the studied NCF showing binder particulate appearing to merge with the fibre sizing.

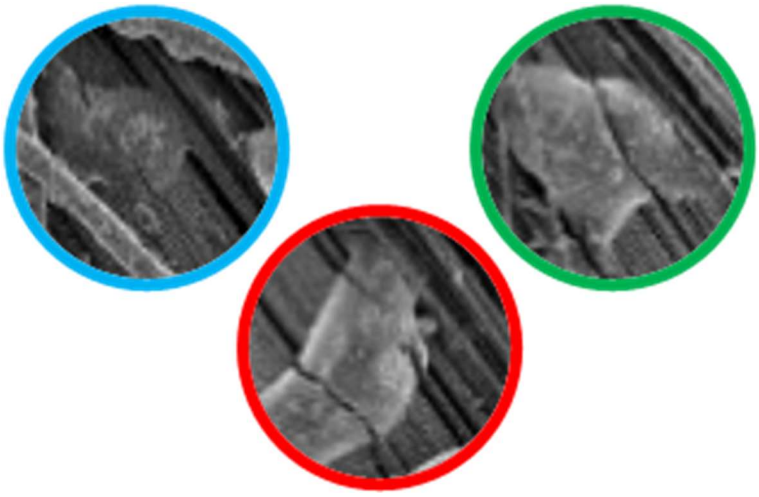

Figure 4.4f: SEM micrograph of the studied NCF showing colour coded 2 × magnification of (Figure 4.4d),

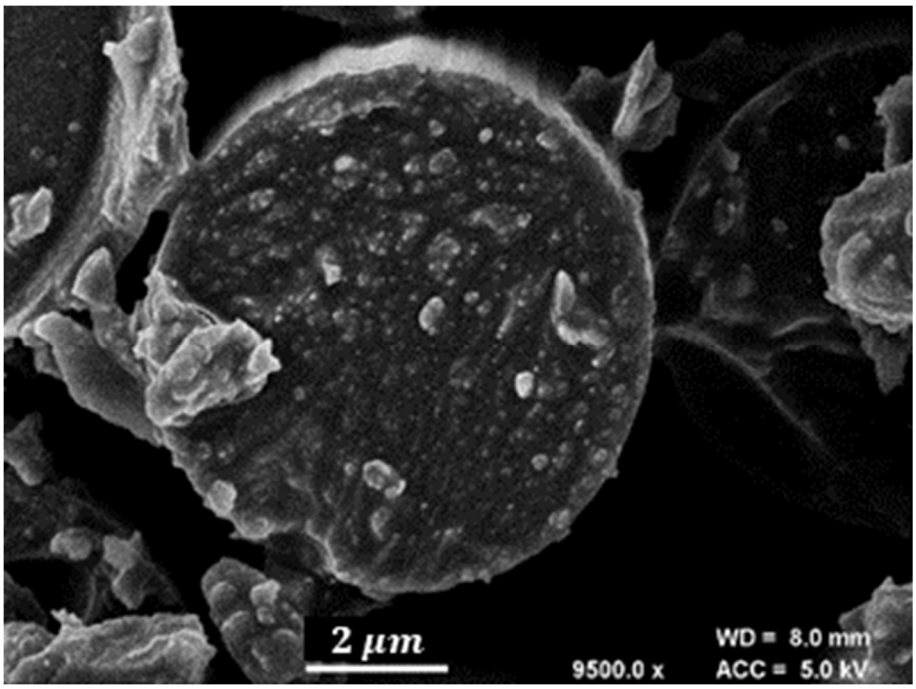

Figure 4.4g: SEM micrograph of the studied NCF showing cross section of a carbon fibre with a diameter of approximately 7 microns.

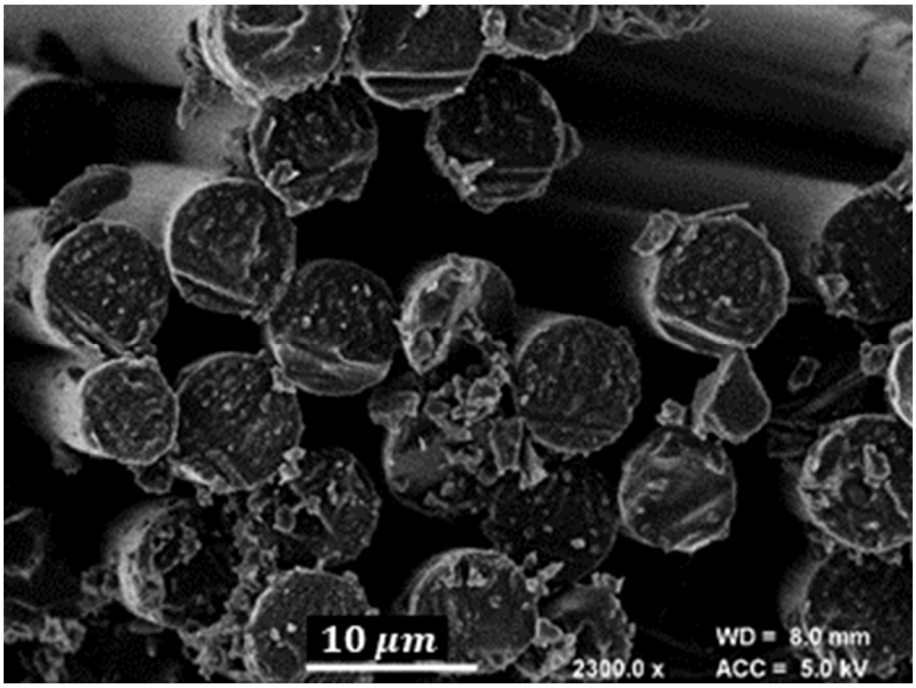

Figure 4.4h: SEM micrograph of the studied NCF showing cross section of the carbon fibres with evidence of shear compression indents from sample cutting.

4.2 INTERPLY SHEAR –THE ROLE OF FRICTION

Investigating interply shear is essential to understanding the role of friction in the chosen biaxial NCF. This is particularly useful in appreciating the material's frictional anisotropy, which may be affected by the additional components such as the stitches and veil. As described in detail in *Section 3.5,* interply shear describes the in-plane shear response between plies (fabric-fabric) and also between tooling and the plies (tool-fabric). Governed predominantly by the frictional response at these interfaces, it allows for an understanding of how different plies of material will slip and shear over each other.

Towards this purpose, experimental interply shear testing was undertaken following Erland's (2016) [11] protocol, using the same test rig and adjusting it for use with NCFs. As this work is focused on informing manufacturing in the aerospace domain, a complex NCF was used, which includes a toughening veil and binding agent, as was set out in the previous) colour coded 2 × magnification of (d), sections. In this work, fabric-fabric interply shear, and thus the interfaces' coefficient of friction, was evaluated. The study sets out a bi-linear approximation method and highlights that the stitch architecture plays a dominant role in frictional anisotropy.

4.2.1 INTERPLY SHEAR BACKGROUND

In the first instance, an appropriate friction model for the material system must be selected. It may seem plausible to use the Coulomb friction model (see *Equation 4.1).* Here τ_c equates to the critical shear stress, the point at which friction transitions from static to kinetic friction, μ is the coefficient of friction and σ_n the normal stress or pressure. However, it was identified [11] that this model did not capture the pre- and post-yield responses effectively, as the Coulomb model approximates the frictional response as an averaged linear response, highlighted in *Figure 4.5.*

$$\tau_c = \mu\sigma_n \tag{4.1}$$

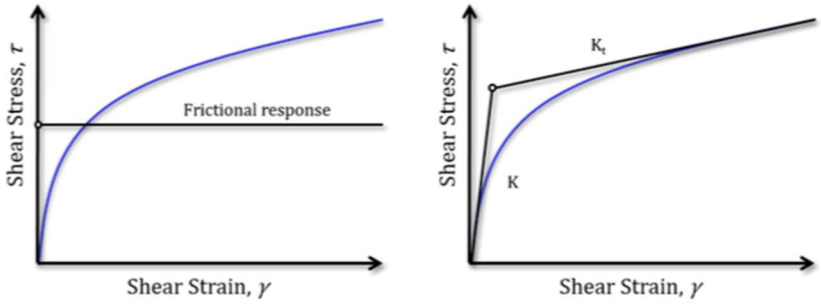

Figure 4.5: (Left) Coulomb linear friction model and (right) bi-linear approximation of the stress strain curve from the frictional response of the material, highlighting the increase in precision of the response opposed to the linear model [11].

The model shows that as σ_n reduces to 0, the resistance to shear also reduces to 0. This did not characterise the resistance to slip in Erland's results, which was identified as the adhesive behaviour of the resin. In NCF materials, no viscous resin interface is present, although as the fibres are bundled in tows, some elasticity is to be expected, as compaction of fibres and fibre meshing is present, even at low pressures. To better characterise the experimental results, the Mohr-Coulomb yield criterion (*Equation 4.2*) can be used, which is also valid in the interpretation of NCF interply shear results.

$$\tau_c = \tan\phi_\mu \sigma_n + j \tag{4.2}$$

The Mohr-Coulomb yield criterion, where j represents the joint strength, in this instance the resistance of the NCF to slip and ϕ_μ the angle of internal friction, calculated from the failure angle on a plot of shear stress against normal pressure, see *Figure 4.6.* The coefficient of friction thus equates to $\mu = \tan\phi$, allowing the coefficient of friction to be calculated from varying normal pressures through *Equation 4.3*:

$$\tau_c = \mu\sigma_n + j. \tag{4.3}$$

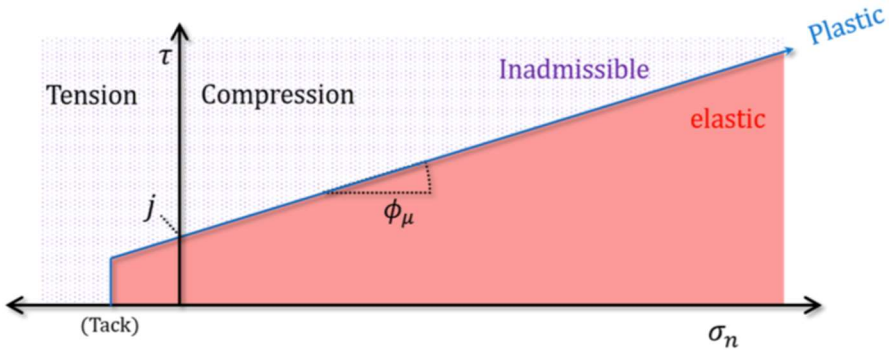

Figure 4.6: Plot of critical shear stress vs. normal pressure. With joint strength, j, and internal friction angle, ϕ_μ, [11].

This model therefore allows the coefficient of friction and the resistance to slip to be calculated respectively.

4.2.2 INTERPLY SHEAR METHODS

All tests were carried out using the NCF material set out in *section 4.1*. The interply shear test rig developed in [11] at the University of Bath, was employed in this research, with modifications to facilitate the new material system. *Figure 4.7* shows a schematic of the rig that isolates the frictional response of the material.

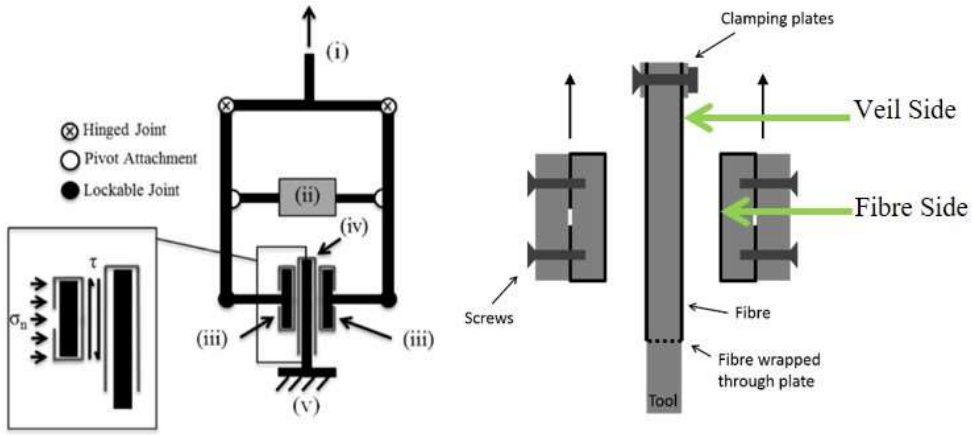

Figure 4.7: Interply shear experimental set-up [1], green arrows added to highlight interface conventions.

As described by Erland: "Firstly, a lockable hinged array connected to an Instron load cell at (i), consisted of a pneumatic cylinder (ii) which pulled together two plates (area, A = 50×50 mm^2) wrapped in a single layer of carbon fibre prepreg (iii). These plates clamped either side of a central plate (area, A2 = 100×150 mm^2) (iv), also wrapped in a layer of carbon fibre prepreg, which was fixed to the bottom mounting of an Instron testing machine (v)".

The test scheme employed in this work is identical except from the use of NCF instead of prepregs.

Masking tape was used on the perimeters of specimens prior to cutting with a rotary cutter, allowing the stitches and fibres to be held in place. Holes were then punched from the specimens to allow clamping to the plates. In the moving plates, clamping was always fixed in the pulling direction. *Figure 4.8* shows the specimen preparation regime employed, highlighting the masking technique used, with the plates shown in *Figure 4.9*. Specimens were cut to provide 0°, 45° and 90° fibre directions by using a set square, allowing assessment of diverse interface angles and also evaluation of different stitch angles on the fibre side.

To facilitate assessment of interface angles, in line with the literature, the pulling direction of the rig was used as the reference, *Figure 4.10*. This means that on the fibre side, 0° fibres are in the axis of the pulling direction, with ±45° representing the angle of the fibre from the reference and similarly 90°, the fibre direction from the reference. On the veil side, the fibre direction was also used, following the same procedure with the pulling direction as the reference; *Figure 4.11* illustrates the reference directions.

The protocol for calibrating the rig involved testing a material with a known coefficient of friction, PTFE, and comparing this to the range found in the literature. The test showed a value of 0.05, which was within the range of 0.05-0.10 [82]. A digital pressure gauge was chosen to replace the previous analogue version. This allowed a more consistent confining pressure. A 1 kN load cell was also used as it has a higher degree of precision over the low loads expected. Samples were kept at room temperature for the duration of the tests.

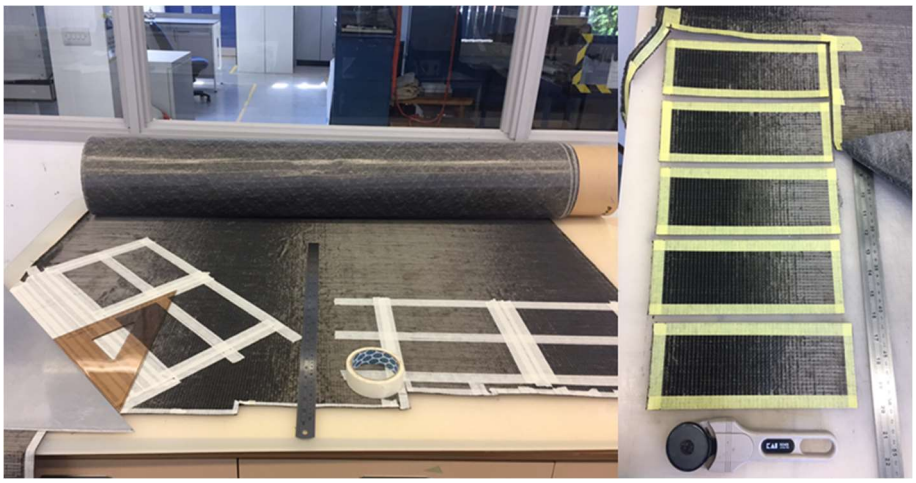

Figure 4.8: Images showing the fixed specimen masking preparation, allowing the boundaries to be fixed prior to cutting with a rotary blade. Subsequently, holes were punched from the specimens to allow clamping to the fixing bolts and to as not disorientate the fibres.

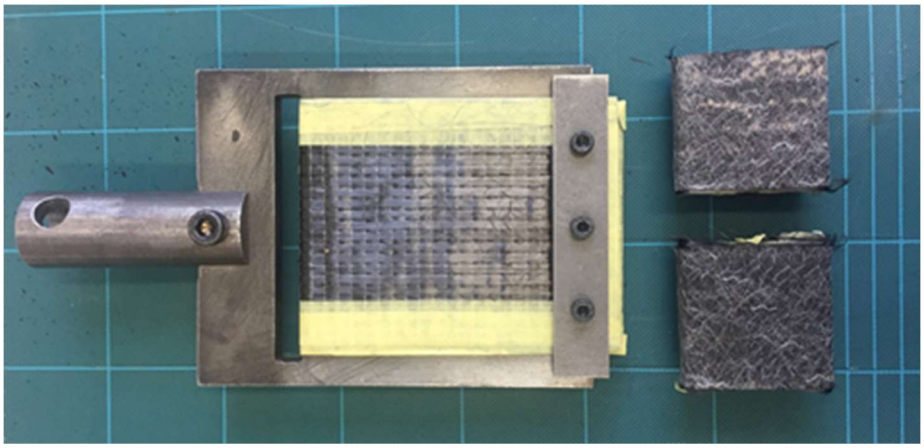

Figure 4.9: Image of the specimens clamped onto the plates. (Left) highlighting the fixed plate clamping regime and (right) showing the movable plates regime.

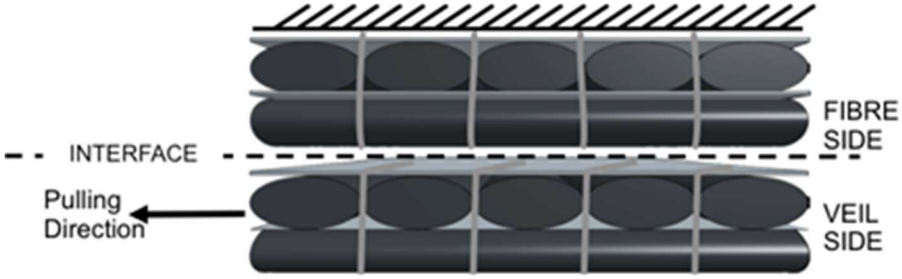

Figure 4.10: Schematic of the interface with specimens clamped onto the plates.

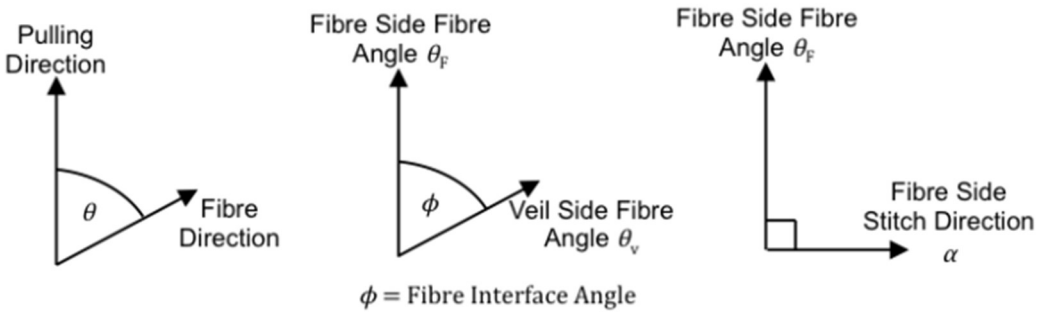

Figure 4.11: Reference directions for fibre, interface and stitch directions.

A consistent masking regime was also employed to fix sample boundaries and facilitate clamping. All samples were further checked for consistency, with stitch integrity and veil application ensured.

4.2.3 INTERPLY SHEAR TEST PROCEDURE

The test procedure was as follows: First the normal clamping force, σ_n, was achieved by way of a digital pressure gauge on a regulator valve feeding the pneumatic cylinder. An *Instron 3369* tensile testing machine then pulled the upper portion of the rig from point (i) at a constant rate of 0.1 mm/min, whilst the load cell recorded the force, F. Tests were conducted at three confining pressures: 17 kPa, 35 kPa and 70 kPa to allow calculation of the coefficient of friction.

These pressures also allow interply shear to be better understood under pressures that are more in line with what is to be expected from DF [11]. This would also facilitate a valid representation of the linear response expected from the plots of critical shear stress *vs*. confining pressure. The fibre side was always fixed to the central plate and the veil side was always fixed to the two pulled plates, identified in *Figure 4.9.* The test specimens are identified in *Figure 4.12,* where they are designated in accordance with

fibre directions on the two opposing contact surfaces, so for a fibre interface of 0//v45, a 0° fibre was aligned on the fibre side, and a 45° fibre was aligned on the veil side, with the 'v' designating the material with the veil on the surface. The test 0//v0 was repeated 3 times, and 0//v90 repeated twice.

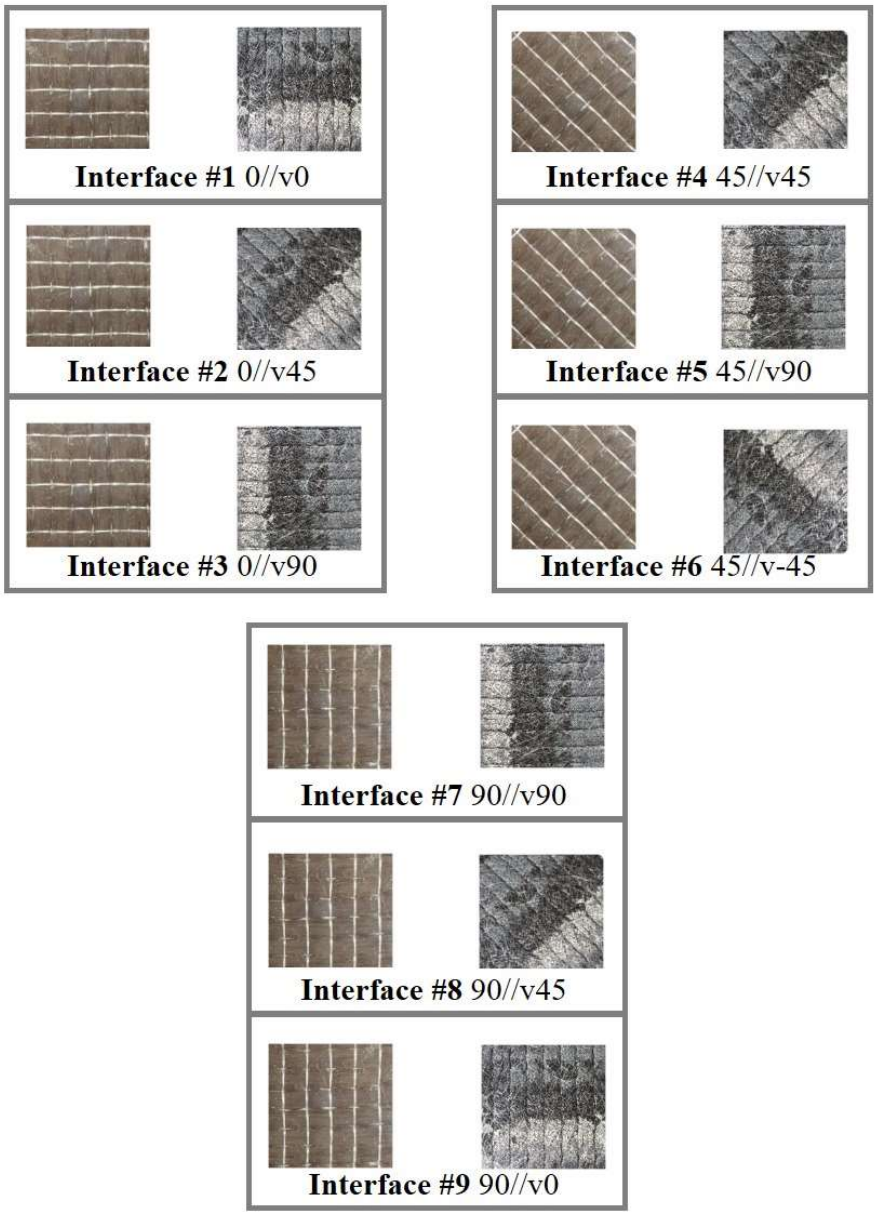

Figure 4.12: Test specimen regime and naming conventions for interply shear testing.

4.2.4 INTERPLY SHEAR RESULTS AND DISCUSSION

The shear stress strain plots obtained from the experiment were qualitatively comparable to those for a prepreg material [11], with an initial steep increase in shear stress. This allowed a bilinear approximation to be used to evaluate the critical shear stress. *Figure 4.13* (top-left) shows a shear stress strain curve for the [0//v45] interface, for the three confining pressures. It follows the expected behaviour with increasing

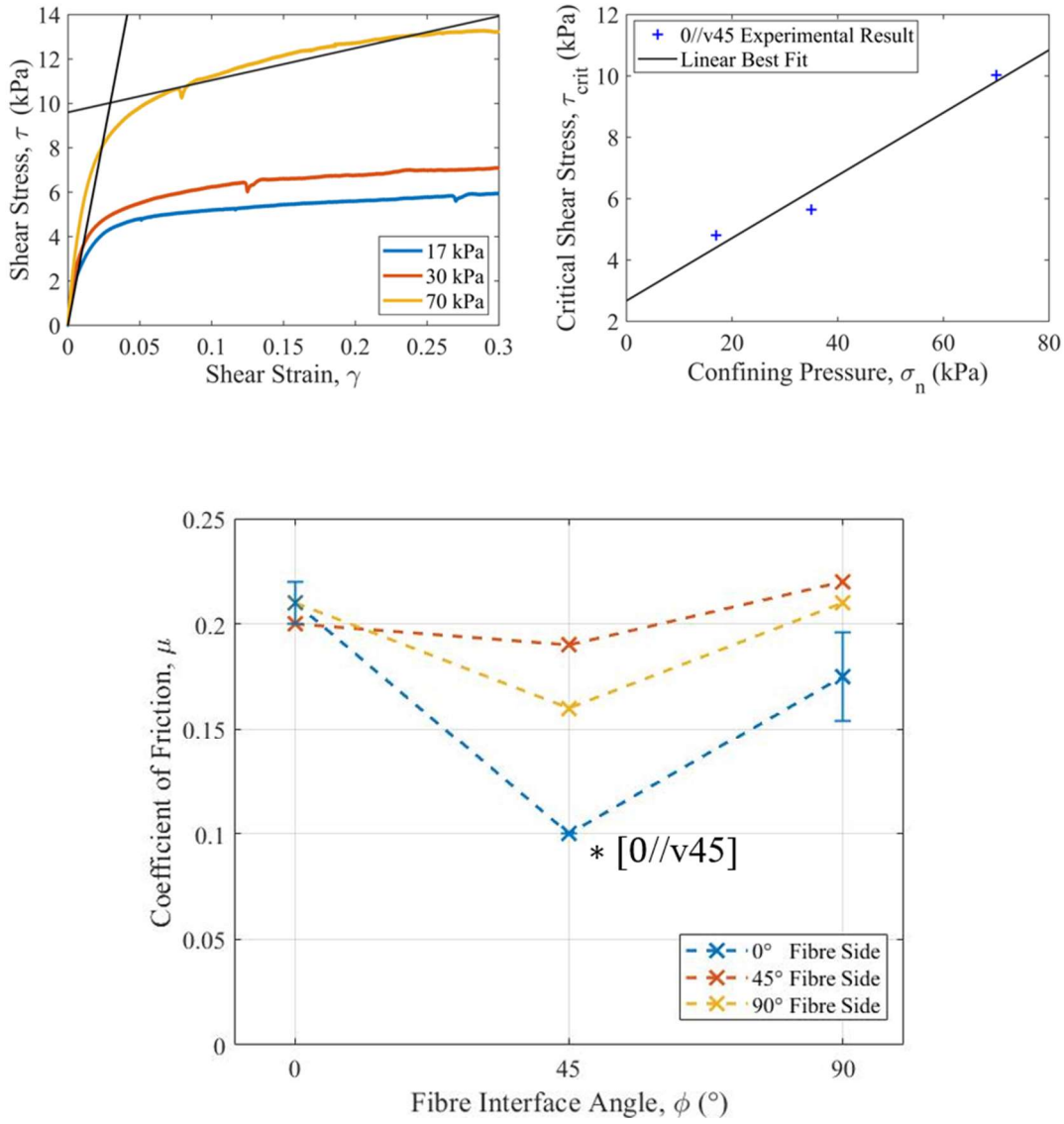

*Figure 4.13: Top-left, interply shear response for [0//v45] interface for the three confining pressures studied. Top-right: Subsequent plot of critical shear stress for the [0//v45] interface. Bottom: All coefficient of friction results with the [0//v45] result indicated with a *.*

shear stress with increasing confining pressure. The critical shear stress is also shown, with the data series split into two, allowing linear trend lines to be fitted and the value obtained. These results were found to follow the same trend for all tested specimens, with the three values for different pressures plotted against the confining pressure. *Figure 4.13 (top-right)* highlights this plot for the same specimen, and shows that by fitting a linear trend line, the coefficient of friction can be obtained from the gradient.

From *Figure 4.13 (bottom)* the coefficient of friction, μ, for all interface angles was found to be between 0.10 and 0.22. These results are comparable with results from Avgoulas *et al.,* (2018) [44], where values were reported around 0.16-0.28 for a carbon NCF in contact with a forming tool. What is evident is that μ reduces in magnitude as ϕ reaches 45° for all fibre directions, whilst when ϕ is 0° or 90°, μ is comparable. This could be due to reduced contact area, as at an interface of 45°, fibres or stitches are not aligned, thus reducing contact. Further, for the specimens with fibre side = 0°, a reduction in the friction coefficient is observed relative to the others.

These results are consistent with [33, 44], where it was shown that less contact area, thus less friction is expected at interfaces that cannot mesh. At the 45° interface there is always a mismatch between the stitch or fibre direction, opposed to the 0° or 90° interface which always has, at minimum, the stitch in the same direction as the fibre. Results from [11] where μ decreased with increasing ϕ as a result of more efficient load transfer, were not upheld in the NCF results here. It is likely that the reason for this is that with this NCF material the stitch is always the inverse direction of the fibre, providing a dominant effect, where as in a prepreg no stitches are present. This further highlights the complexity that stitching yarns present in forming, with significant divergence from the theory of prepreg materials. Interply friction should therefore be considered not only from the influence of the fibre direction, but also from that of the dominant stitch direction.

4.2.5 INTERPLY SHEAR SUMMARY

These results emphasise the complexity of carbon NCFs and their differences when compared to woven or prepreg systems. This new evidence offers understanding regarding the influence of the stitching yarns on the coefficient of friction. This is most significant on the fibre side of the interface, with the stitching perpendicular to the fibre direction. Thus, the stitches must be considered as a key determinate of the forming characteristics of the material. Further supplementary studies are needed that can allow for more quantification of the effect, particularly if the full anisotropy is to be modelled. Microscopy revealed the prominence of the fibre side stitch. This topology, contrasting with the veil's random nature, influences the frictional response. The addition of the binding agent could also contribute, with larger contact area expected as a result. Contact analysis of the interface could allow for better understanding of the mechanics of interply shear, however, quantification is challenging in complex systems such as these. Future studies may benefit from employing pressure sensitive films to characterise the true contact area of the interface.

4.3 BENDING BEHAVIOUR OF BIAXIAL NCF

Out-of-plane bending and its contribution to wrinkling is understood to be a major determinate of wrinkling severity. This is particularly pertinent in NCFs, as the complex material architecture influences the material anisotropy and includes further variables than woven comparators; such as the stitch pattern, veil, binder, stitch spacing, ply thickness and stitch tension.

4.3.1 BENDING BEHAVIOR METHODS

To evaluate the bending response, Shirley cantilever tests [83-88] are widely performed according to BS EN ISO 9073–7; 1998 [84] allowing the calculation of the bending stiffness per unit width, G, where M is the weight per unit area and l is the bending length:

$$\mathrm{G} = \frac{Ml^3}{8}. \tag{4.4}$$

To perform accurate bending characterisation, an apparatus for measuring the bending stiffness was designed and fabricated following the schematic in *Figure 4.14*. The test-rig developed was laser cut from 3 mm MDF and utilised an acrylic slider in place of the standard steel rule to allow for testing wider samples. A fixed tilted board, at 41.5°, was employed following the standard method to allow for ease of measurement. Rectangular strips (30 x 250 mm) were used for warp and weft orientations and strips of 100 x 250 mm in the bias direction to reduce in-plane shear or edge effects from stitch degradation [89]. Masking tape was used on the perimeters of specimens prior to cutting with a rotary cutter, allowing the stitches and fibres to be held in place. Six test repetitions were performed to eliminate the influence of experimental variability and strip displacement was measured using a steel rule. Whilst this method cannot evaluate non-linear bending [86], it offers an approximate representation for the secondary material deformation mechanism and is still the most popular method for bending characterisation of non-woven fabrics.

4.3.2 BENDING BEHAVIOR RESULTS AND DISCUSSION

The bending experiments showed that the veil and stitch architecture influenced the out-of-plane mechanics. This can be evaluated in *Figure 4.15-4.16*, orientation 2, whereby having the 0° fibres on the top surface gave a bending stiffness 57% lower than orientation 3. This is not only attributed to displacing the longitudinal fibres

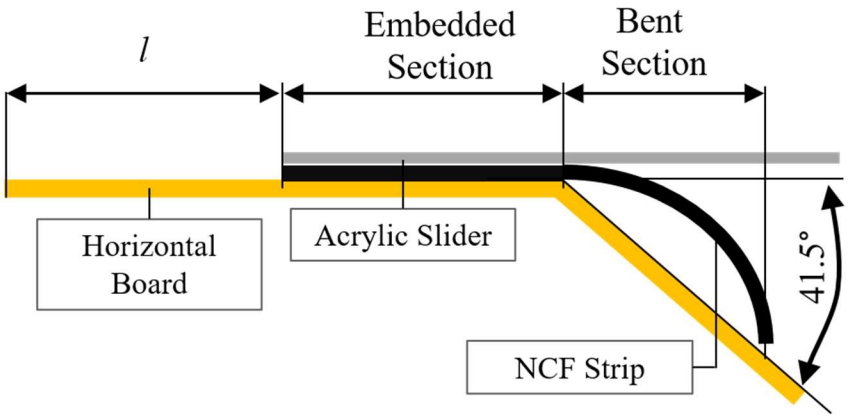

Figure 4.14: Shirley cantilever experiment schematic with the NCF (black), cantilever boards (yellow) and acrylic slider (grey).

0.5 mm above the fulcrum, but also to the addition of the veil and binder. When the veil sandwiched a 90° fibre layer on the compressive bending region, as in orientation 4, it acts as a stiffener in preventing rotations of the tows. When the veil was removed from this location, see orientation 2, the 90° tows were free to rotate within the compression of the tricot stitch. This led to a 47% reduction in bending stiffness. This can also be seen in *Figure 4.17,* where orientations 2 and 3 are shown. In orientation 2, the 90° fibres are below the midline and have one free interface, allowing the tows to rotate and compact during transverse bending, reducing the bending stiffness of the specimen. In orientations 1 and 3, the effect of the veil is not evident, this is because the 0° fibres are below the midline and in compression, thus don't undergo the same rotation and compaction as the 90° fibres in orientation 2 and 4. Orientation 5 is also stiffer than orientation 6, which is likely attributed to the difference in the stitch architecture on the front and reverse of the fabric. This shows the veil and placement of fibres in relation to the midline are important factors in transverse bending.

It was previously discussed in *Section 4.1* and *Figure 4.4*e and *4.4f* that the binder particulates appear to have partially cured and fused with the fibre sizing. This would increase the in-plane compressive stiffness on the mesoscale, allowing load to transfer between the 90° and 45° fibres when in compression (see *Figure 4.16,* orientations 4-5). Without the binder or veil, compressive stiffness originates from the stitch. This may have important implications for macroscale homogenisation strategies that aim to capture the full effect of the anisotropy.

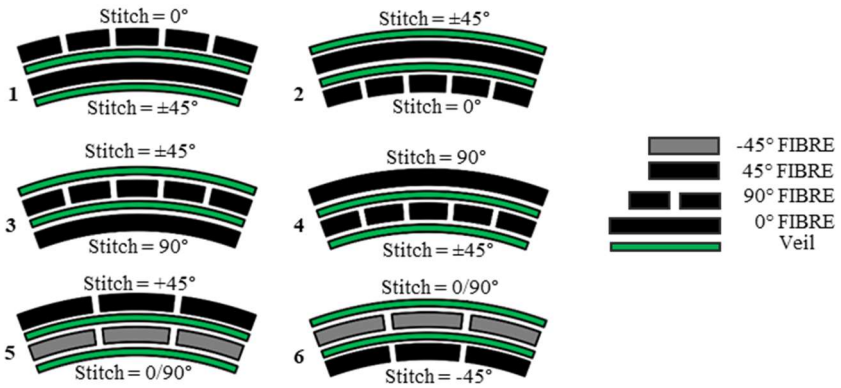

Figure 4.15: Bending orientation schematics. Six samples were tested in each orientation and the bending stiffnesses were calculated.

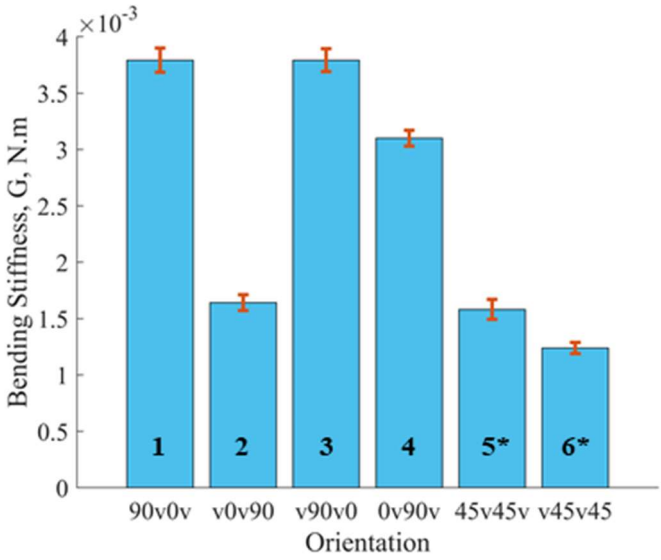

*Figure 2.16: Bending stiffness results for the six sample orientations, The red bars indicate the standard deviation for the six measurements. * Wider samples (100 mm) for bias orientation.*

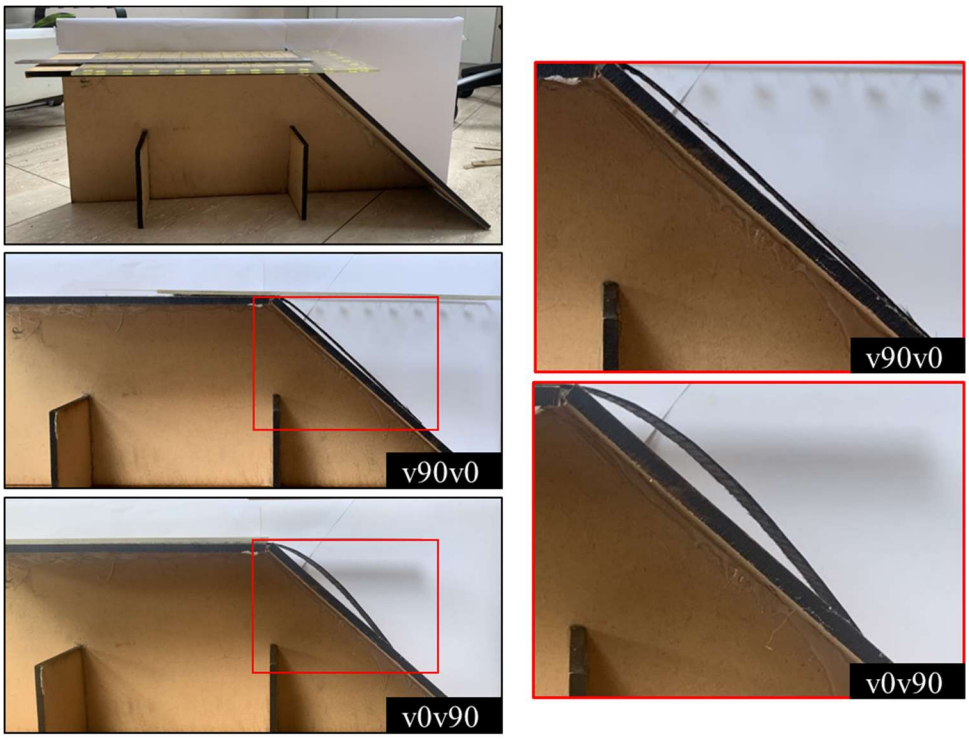

Figure 4.17: Bending experiments for v90v0 (orientation 3) and v0v90 (orientation 2). Highlighting the differences in bending when the fibre tows below the midline are permitted to rotate.

4.4 INTRAPLY SHEAR – BIAS EXTENSION

Biaxial carbon fibre fabrics do not readily deform along the fibre axis, due to the near inextensibility of carbon. In biaxial fabrics, the *bias direction,* refers to the axis at the midline between both warp and weft directions. Deformation is instead predominantly governed by in-plane shear deformation in the bias direction. This is facilitated by rotations about the pillar stitch which allow the material structure to stretch through in-plane shear without fibre strain. This is illustrated in *Figure 4.18*, where the tricot pillar stitch promotes rotations about the black sections of the stitch. As was discussed in the literature review, two experimental techniques are typically chosen to elucidate this property. In this work, bias extension experiments were deemed appropriate for the chosen material. Bias extension tests rely on isolating a portion of the material and deforming it through pure shear. This involves clamping a rectangular specimen, with a minimum aspect ratio of 2, with the fibres orientated initially with the midline coincident with the pulling direction.

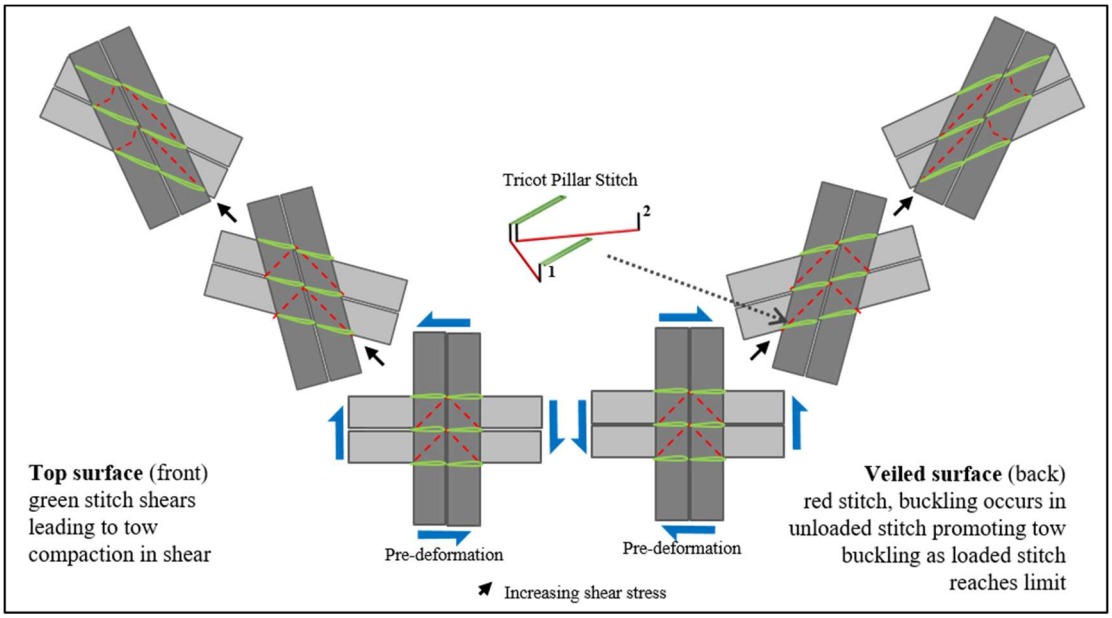

Figure 4.18: Intraply shear through tricot-pillar stitch deformation. Unit cell of stitch inset with the near symmetrical shear pattern due to the material architecture present in the biaxial NCF studied.

4.4.1 INTRAPLY SHEAR METHODS

Bias extension tests with an aspect ratio of 2 were conducted according to the method described in [90, 91] on an *Instron 3369* tensile testing machine. The specimen had dimensions of 120 x 240 mm. Larger specimens are beneficial in reducing likely edge effects arising from stitch rupture. The specimen followed the conventions set-out in *Figure 4.19*, with the central region, C, undergoing pure shear during the test.

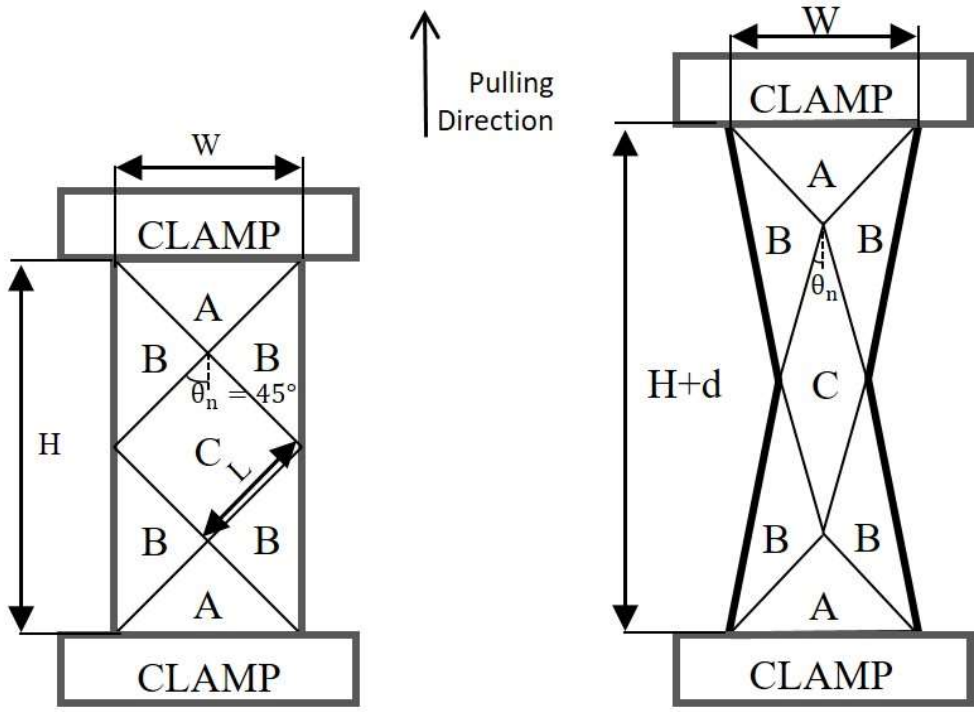

Figure 4.19: Bias extension specimen schematic pre- and post-deformation. Region C undergoes pure shear when the sample is orientated with the fibre ±45° to the pulling direction. Region B will have half the magnitude of shear deformation as region C and region A should undergo no deformation.

Samples preparation was rigorous to ensure fabric integrity, masking the periphery prior to cutting with a rotary cutter. Prior to this, lines were drawn on to the fabric in the same layout as *Figure 4.19*, using a white paint marker. This allows simple assessment of the shear angle and also can reveal any inter-tow slip. Clamps used in the experiment were fabricated with a central recess to reduce the potential for the fabric to slip in the clamps and allow for a fixed boundary condition. Three repeat measurements were conducted to allow for a reduction in any variability.

To determine the shear angle, γ, in zone C, the initial sample width, W, and the displacement, d, is assumed to satisfy the equation,

$$\gamma = 90° - 2\theta = 90° - 2\cos^{-1}\left(\frac{W+d}{\sqrt{2}W}\right). \quad (4.5)$$

Once the shear angle has been calculated, it is next appropriate to determine the shear force from the axial force, F. Following the standard rate-independent method [40, 42], the normalised shear force, F_{sh}, for region C can be evaluated through the iterative equation,

$$F_{sh}(\gamma) = \frac{1}{(2H-3W)\cos\gamma}\left(\left(\frac{H}{W}-1\right)\cdot F\cdot\left(\cos\frac{\gamma}{2}-\sin\frac{\gamma}{2}\right) - W\cdot F_{sh}\left(\frac{\gamma}{2}\right)\cos\frac{\gamma}{2}\right). \quad (4.6)$$

In this work, both of these equations were implemented in a purpose built *Matlab* script. Allowing the calculation of shear angle and shear force. The displacement, d, can either be taken directly from the Instron, or can be calculated through digital image correlation (DIC). DIC in itself is difficult to implement on carbon materials due to the reflectivity of the fibres, which is further exacerbated by their fibrous structure. 3D DIC was captured using two *LaVision Imager M-lite* cameras and *DAVIS* processing software, however automated image analysis was unsuccessful due to the earlier concerns. Manual image analysis using the 3D DIC reconstructions, was however amenable. *Figure. 4.20* shows the test set-up pre-test and during testing.

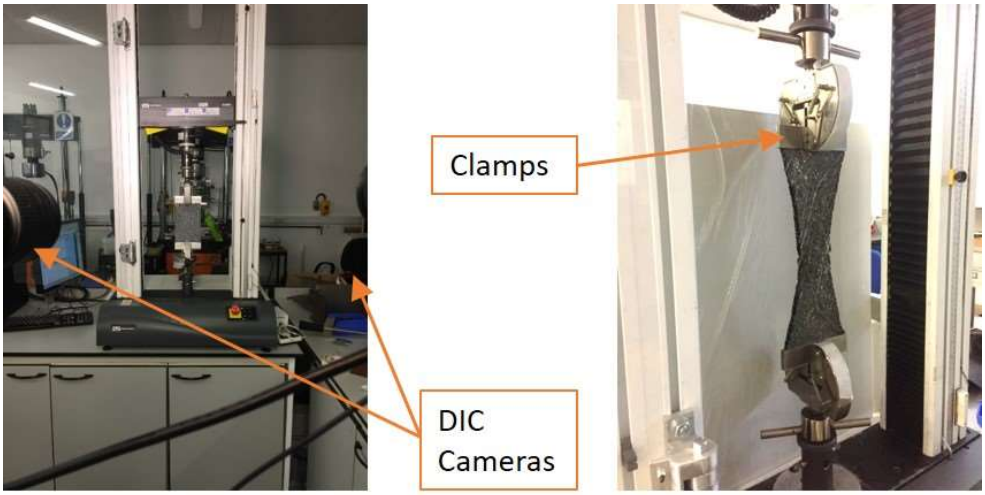

Figure 4.20: Bias extension test set-up before and during the experiment.

4.4.2 INTRAPLY PLY SHEAR RESULTS AND DISCUSSION

As was previously discussed, the fibrous nature of the NCF did not allow automatic DIC strain information to be gathered in this instance, hence axial strain information was based on output from the Instron, which included the displacement of the sample edge. The data from the experiment, showing the displacement and axial force values, is found in *Figure 4.21,* here the three experiments were smoothed using a moving average of 100. *Equations 4.5* and *4.6* were then used to determine the normalised shear force as a function of shear angle.

Using axial strain data from the Instron could produce an overestimate of the theoretical shear angle at high strains. This was evaluated using *ImageJ, (Fiji)* [92], to extract the shear angle and deviation from the theoretical value, *Figure 4.22*. However, as this deviation is also attributed to slip and edge effects such as stitch breakdown, the kinematic model was used as these would break the assumption of pure shear. While slip is not modelled, we can hypothesise that slip would occur between the shear angles of 30° and 60°. Whilst this study did not aim to develop a state-of-the-art material model, macroscale modelling results presented later highlight the efficacy of this simplification. The resulting normalised relationship between shear stress and shear

angle was fitted via *Matlab's* fitting toolbox as a rational polynomial. To allow the development of simplified hyperelastic behaviour at high strain, a second exponential fit was added to the shear stress formulation. As the majority of defect free deformation occurs before 40°, this will have little impact on the global deformation of the process models studied in this thesis. The shear stress, illustrated in *Figure 4.23*, therefore took the form:

$$\sigma_{12}\ (MPa) = \frac{P_1\gamma_{12} + P_2}{{\gamma_{12}}^4 + Q_1{\gamma_{12}}^3 + Q_2{\gamma_{12}}^2 + Q_3\gamma_{12} + Q_4} \qquad 0° \leq \gamma_{12} < 40° \qquad (4.7)$$

$$\sigma_{12}\ (MPa) = B_1{B_2}^{\gamma_{12}} + B_3 \qquad 40° \leq \gamma_{12} \leq 89° \qquad (4.8)$$

with coefficients,

$$P_1 = 1.382 \times 10^4,\ P_2 = 204.5,\ Q_1 = -83.9,\ Q_2 = 1009,\ Q_3 = 1.632 \times 10^5,$$

$$Q_4 = 1.176 \times 10^5,\ B_1 = 1.40784 \times 10^{-5},\ B_2 = 1.15916,\ B_3 = 0.09482.$$

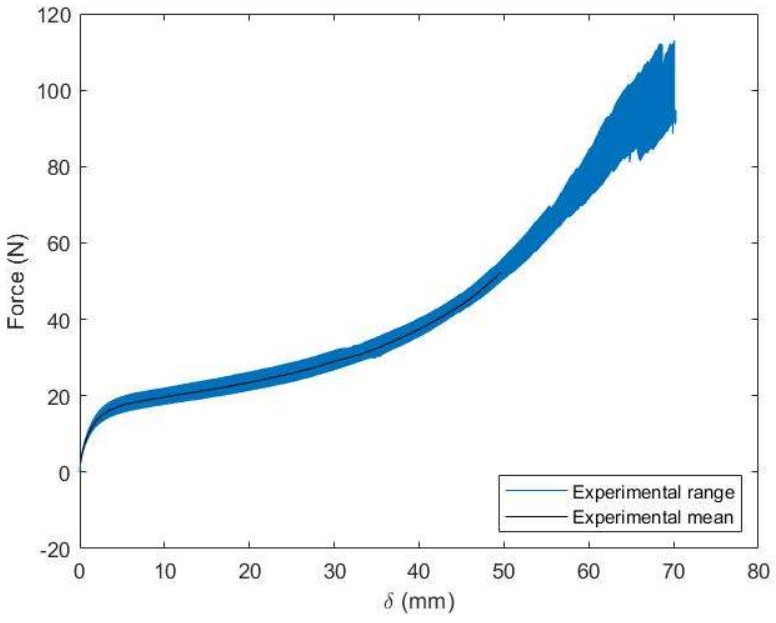

Figure 4.21: Bias extension experimental results of axial force and Instron displacement, combined results from three experiments.

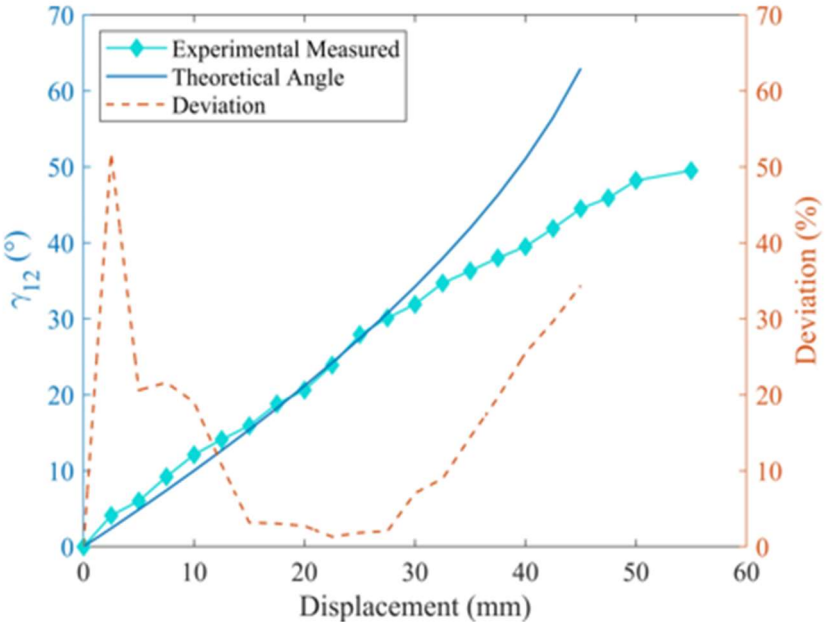

Figure 4.22: Shear angle vs displacement results for the bias extension data with the experimental measured using DIC data and the theoretical angle calculated through kinematic analysis using the Instron displacement.

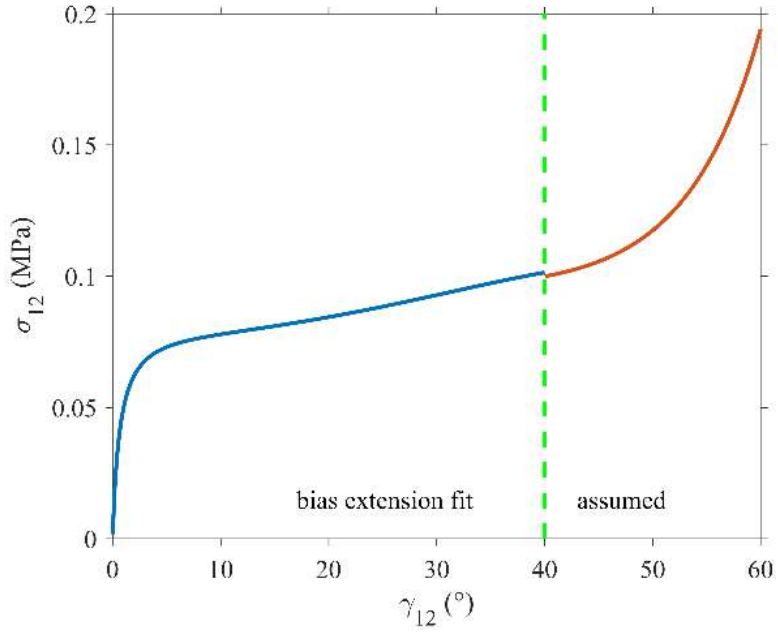

Figure 4.23: Shear stress as a function of shear angle. The blue curve is from the experimental analysis; the red curve is the assumed exponential function used to create the hyperelastic behaviour.

4.5 MATERIAL CHARACTERISATION CONCLUDING REMARKS

This chapter set out the complexity of a veiled biaxial non-crimp fabric through experimental characterisation of the major deformation mechanics: friction, bending and intraply shear.

Microscopic analysis of the [90/v/0/v] fabric revealed a highly anisotropic material with evidence of binder pre-curing and microscale manufacturing defects. The material architecture was also examined through 3D optical microscopy, where the prominence of the fibre side stitch in comparison with the veil side, highlighted the additional considerations needed when adding structural reinforcements such as the veil.

It was shown that the prominent fibre side stitches had a significant impact on the frictional anisotropy of the material. This was likely due to the increased contact area from the co-mingling of aligned fibres and stitches on opposing contact surfaces.

Characterisation of the veiled biaxial NCF also revealed complicated bending mechanics, with highly anisotropic bending stiffness. The veil was shown to act as a stiffener in bending, preventing the rotation of tows on the veil side of the material.

Finally, bias extension tests were conducted on the material. Due to the shear deformation mode facilitated by the stitches, intraply shear analysis revealed highly non-linear shear stress behaviour.

It is common to use these properties to develop complex computational models. Although, by first appreciating the material architecture, in particular the divergence from woven materials and the contribution of additional reinforcements, engineers will be equipped with the insight needed to develop efficient homogenisation strategies.

CHAPTER 5

NCF FEA MODEL

As was shown through material characterisation, NCFs are complex with highly anisotropic bending stiffness and non-linear non-orthogonal shear stiffness. The creation of valid computational models precedes the development of virtual strategies. This chapter first sets out the background and current state-of-the-art in finite element modelling, with an evaluation of different strategies found in the literature. Next the chosen approach, macroscale modelling, is developed using the results from *Chapter 4: Material Characterisation* and validated against the experimental data.

5.1 REVIEW OF MODELLING STRATEGIES

Simulation is a key tool towards understanding material behaviour and modelling process results. The commercial finite element analysis (FEA) package *Abaqus* is frequently used, making use of both membrane elements [93, 94] and shell elements [83].

Membrane models have the advantage of computational efficiency, but at the detriment of mechanical validity, particularly in forming protocols that include bending, whereas typical shell models overestimate the compressive stiffness. Novel developments to these models include the use of sub-modelling [95], coupled elements [87], laminated shell elements [86, 88] and more recently, coupled membrane and bending idealised shell models [96-99]. Despite these advances, however, accurate computational models require substantial runtimes, meaning most models cannot be applied towards the optimisation of industrial processes.

In *Chapter 4* the material architecture was shown to have highly complex features with multiple length scales. Fibre diameters were in the range of 7 μm, with microscale characteristics that could affect the global material properties. However, modelling on this scale is computationally expensive due to the large number of required elements and degrees of freedom [100]. Homogenisation of the material properties is key to developing computationally efficient modelling strategies. Modelling scales can be sub-divided into three distinct categories, mesoscale, macroscale and semi-discrete [100]. These are initially defined below, before an evaluation in regard to process optimisation.

Mesoscale models

On the scale of the fibre tows, mesoscale models are typically built up in repeatable unit cells. This increases the computational expense, although well validated models can reduce the experimental material characterisation burden. However, the complex validation that goes into creating these models, as well as the significant computational cost, means that they are usually reserved for laboratory-scale experiments, such as bias extension [101], or as part of a multi-scale analysis.

Macroscale models

Macroscale models treat the material as a single homogenised continuum [101]. Characterising the material properties through experimental analysis and using these as input parameters, allows the modelling of the global mechanics. With fabric materials, membrane models are the most basic implementation [93, 94, 101]. Membrane models capture the in-plane shear behaviour but, by definition, do not include bending stiffness. With highly anisotropic bending properties, this can reduce the ability of the model to capture realistic wrinkling patterns [102].

To achieve this at the macroscale, some researchers choose to implement shell models [83]. However, without further adjustment of the constitutive relation, bending properties are calculated as a function of the in-plane elastic modulus. This means that as the stiffness along the fibres is large, bending stiffness is dramatically overestimated. To get around this, some choose to implement a lower elastic modulus when the fabric undergoes compression [103]. However, this coupling of in-plane and out-of-plane mechanics has been shown to not realistically capture wrinkling phenomena, particularly in NCFs [104].

Further work has followed that decouples the in-plane and out-of-plane mechanics. Here, through the use of shell-membrane models, decoupling of bending stiffness and in-plane stiffness can be achieved through mutually constrained nodes [96-99, 104]. This typically requires coupling or tying nodes, but it is also possible to manually assign nodes to two materials. By decoupling these properties, the experimental data for bending stiffness and in-plane shear stiffness can be used to capture the fabric behaviour. However, these models usually only support bending behaviour that initially is orthotropic. These are efficient, but cannot describe mesoscale effects such as slip or stitch rupture as these are functions of the global homogenisation. Shell-membrane models are widely implemented because they balance computational efficacy and accuracy of wrinkling prediction [96-99, 104].

Semi-discrete models

Semi-discrete models are between mesoscale and macroscale, they allow the material to be characterised at the macroscale, but include mesoscale effects such as the stitches, damage or slip. This can include using shell elements connected by bar or beam elements [105]. These models are not yet widely used for process optimisation due to the larger computational burden. Notable examples in the literature include a beam-membrane element formulation that allows the modelling of stitch effects [87] and a semi-discrete triangular shell element implementation [106].

Macroscale material modelling

In-plane shear behaviour, as described in C*hapter 4 – Figure 4.13,* is the predominant deformation mechanism of biaxial fabrics. This is due to the stiffness in this direction being orders of magnitude lower than the tensile stiffness along each of the fibre directions. Experimental data from either the picture frame or bias extension serves as input data [107]. This is typically in the form of shear stress as a function of shear angle, however calculation of the shear modulus can also be used as the input data [108].

In-plane tensile stiffness of the fabric, along each of the fibre lengths, is usually at least three orders of magnitude larger than the in-plane shear behaviour. In NCFs, in-plane elasticity is usually considered linear [21]. Some non-linearity can be expected due to the initially relaxed state of the fibre, however, this is not expected to be as severe as in woven materials, due to the impact of crimp in the woven fibre path.

Non-orthogonality of the fibre directions emerges as the material undergoes in-plane shear deformation. Initially, when the fibres are orthogonally aligned, the material properties along each of the fibre directions are trivial to calculate. However once shearing initiates non-orthogonality emerges through rotations about the pillar stitches. If we were to rely on the initial fibre coordinate system, as the material deformed, the fibre properties would overestimate the stiffness in each of the directions. To represent this complex behaviour, a non-orthogonal, co-rotating frame can be constructed to update a local coordinate system [98, 109]. Through this, the material properties along

each of the fibre directions can be updated with respect to the new non-orthogonal coordinate system.

The commercial software package, *Abaqus,* is often selected to model these materials. Different strategies in *Abaqus* exist to capture this non-orthogonality, typically by employing a non-linear material subroutine. Methods available include the use of a VUMAT, which allows high levels of customisation, however they do require the application of a transformation matrix [98]. The key model used in the literature is VFABRIC [94, 95]. This model automatically updates the incremental fabric stresses for the incremental fabric strains, whilst updating the material properties with respect to the local coordinate system. Material subroutines are written in the FORTRAN programming language and allow the input of experimental non-linear properties.

A final aspect to consider is that of shear-tension coupling. This is the material behaviour that governs the relationship between in-plane shear stiffness and the tensile stiffness of the fabric. This has been shown to more realistically represent the wrinkling morphology of woven materials [110, 111]. In woven materials, tension-shear coupling is determined to be a result of normal frictional forces at the warp and weft cross-over points [110]. In NCFs there is no cross-over of warp and weft yarns (*i.e.* non-crimp), therefore it is common to assume no shear-tension coupling.

5.2 IMPLEMENTED MATERIAL MODELLING METHOD

A dynamic explicit analysis was used in *Abaqus* for all FE models. This not only allows for complex contact interactions, but also facilitates integration with VFABRIC. To model the NCF efficiently, an elastic material with a zero Poisson's ratio in the direction of the fibres is assumed and tow slip that can often emerge at large shear is ignored. These assumptions enable a simplified homogenisation of the material properties. By definition, membrane models cannot capture the bending behaviour. Thus, a coupled membrane and shell element approach was pursued in this study, similar to [98]. Using a shell model alone would not allow the decoupling of the in-plane and out-of-plane behaviours. To achieve this in *Abaqus*, shell elements and membrane elements were defined whilst sharing superimposed nodes. This is distinct

from coupling or tying and allowed efficient computation of the bending response without affecting the constitutive in-plane behaviour [96-99, 112]. First, the membrane material model is discussed, followed by the shell material model.

As discussed previously, non-orthogonality emerges as the material shears; this necessitates updating the material properties with respect to the new fibre orientations. Towards that end, a VFABRIC non-linear material subroutine was chosen. VFABRIC calculates and updates the incremental fabric stresses for the given incremental fabric strains. The in-plane constitutive equation for the material, following the assumption about the Poisson's ratio, takes the form:

$$\begin{bmatrix} d\sigma_{11} \\ d\sigma_{22} \\ d\sigma_{12} \end{bmatrix} = \begin{bmatrix} E_1^T & 0 & 0 \\ 0 & E_2^T & 0 \\ 0 & 0 & G_{12} \end{bmatrix} \begin{bmatrix} d\varepsilon_{11} \\ d\varepsilon_{22} \\ d\gamma_{12} \end{bmatrix}, \tag{5.1}$$

where the directional subscripts 1 and 2 represent the fibre directions, which initially align with the material coordinate system direction x and y for the undeformed sheet. Here, $d\sigma$ is the in-plane incremental stresses, $d\varepsilon$, the in-plane incremental direct strains, $d\gamma$, incremental in-plane shear angle and G_{12}, the shear modulus. The Young's modulus applied to the membrane elements in the fibre direction was calculated from the fibre properties given in *Chapter 4 - Section 4.1*, after accounting for the fibre volume fraction. To allow the shell model to work in parallel with the in-plane membrane response, the total in-plane elastic modulus was decomposed according to *Equation 5.2*.

$$E^M = E^T - E^S . \tag{5.2}$$

Where the superscripts, *T, M* and S represent the total, membrane and shell quantities respectively. Using VFABRIC, the direct incremental stresses are calculated as shown

in *Equation 5.1*, but the shear stress, σ_{12}, is updated by making use of *Equation 4.7 and 4.8 (Chapter 4)* for the current shear strain, γ_{12}, without using incremental stresses and strains or the need to calculate an equivalent non-linear shear modulus, G_{12}. This model has been shown to successfully represent orthotropic fabric materials, such as woven glass fibre [94, 113].

The bending material model used S4 shell elements defined using the same nodes as the M3D4 elements in *Abaqus*. A single orthotropic lamina was used to define the material properties. The bending properties observed in the cantilever tests, in *Chapter 4,* are represented by an equivalent, average Young's modulus along the fibre directions. Specifically, the mean of the orientations where the long fibres were orthogonal to the fulcrum (see *Figure 4.12, cases 1-4*) was used. A mean bending stiffness, G, was calculated as 3.007×10^{-3} N m for a bending length of 164 mm - see *Equation 3*. Then, Bernoulli-Euler beam theory was deployed to estimate an equivalent in-plane Young's modulus. This was calculated by $E^S = \frac{12\,G}{t^3}$ and produced an equivalent modulus of 36.09 MPa with t = 1 mm for the NCF. The shell model also required transverse shear stiffness properties, which were set at 15.04 MPa, following *Abaqus'* documentation on shell section behaviour [114].

5.3 MATERIAL MODEL RESULTS AND VALIDATION

First, elementary tests were performed to validate the constitutive model and particularly that the shear stiffness was preserved following the combination of the shell and membrane elements.

Analysis of the sensitivity of the mesh size was also conducted, *Figure 5.1, left,* which revealed little in-plane sensitivity issues. *Figure 5.1, left,* also highlights the axial force *vs*. axial displacement results for the bias extension FE model against the experimental data. The model exhibited the expected behaviour, following the shear angle distribution as described in *Chapter 4, Figure 4.14.* This dictates the specimen should undergo no shear deformation in region A, pure shear deformation in region C,

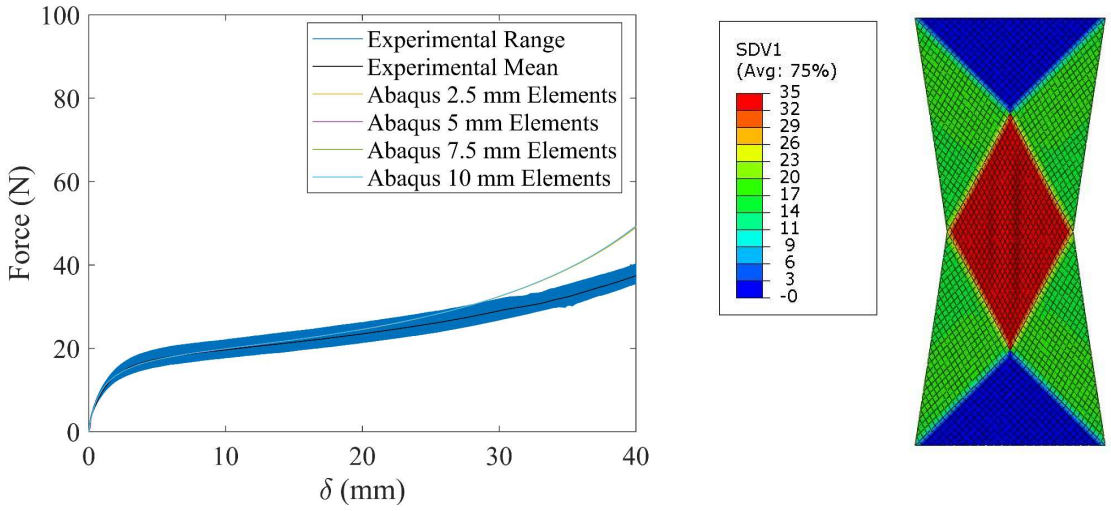

Figure 5.1: Left, virtual bias extension axial force vs. displacement results compared to the experimental behaviour for four different element sizes. Right, an example of the FE bias extension experiment for a 5 mm mesh edge size at 30 mm displacement.

and region B exhibits 50% of the shear deformation in comparison with region C, *Figure 5.1 (right)*.

In this instance, this resulted in an overestimation in force (when displacement is ~30 mm) similar to the behaviour observed in [115]. This may be due to edge effects and slip in the bias extension experiments which are exacerbated at high strain, as discussed in *Chapter 4, Section 4.4,* and also the homogenisation strategy employed. These edge effects, such as peripheral specimen stitch break down, are often exacerbated by the relatively small specimen sizes in bias extension testing, in comparison with industrial forming protocols.

A cantilever simulation was performed to validate the non-linear, in-plane shear stiffness and anisotropic, out-of-plane bending stiffness, similar to [98], which replicated the experimental procedure, *Chapter 4 – Section 4.3.* First, the 0°/90° orientation was assessed against the experiment, followed by the bias direction. As

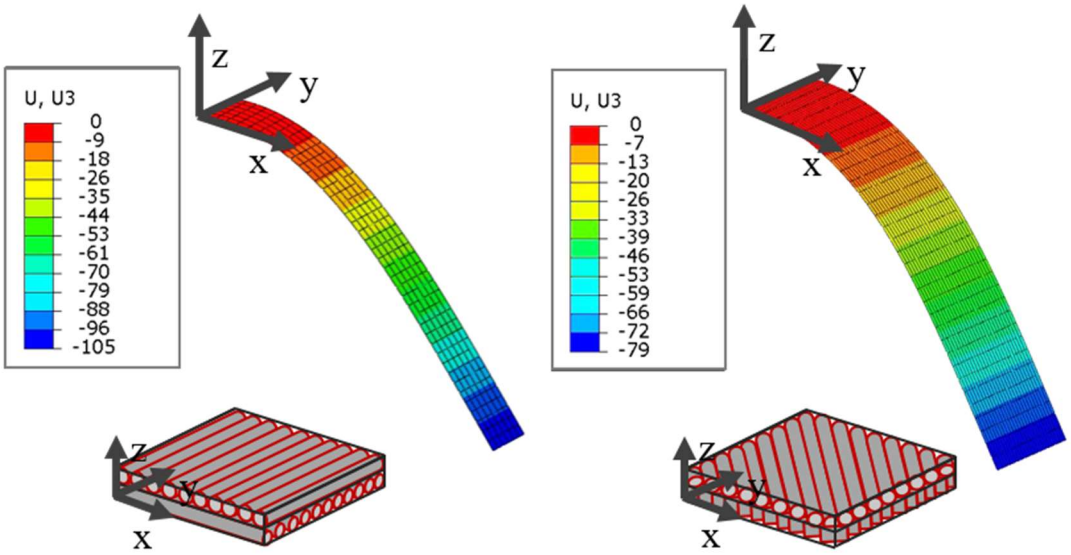

Figure 5.2: Virtual out-of-plane bending stiffness validation experiments based on the Shirley cantilever method. Left, indicates the FE results for the 0°/90° configuration and right indicates the FE results for the wider bias direction, with both plotted using the displacement in Z from the horizontal board (Figure 4.11).

bending is primarily governed by the bending stiffness in the fibre direction, performing a further check in the bias direction serves to validate the complex material behaviour. Following the work in [89], wider samples were used for the bias orientation simulation, in line with the experimental protocol outlined in *Chapter 4 – Section 4.3.*

For the 0°/90° orientation (*Figure 5.2, left)*, the bending angle was 41.5°, which matched the experimental measurement. Simulations undertaken in the bias direction (*Figure 5.2, right)* gave a 3.9% underestimate in bending angle, 39.9° for an 127 mm bending length. This underestimate is logical as the cantilever experiment neglects the contributions from slip, shear and fraying at the edges, which would be exacerbated in the bias orientation. Hence, the bias direction is not included as part of the test standard [84], however by conducting this further comparison, the model of bending stiffness can be robustly validated.

5.5 CHAPTER SUMMARY

The preceding chapter focused on the development of a macroscale FE material model for the veiled biaxial NCF, characterised in *Chapter 4.* Initial evaluation of the literature highlighted the applicability of macroscale strategies to process optimisation and modelling. Several key elements of a valid model were identified, namely: the high tensile stiffness of the fibres, comparatively low non-linear shear stiffness and a low anisotropic bending stiffness.

A shell-membrane element formulation was selected for the ability to tailor both the in-plane shear stiffness and out-of-plane bending stiffness, as well as computational efficiency. Some studies suggest almost a 50% increase in computation time when compared with a membrane model that, by definition, do not include bending stiffness [98]. This remains feasible for process optimisation and is not as costly as mesoscale modelling [101].

Non-linear shear stiffness was applied to the membrane elements through a VFABRIC material subroutine. Further, shell elements were defined with an effective elastic modulus calculated from the bending stiffness, before both elements were mutually constrained with shared nodes.

Virtual bias extension and Shirley cantilever experiments were performed to replicate the experimental protocols in *Chapter 4*. Both showed agreement with the experimental data, validating the hypoelastic constitutive relation and model implementation.

With a valid material model, virtual process models can be created, allowing for process optimisation that aims to improve the manufacture of composite parts. The model developed in this chapter, shows simple characterisation experiments can garner efficient and valid results for a highly complex NCF.

CHAPTER 6

DISTRIBUTED MAGNETIC CLAMPING: A NOVEL PREFORMING PROCESS

In this chapter, a method for facilitating the creation of challenging geometries by changing the boundary conditions in a flexible manner is proposed, termed *Distributed Magnetic Clamping* (DIMAC). This method allows for direct adjustment of local stress conditions and can be automated and optimised for a diverse range of part geometries. First, the background and context is introduced, before a purpose-built rig and the key methodologies are presented. Next, a proof of concept investigation validates the efficacy over a hemispherical geometry. A parametric study subsequently investigates discrete geometries and develops a metric of wrinkling severity. Results validate the novel distributed magnetic clamping process and test its efficacy.

6.1 INTRODUCTION

Dry fabric composites offer accelerated cycle times through efficient processing, out-of-autoclave manufacture, longer shelf life, and reduced dwell times. In comparison with prepregs, fabrics are also much easier to work with and manage on the shop floor. Non-crimp fabric (NCF) composites are now widely adopted across the aerospace and automotive sectors due to the aforementioned advantages and their reduced mass when compared with woven materials.

Manufacture and production processes, however, remain inflexible [116, 117], resulting in added barriers in developing open, multifunctional systems toward the goals of industry 4.0. Even within highly engineered settings, such as the aerospace sector, composite manufacture is predominantly guided by a practical understanding of forming processes. Academic research into NCF forming is often outpaced by pressures on industry. Leading manufacturers are continually developing new protocols and manufacturing techniques, frequently with proprietary intellectual property rights.

Research has also suffered from a lack of standardisation in what is a relatively new field. This adversely affects knowledge transfer and minimises the development of novel predictive modelling tools that can leverage diverse data sets. Herein, an adaptable manufacturing process is demonstrated, which allows tailored blank holder conditions using minimal hardware. The process employs magnetic clamps to provide scalable and flexible control of local mechanics through material tensioning.

Thus far, forming processes for NCFs have largely been borrowed from their crimped woven counterparts. These processes, including techniques such as diaphragm forming (DF), are beset with variability with little opportunity to accurately control boundary conditions (BCs) during preforming. They also add further computational cost to FEA models and are difficult to model, requiring understanding of the membrane and fabric pinning, exacerbating variation in the quality of resultant parts [98]. Increasing desire for parts of additional geometrical complexity indicates a need for bespoke forming operations. External to this, material development is also ongoing, meaning additional lead time is required to fully characterise any given material. NCFs are highly engineered, and hence many variations within this material category exist.

Approaches towards improving formability are available in the literature, both with *intrinsic* control (defined here as adjustments to the local in-plane stiffness through modifying the material itself [93-95, 109, 118]) and *extrinsic* controls (defined here as adjustments external to the material [119, 120]). While intrinsic controls such as resin overprinting and stitch removal offer promise, they remain difficult to implement on the shop floor. This is mainly due to the added processes that are inherent to any intrinsic method. By developing flexible extrinsic controls for material manipulation, pre-processing can be reduced. One robotic method is end-effector preform manipulation, which is fruitful at industrial scales [121], but requires expensive equipment and is relatively slow.

As discussed in *Chapter 4*, biaxial fabrics are the most common NCF (Fig. 1). Additions such as toughening veils [122] are now widely used in the aerospace sector as well as a plethora of other modifiable parameters via the stitch [123].

Asymmetric shear of some NCFs [115, 124, 125] adds complexity to the relation between the mechanics of the material and geometry, and has been shown to cause significant wrinkling [115, 126]. This asymmetry is typically the result of resistance to shear when one of the bias directions is aligned with a stitch direction. Asymmetric shear, however, can be reduced through choosing a fabric with balanced in-plane shear properties, such as biaxial NCFs which do not have a stitch path in the bias direction. A second method is through boundary control, which is a convenient and impactful process control parameter. Simple demonstrator geometries are typically used in forming studies to isolate desired effects. For example, a hemispherical tool, due to its implicit axisymmetry, facilitates evaluation of intraply shear. This is an active area of research, with the principle of differential shearing explored through spring-clamping [93, 109], overstitching [94], resin printing and pressure pads [65, 81, 112, 120]. These methods provide feasible routes to process control, but still carry barriers that prevent adoption in industry. These include high tensile forces and damage to the material, whilst requiring high accuracy in placement. Similarly, many methods require large mechanical assemblies and secondary processes, all of which increase production times.

Continuous blank holders, which prevent out-of-plane bending can be advantageous in reducing unwanted out-of-plane wrinkles, however, continuous blank holders can also prevent beneficial out-of-plane deformation, particularly in relation to positive curvature. By damping this bending mechanism, material can remain inside the part and increase wrinkle severity. Discontinuous variable clamping, that allows more out-of-plane deformation in discretised locations, combines several of the benefits of the aforementioned techniques and few of their challenges. Specifically, the use of distributed magnetic clamping is explored throughout this chapter. Distributed magnets allow for variable clamping forces at discrete locations, and can be applied to: the periphery or interior of the NCF sheet, against a supporting plate or against the tool itself. Magnetic consolidation of prepreg lamina has shown promise in reducing void content and demonstrates that permanent magnets could be easily utilised in production [127]. Large mechanical assemblies can be avoided and, thanks to the development of increasingly cheap suitable alloys, magnetic clamps are available in multiple sizes. The ease of application of magnetic clamps makes them appealing for studying boundary control, localised deformation, rate control, differential boundary forces, and multi-step protocols. This highlights highly flexible process control in comparison with conventional spring clamping methods.

Similar considerations apply to metrology tools. For instance, there is a large reliance in research on digital image correlation (DIC). However, scaling this into industrial settings is often impractical. Stereo vision systems require line-of-sight access to the operation, whilst also being expensive, labour intensive and difficult to implement on a production line. Other methods, such as photogrammetry, are operationally similar, yet offer more flexibility [119, 128]. Photogrammetry allows optimisation of image acquisition through its non-fixed set-up and therefore more data can be collected around particular features of concern. Readily available cameras permit reconstructed 3D models with high quality texture mapping, aiding analysis. We previously demonstrated the experimental capabilities of photogrammetry in [119, 129, 130], which has been corroborated in a comparative study with white light scanning [128]. Whilst photogrammetry does come at the detriment of some precision, the non-fixed set-up means that complex surfaces can be easily scanned in comparison with

DIC. A parallel study, outside of the main focus of this thesis, assessed drone based photogrammetry for preforming and highlighted sub-mm precision [131]. By focusing on flexible and scalable techniques, it is possible to merge data sets from both research and industry, including from both physical experiments and simulations. In turn, increased volume and diversity of data fuel the deployment of machine learning techniques to optimise manufacture.

6.2 METHODOLOGY

The distributed clamping test rig consists of two sub-assemblies that allows for the development of alternative tools in future tests, see *Figure 6.1*. The rig described here relates to hemisphere tooling, as this reduces effects due to geometry and isolates the anisotropic nature of the material, streamlining method verification whilst including double curvature. Through these trials the impact of distributed clamping on the forming behaviour was assessed. All tests were conducted with the *Tenax* [90/v/0/v/pb] biaxial NCF characterised in *Chapter 4.*

6.2.1 MATERIAL SAMPLE PREPARATION

Material sample preparation followed a rigorous process to reduce variability and induced pre-shear. This was achieved through masking the periphery of the cut lines with adhesive mounting tape and using a rotary cutter to cut square samples with side length of 400 mm. Prior to testing, each specimen was sparingly sprayed with a suspension of hydrated magnesium silicate (Talc, $Mg_3Si_4O_{10}[OH]_2$) in isopropanol (C_3H_8O), in a volumetric ratio of 1:4 – to facilitate image analysis. The alcohol evaporated leaving a fine white powder, which did not affect structural behaviour, contrary to conventional paint speckle methods. This approach, coupled with the presence of the veil, reduced reflections from carbon fibres whilst also providing trackable features for image analysis.

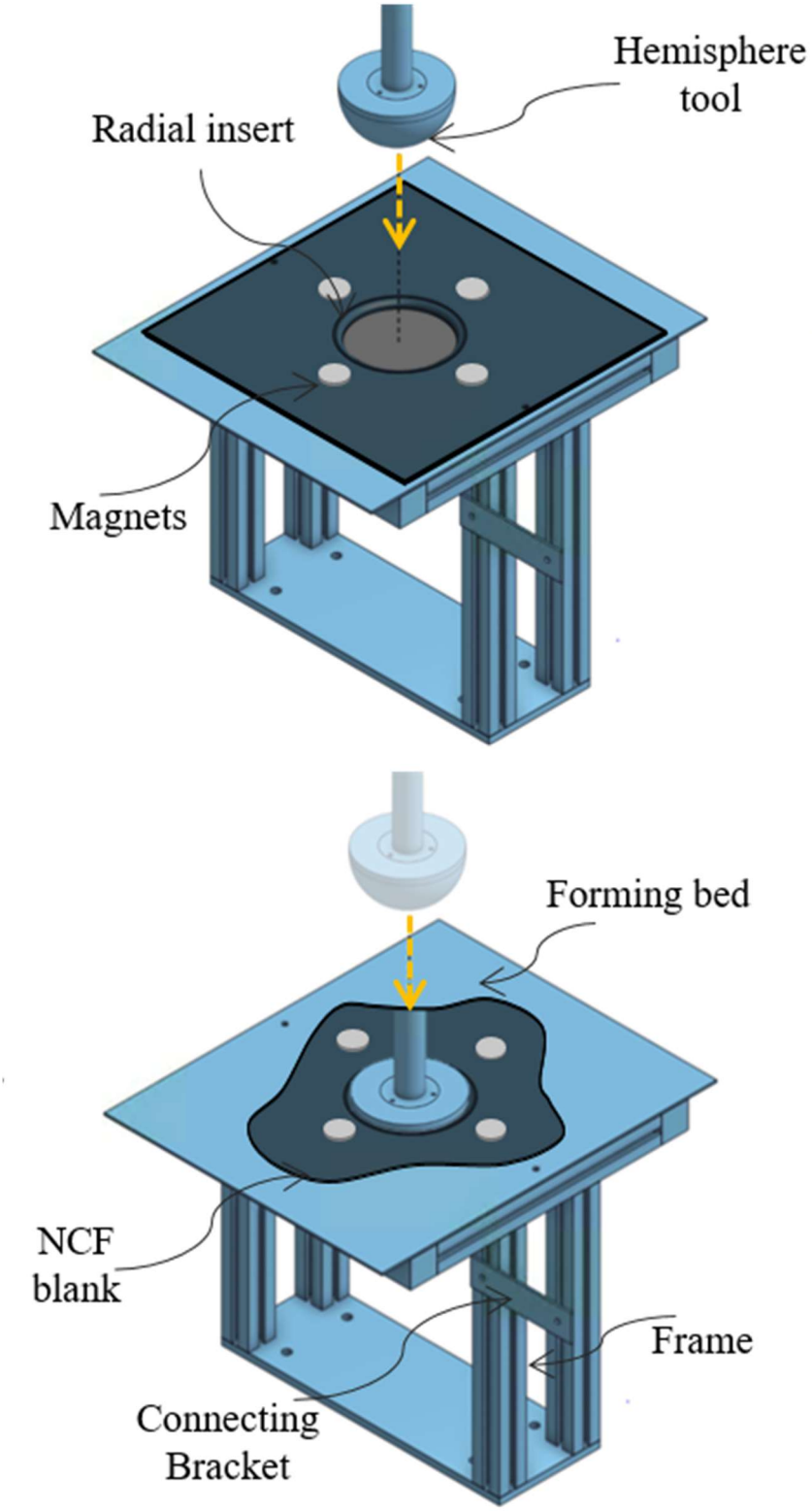

Figure 6.1: Top, distributed clamping process with hemispherical tooling in pre-deformed state and, bottom, representation after full stroke.

6.2.2 DISTRIBUTED MAGNETIC CLAMPING PROCESS

The distributed clamping test-rig developed for the hemisphere (radius = 60 mm) geometry is presented in *Figure 6.1.*

The rig was fixed to an Instron tensile test machine via mounting holes. A mild steel forming bed (400 x 500 x 3 mm) was attached to the supporting frame with a circular exclusion (radius = 61 mm). An insert with a 10 mm radius was then bonded to the internal exclusion. This part was vital for reducing stress concentrations that would lead to fibre or stitch damage, and for efficiently transferring tension between the magnets and tool. The part was 3D printed on a *Form 2* SLA printer from *FormLabs* and fitted with calibration markings to aid analysis. The hemispherical tool was machined with a smooth surface finish from aluminium. The tool included a 20 mm tangential extension from the equator to ensure no edge effect in forming, *Figure 6.2-6.3*.

The NCF blank was placed on top (veil side up) of the forming bed and clamped in place using magnets at the specified test locations. NCFs tested were orientated with the material x-direction aligned with the positioner X-direction. This was achieved

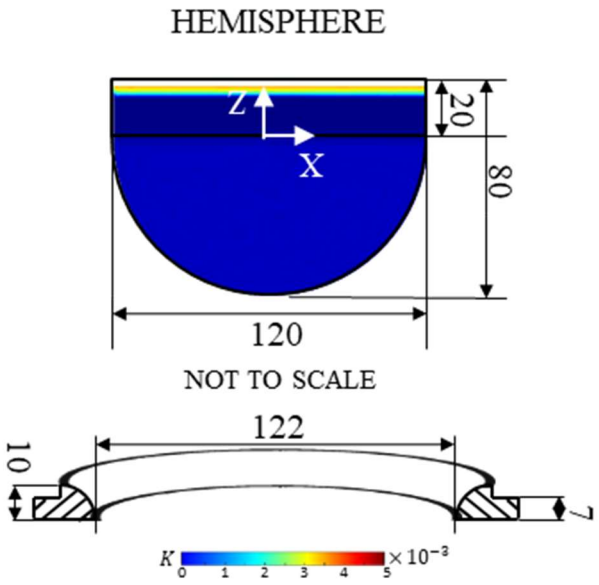

Figure 6.2: The hemisphere geometry used in this study, and radial insert schematic which is bonded to the forming bed.

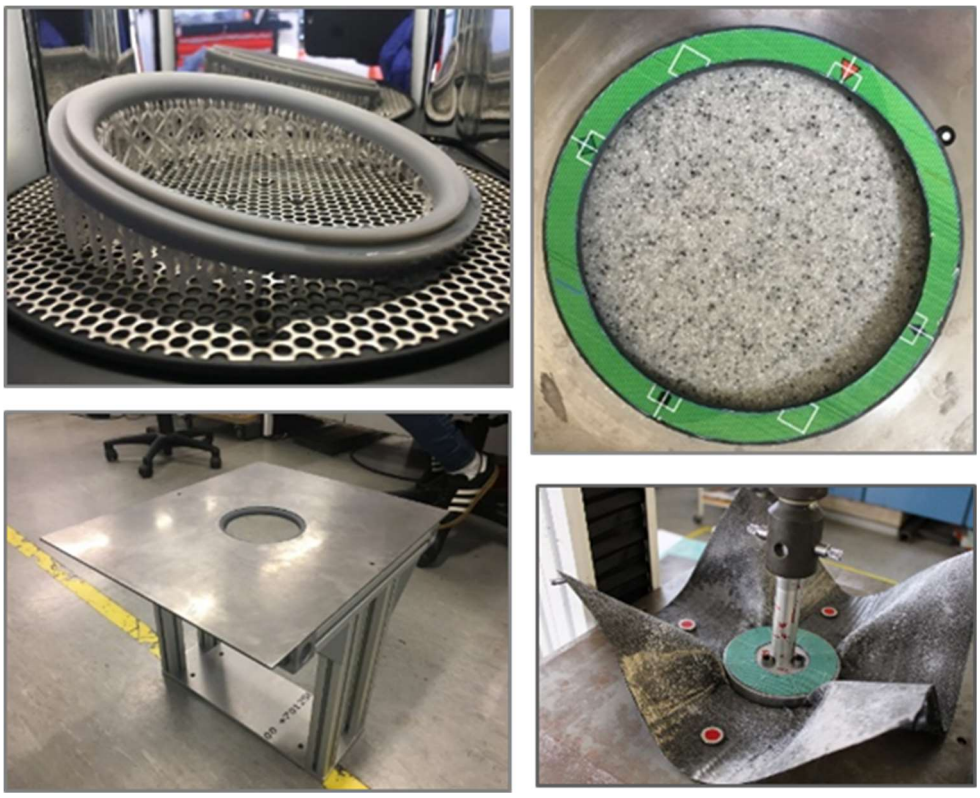

Figure 6.3: (Top-left) The hemisphere radial insert after curing showing recess bond line, (top-right) the reverse of the insert showing the calibration markings, (bottom-left) subsequent insertion to the forming bed, (bottom-right) example forming operation.

through the use of a magnet positioner with pre-defined discrete occlusions, *Figure 6.4*, laser-cut from 3 mm MDF. This was placed for positioning the magnets and removed before initiating the forming procedure. These occlusions corresponded to 16 angles at $22.5°$ increments and four radii at $r = 90, 120, 150$ and 180 mm, which were expressed in polar coordinates $[r, \theta]$. Given the material symmetry, four magnetic clamps were the minimum required to promote orthotropic in-plane shear deformation. This arrangement was defined with the coordinates $[r,\ \theta + i90°]$, where $i = 0, 1, 2, 3$. Four separate tests were performed, where $\theta = 0°, 22.5°, 45°, 67.5°$. The material architecture suggests the promotion of in-plane shear deformation for $\theta = 45°$. This works similarly for any geometry with four transverse planes of symmetry. The stitch architecture is shown in *Chapter 4, Figure 4.18*, both in natural, and deformed configurations. In the experiments, 20 mm diameter circular N42 neodymium magnets

with a thickness of 5 mm were used. The vertical and shear pull, as rated by the manufacturer, are 7.30 kg and 1.46 kg respectively when in contact with a mild steel surface, however as no test standard or specification is stated, calculating the compressive force from these values is not valid. Clamping force testing found a higher compressive force of 90 N. This was achieved by bonding a magnet to a tensile test machine platen. Subsequently, it was placed in contact with the steel forming bed and raised to record the peak reaction force. The selected magnets were chosen to be relatively high compressive force. Highlighted in the literature review, increasing blank clamping forces often yields preforms with less defects. Compared to conventional

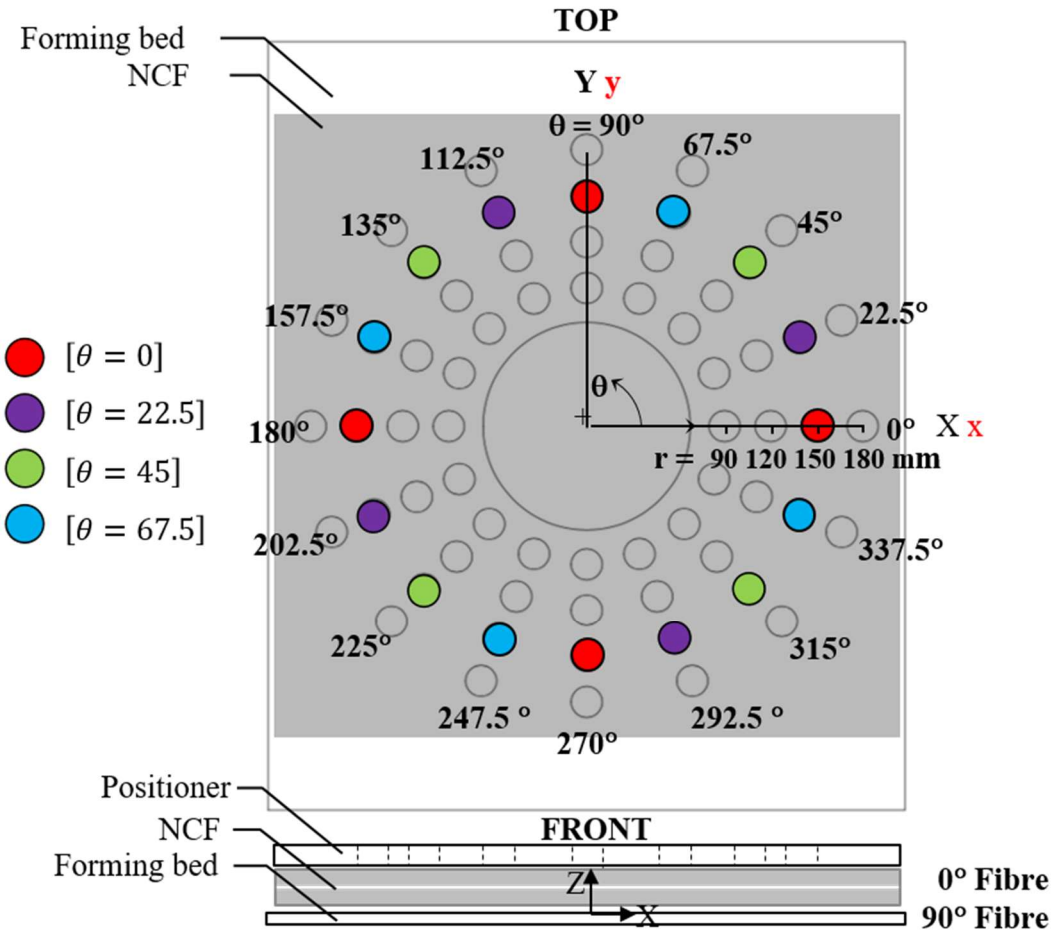

Figure 6.4: Magnet positioner and coordinate system where four experimental test configurations are defined by θ, which represent the four polar coordinates the magnetic clamps take: $[r, \theta]$, $[r, \theta + 90]$, $[r, \theta + 180,]$, $[r, \theta + 270]$.

spring clamps, when the in-plane tensile force exceeds the frictional force of the magnetic clamp, the magnets can slip over the surface of the fabric. In spring clamps this could cause stitch rupture or wrinkling. In this thesis, magnet location is selected as the variable parameter. In biaxial fabrics, shear deformation is energetically favourable. 20 mm magnets were chosen to discretise the inner clamping radius in a minimum of 16 locations, to offer the most flexibility. The advantages of magnetic clamping are summarised below.

- No large mechanical assembly required
- Available in a wide range of clamping forces
- Flexible size, shape, height, thermal compatibility
- Avoids fixed clamping, and permits slip
- Can be easily tailored to geometry
- Cheap and readily available
- Easily tracked in machine vision applications
- Clamping forces can be increased by simple stacking
- Can be automated with use of electromagnets or permanent switching magnets

6.2.3 METROLOGY: PHOTOGRAMMETRY

As was previously discussed, photogrammetry offers many operational benefits in a production environment in comparison with digital image correlation (DIC). Namely, ease of operation, accessibility, flexible data acquisition, speed of set-up, low cost, high functionality of point cloud post-processing, and feature optimised data acquisition, whilst approaching the precision offered by DIC. These benefits are of particular interest in agile manufacturing and the digital twinning of processes and environments, where monitoring and adapting production to improve quality and productivity are key drivers. Photogrammetry saw development through geoscience, allowing topographic data and surface visualisations through reconstruction of 2D images into 3D models, and works by calculating the spatial locations of shared features across numerous images. This dictates that photogrammetry is an image based modelling technique

where the output is a 3D model of the photographed surface or subject, usually expressed as a 3D point cloud.

With the development of further structure-from-motion (SfM) algorithms, photogrammetry is accessible to almost all skill levels and is available through a variety of software choices, including powerful open source options. Typically, the workflow consists of: image capture, model generation, post-processing, and analysis. By following the best practice, precision of up to 1/50 of a pixel can be achieved, with a theoretical measurement precision of approximately 0.05-0.1 mm for a 10 m sized object [132-134].

Guide for high precision analysis

1. **Image Capture**

   Photogrammetry analysis, like all data, is only as good as the acquisition. Taking high quality photographs and capturing the intended subject with care is paramount. Mistakes made at this stage cannot be remedied without repeating the process of image capture – in some cases this could be a destructive test method or dynamic manufacturing process. Digital single-lens reflex (DSLR) cameras are the preferred choice, and should include a full-frame sensor and high-definition prime lenses.

   Lighting is key, particularly considering how the lighting might change around the object or during testing or production, and should be uniform and stable. Gimbal stabilisation, tripods and fixtures can all be useful in ensuring stable images with less chance of blurriness or parallax errors. Image capture should ensure full coverage of the target surface, with consecutive images sharing at least 30% of the field of view.

   SfM works by recognising features, correlating and then tracking these features across an image set. For some materials, the topological features may be sufficient, such as the grain of wood. But to increase precision, surface patterns can be added in a similar way as is done for DIC. This can include speckle patterns, paint, marker pens or even stickers. Unlike DIC, photogrammetry is less effected by the distribution of feature sizes, so features do not have to be as regular across the target object.

2. **Model Generation**

Once high quality images have been captured, a SfM reconstruction software should be selected. Commercial software packages such as ReCap Photo (Autodesk), PhotoScan (Agisoft), and PhotoModeler (EOS Systems) are available and offer benefits such as cloud processing and technical support. However, to further develop and integrate model generation into automated workflows, open-source and free SfM packages exist such as Meshroom, Colmap and MicMac. For comparative software studies see references [135, 136].

Before importing the captured images into the chosen software, it is good practice to remove blurry images to reduce erroneous results from poor feature correlation. Similarly, images that are too similar can be removed as these will add further processing time, with little benefit. Open source image filtering software is widely available in a variety of languages such as python or environments such as Matlab, and can help in automatically removing blurry images.

3. **Post-processing and Analysis**

The software packages mention previously typically include some basic analysis tools, however, to develop bespoke analysis methodology, such as to assess surface height along a surface normal of discrete geometry, separate post-processing software is preferred. Open source packages such as CloudCompare and MeshLab are popular choices and allow fast and complex analysis when processing point clouds. Scripts in Matlab or other coding languages can also be used to process simple point cloud data.

In this thesis, the post-processing workflow subsequent to image capture, Figure 6.5 consists of: 1. Model Generation using Recap Photo (Autodesk); 2. Crop to the calibration perimeter markings around the area of interest; 3. Rescale the model by selecting the known reference distance on the calibration markings; 4. Crop away the calibration markings (at this stage all reference to physical space is lost, hence keeping the calibration marking on the first version is good practice; 5. Export the model as a point cloud; 6. Choose the post-processing software, in this thesis Matlab or CloudCompare were used and are indicated appropriately. Next align the point cloud

to the reference surface (typically a CAD file of the tooling); 7. Measure the distance between the reference surface and point cloud; 8. Finally, visualise the results as a contour map, or a distribution of surface height measurements.

6.2.4 TEST PROCEDURE

The test procedure was as follows: first the test rig was attached to an Instron 3369 tensile testing machine via the mounting plate and brackets. The mould tool was then fixed to a 1 kN load cell via a mounting bracket and pin. The NCF blank was placed centrally on the forming bed and orientated to the required position. Following this, the magnet positioner was employed to place the magnets at the test positions and removed once the magnets were all placed. The tool was first placed in contact with the NCF sheet and then lowered at a constant rate of 10 mm/min, moving a total of 61 mm along the negative Z direction, see *Figure 6.3*. On completion, both sides of the NCF were photographed using a *Canon EOS 2000D* SLR camera, ensuring full coverage of the specimens with 50-100 photos. Analysis through photogrammetry (*Autodesk's ReCap*) produced a 3D reconstruction of the surfaces in the form of point clouds. These were subsequently scaled with the use of calibration markings.

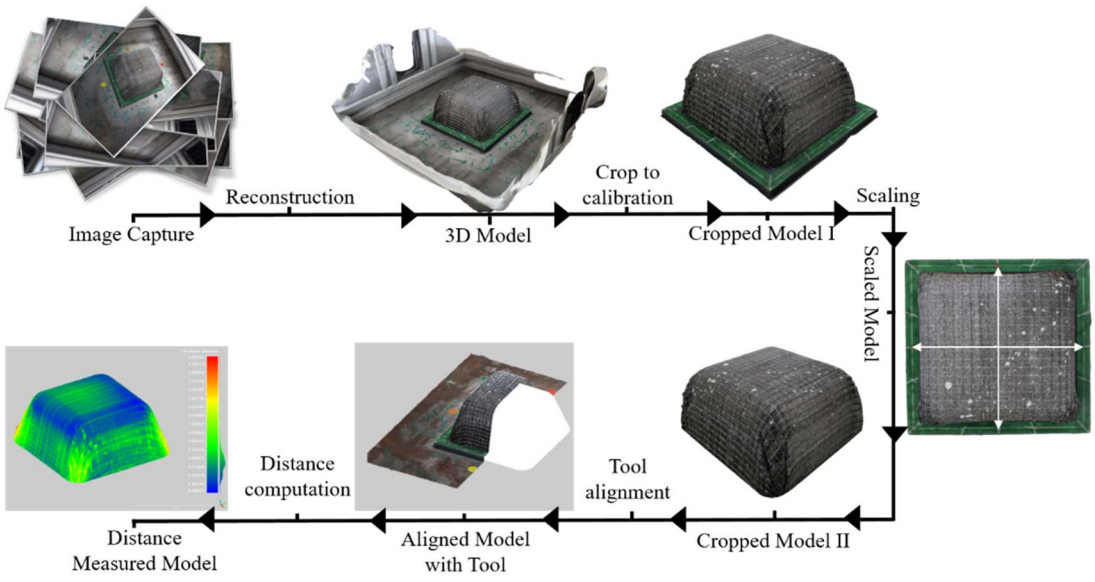

Figure 6.5: Workflow of the photogrammetry process

Accurate measurement of wrinkle size can be achieved through numerical analysis of the point cloud. The workflow is also amenable to automation with high quality scanned surfaces with texture mapping. As hemispheres can be described analytically, it is trivial to calculate the distance of the formed part from the origin of the hemisphere. This was measured at each coordinate in the point cloud, α. The distance between α and the tool surface, for every node was then calculated using the tool radius and original material thickness (1 mm) to give δ.

6.3 A PROOF OF CONCEPT STUDY

The discussion in *Chapter 3's* literature revealed an opportunity for novel boundary control using magnets. Two key arguments are repeated here. Lee *et al.* [9] experimentally studied the effect of blank holder force (BHF) on glass fibre NCFs produced through stamp forming and showed that through increasing the BHF, the asymmetry reduced. They also highlight that wrinkle sizes reduced significantly with increasing BHF. A further study conducted by Tanaka *et al.* [81] evaluated BHF through changing the boundary conditions (BCs) to optimise the same forming process over a hemisphere. The study looked at a biaxial 90/0 carbon fibre NCF with four different BCs tested. Although BHF magnitudes were not reported, it was concluded that by applying BHF, formability increased. More interestingly, shear deformation was facilitated by applying the BHF in only the ±45° directions and removing it in the 0/90° directions. Conversely, more wrinkling was seen when applying the BHF to the 0/90° directions and removing it in the ±45° directions, showing that there was significant variation in the shear deformation because of changing BCs.

In this section, the experimental distributed magnetic clamping method is investigated. Neodymium magnets are used to clamp the material onto a forming bed, allowing intraply and interply slip, whilst providing much greater flexibility in boundary control. Through exploiting magnetism, the need for large mechanical assemblies can be reduced, offering scope for further optimisation. This approach facilitates an innovative method of preforming, increasing productivity whilst reducing process complexity.

6.3.1 PROTOCOL

By increasing the distance of the magnet from the tool, a reduction in the tension of the material between the tool and magnet is achieved. Initial experiments replicate similar processes in the literature (discussed in *Chapter 3)*, validating the use of magnetic clamping in place of conventional clamping methods. Therefore, through clamping the ±45° and then the 0/90° directions, a comparison with the results from Tanaka *et al.* [81] is conducted. Secondly, by increasing the radius of the clamping positions, analysis is conducted on effectively reducing the BHF in specific directions. These studies utilise the hemispherical geometry outlined in *Section 6.2.*

All tests were carried out using the biaxial NCF outlined in *Chapter 4.* Analysis, through photogrammetry (*Autodesk's ReCap* software), produced a digital reconstruction of the surfaces. The output is a point cloud of the formed part, with colour added following *Section 6.2*. The test specimens are identified in *Table 6.1* where the different coordinates used are listed. Tests 1 and 2 replicate the effect of a continuous blank holder and the effect of changing the radius. This aims to represent an equivalent setup to conventional full blank holders. Test 3 clamps the 0° and 90° fibres at a radius of 90 mm, following the work conducted in [10]. Similarly, in Test 5 the ±45° directions are clamped. Tests 4 and 6 repeat the above strategy, but with double the radius, which aims to evaluate the effect of decreased tension on the material. All tests were conducted three times to evaluate repeatability and eliminate natural variability as a factor.

Table 6.1: Test specimens used in the proof of concept study.

Test	[r (mm), θ (°)]
1	[90, 0] + [90, 22.5] + [90, 45]+ [90, 67.5]
2	[180, 0] + [180, 22.5] + [180, 45]+ [180, 67.5]
3	[90, 0]
4	[180, 0]
5	[90, 45]
6	[180, 45]

6.3.2 RESULTS AND DISCUSSION

Initial experimental observation of the forming process highlighted material draw to the tool surface in all cases. Reconstruction, through photogrammetry, of the surfaces was also effective, producing point clouds and texture mapping.

Tests 1 and 2, seen in *Figure 6.6*, show no major out-of-plane wrinkling, as expected. In a) and c) textured scans are shown, while in b) and d) the deviation from the target shape is shown in terms of the radial distance from the sphere centre (δ). Repeated trials show the intraply shear mechanism of the material was successfully initiated. The results were similar to full blank holders, with magnets distributed every 22.5°, indicating sufficient tension was generated throughout the sample. The balanced BCs in this case, show that the material is permitted to shear and adhere to the hemispherical geometry. This is corroborated through the scans taken of the upper surface, *Figure 6.7*. In Test 2 it is apparent that the magnets at 0°, 90°, 180°, and 270° move towards the tool, along the orientations of the fibres. Further, magnets at the 45°, 135°, 225° and 315° appear to slip less and remain close to their original location. The

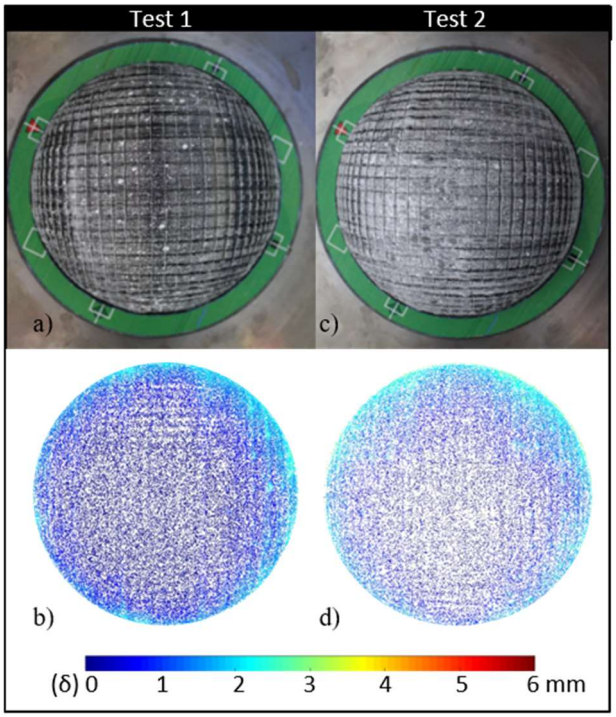

Figure 6.6: (a) 3D model of Test 1 (b) deviation from target for Test 1 (c) 3D model of Test 2 (d) deviation from target for Test 2.

Figure 6.7: Photogrammetry model of the top surface after preforming for Test 2. Magnets tagged with red stickers, the green circle shows the 180 mm radius of the initial positions, showing the material propensity to draw in from the 0° and 90° fibre directions. The yellow item on top of the mould is used for calibration.

remaining magnets show a balance of the two. This confirms that much larger intraply shear deformation occurs in the ±45° directions. This was further supported by Test 2, where very similar results were observed. Results showed little difference to Test 1, which may possibly be due to the improved formability with tension throughout the sample.

Tests 3-6 similarly revealed few surprises. These results are highlighted in *Figure 6.8*, where point clouds from the photogrammetry analysis are shown as well as the deviation from the target geometry. Test 3 and 4, where only the 0° and 90° fibres were held, showed wrinkling towards the ±45° direction of the hemisphere. This corroborates previous findings; these BCs facilitate more material draw-in from the 45° directions, reducing the ability of the material to shear, since the fibres are not permitted to move in the preferred manner. Controlling these orientations leads to a locking of the material, thus reducing intraply shear. *Figure 6.9* shows three repeats of Test 4, highlighting the repeatability of deformation, as such further repeats are not reported here.

In Tests 5 and 6 where the ±45° directions were clamped, corroboration of Tanaka *et al.* [81] was further verified. Deformation can therefore be influenced through local adjustment of the boundary conditions to reduce the defects. These results highlight the ability to control the intraply shear mechanism by applying distributed magnetic clamps to the NCF, with the axisymmetric part showing the effective control of the material draw in. A further objective of these experiments was to evaluate the process after reducing the tension on the material by increasing the radius of magnet positions. This could effectively reduce the applied forces as they are applied to a larger area.

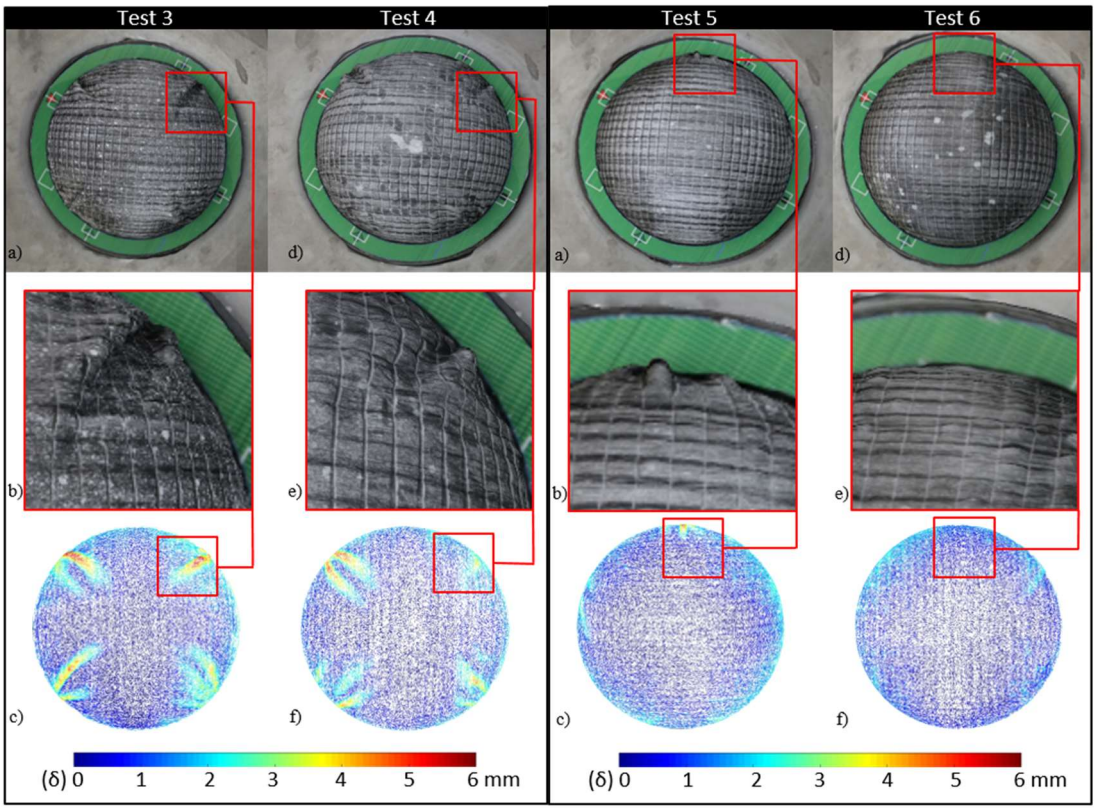

Figure 6.8: Left, (a) 3D model of Test 3, (b) magnified wrinkle from Test 3, (c) deviation from target shape for Test 3. (d), (e) and (f) contain the same for Test 4. Showing that wrinkling was seen in the ±45° directions as a result of clamping the 0° and 90° fibres. Doubling the radius and reducing tension, also shows a reduction in wrinkling magnitude. Right, (a) 3D model of Test 5, (b) magnified wrinkle from Test 5, (c) deviation from target shape for Test 5. (d), (e) and (f) contain the same for Test 6. Showing that wrinkling was seen in the 90° direction as a result of clamping the 45° direction. Doubling the radius and reducing tension, shows the wrinkle was removed.

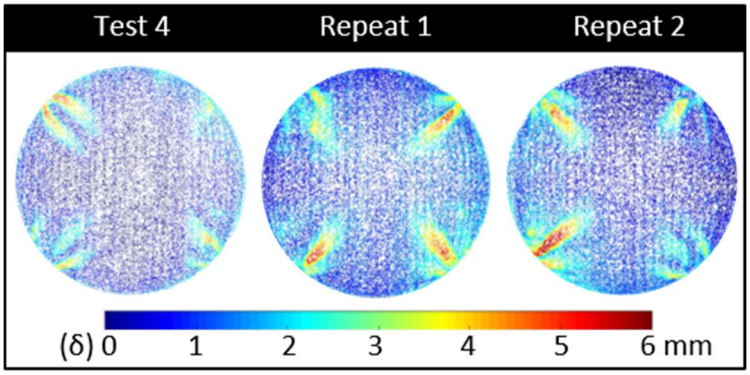

Figure 6.9: Left, deviation from target for Test 4 for three repetitions, showing wrinkle initiation in the same ±45° direction and the repeatability of the process. Right, available deformation mechanisms in biaxial NCFs, with mobility shear-dominated. Stitch points indicated in red, carbon tows in grey.

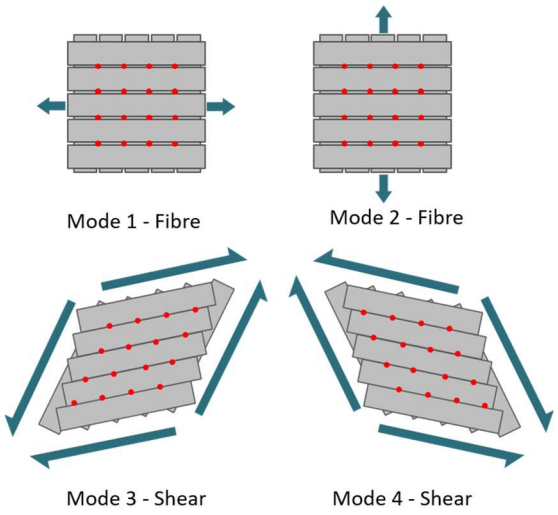

Figure 6.10: Available deformation mechanisms in biaxial NCFs, with mobility shear-dominated. Stitch points indicated in red, carbon tows in grey.

In Tests 4 and 6 the position radius was doubled. Tests 4 and 6 showed that by doubling the radius (180 mm), wrinkles reduced in magnitude. This again supports the view that optimising BCs can produce high quality, defect-free, double curvature parts.

Double curvature can only be formed through stretching or compressing material. Deformation mechanisms regarding NCFs are however very different to those of UD prepregs. Whilst similar mechanics are found, such as those discussed by Johnson *et al*. [137], in NCF there is no resin and instead two UD layers connected through stitching yarns. This creates new deformations modes, *Figure 6.10,* where Modes 1 and

2 are fibre modes in the respective fibre direction. These modes are not optimal forming mechanisms due to the carbon fibres themselves being inextensible. Modes 3 and 4 are much preferred, with these shear modes providing the dominant mechanism through rotations of the tows about the stitch points. Sometimes termed 'trellis shear', this translates into increased material mobility. In this work, it was shown that through utilising distributed clamping, different deformation modes were initiated. The hemisphere includes large negative curvatures, therefore by adding BCs to the material in the ±45° direction, the NCF was mobilised through shear, effectively pulling the excess material out of the target part. When only the 0/90° fibres were controlled, shear was not initiated, resulting in excess material being pulled into the target geometry causing out-of-plane wrinkling. By distributing BCs throughout the material, these modes could be tailored to specific geometries, allowing for much greater process control.

Through assessment of the hemispheres, it can be seen that wrinkles were mitigated in Tests 1, 2 and 6 with Test 6 showing no major wrinkling. In Test 6, reduced tension and only fixing the ±45° directions, with 4 magnetic clamps, produced results in line with those expected from a continuous blank holder. *Figure 6.11* compares the DIMAC process to a traditional production process. Here, a standard single diaphragm (SDF)

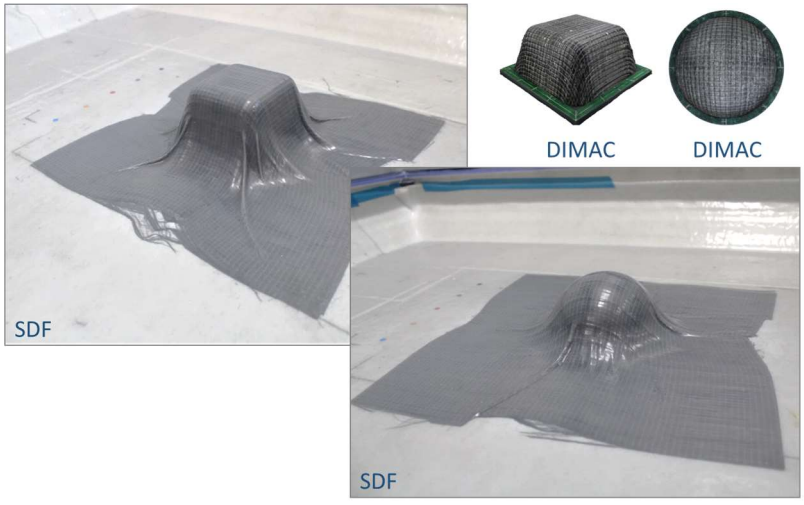

Figure 6.11: DIMAC comparison with single diaphragm forming for both a hemispherical and cubic geometry. The increase in defects and uncontrolled nature of deformation is markedly different.

experiment was conducted, over two geometries, to highlight the advantages of DIMAC. Here, SDF shows the variability and increased magnitude of wrinkling defects, compared with the DIMAC example. This offers new insight into the ability to actively control preforming deformation mechanisms through localised distributed clamping, and highlights the advantages of simple boundary control.

6.3.3 CONCLUDING REMARKS

The preceding proof of concept study evaluated distributed magnetic clamping as a method to locally adjust boundary conditions during hemispherical preforming. The study resulted in several insights that inform the development of the following chapters and provided a number of remarks:

- Distributed magnetic clamping was viable for local boundary condition adjustment and generating highly repeatable results.
- Results were consistent with previous studies highlighting in-plane shear modes as a key deformation mode of biaxial fabrics.
- The process outlined lays the foundations for powerful strategies which can optimise the placement of magnets on the periphery of the blank, or even against the tool itself.
- Analytically described geometries, such as the hemisphere, allow simple calculation of the deformation along the radial chords. However, a robust quantitative metric, for wrinkling severity, will be required for development to discretely described geometries.
- While the axisymmetric hemispherical tooling allowed validation and assessment of DIMAC, extension to more complex geometries is crucial for industrial relevance.
- Magnets were sufficient in clamping the fabric and initiating in-plane shear deformation, while still allowing some relative sliding over the forming bed and fabric.

6.4 DEVELOPING DIMAC FOR QUANTITATIVE ANALYSIS AND DISCRETE GEOMETRIES

It is hypothesised that through magnetic distributed clamping, NCF forming could be pursued for complex geometries while eliminating defects. Placing the clamps within the fabric allowed differential shearing through active boundary control, and a reduction in defects.

Further development to industrially relevant geometries with further complexity is crucial. However, a discrete geometrical description renders the analytical method for calculating δ obsolete. Therefore, a new method for metric calculation is developed that can utilise discrete descriptions of geometry. In composite forming, this geometry is the tooling, and thus a .stl file is most suitable due to their wide application.

This chapter first develops the methodology from the proof of concept study, before analysing the wrinkling metric for the cubic geometry. A wide range of boundary conditions are tested, before a presentation and wider discussion of the results for both the hemispherical and cubic geometries.

6.4.1 METHOD DEVELOPMENT FOR DISCRETE GEOMETRIES

Typical aerospace parts usually have many planar sections, particularly in panels, spars and wings, and these parts have further features such as radii and tapers. A geometry was therefore designed to replicate some of these complexities and, for the purposes of this thesis, is termed the *Cubic* geometry, see *Figure. 6.12*. This part was a natural follow-up to the hemisphere, with comparable tool dimensions and only positive Gaussian curvature. Further, it was not axisymmetric but had four transverse planes of symmetry. The overlaid Gaussian curvature in *Figure 6.12* highlights the key areas of double curvature, namely the radii and corners.

As the process was designed to be as modular and adaptable as practicable, only one other change to the forming process was necessary. That is the radial insert, which ensures no detrimental stress concentration where the material interface transitions from the forming bed, to the tool. This part was again fabricated from SLA 3D printing

and bonded to the central exclusion in a similar manner as is discussed in *Section 6.2*. When scaling this process to industrial settings, this part could simply be fabricated from machined or additively manufactured polymers or metals.

For the subsequent forming trials three clamping radii were selected for assessment: 120 mm, 150 mm and 180 mm. Clamp locations, as described in *Section 6.2*, are given with polar coordinates. Twelve tests were conducted with each experiment using 4 clamps and a further six using 8 clamps. These are defined according to *Table 6.2*.

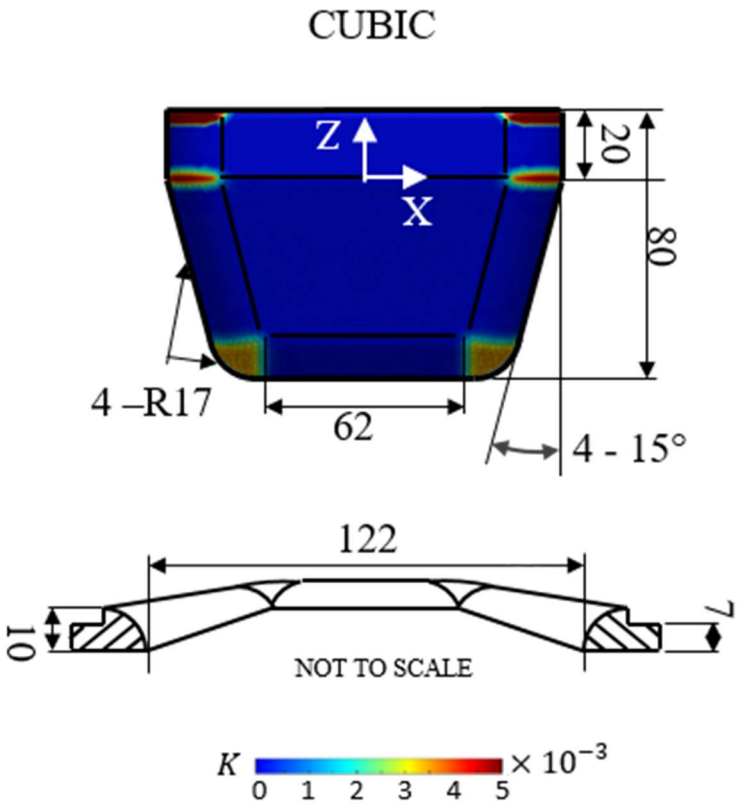

Figure 6.12: Cubic geometry used in this study. The colour map shows Gaussian curvature, K, overlaid. The bottom shows the radial insert.

Table 6.2: Experiments performed in Section 6.3.

Test	Radius (mm)	[r (mm), θ (°)]*
1	120	$[120, 0]$
2		$[120, 22.5]$
3		$[120, 45]$
4		$[120, 67.5]$
5		$[120, 0] + [120, 45]$
6		$[120, 22.5] + [120, 67.5]$
1	150	$[150, 0]$
2		$[150, 22.5]$
3		$[150, 45]$
4		$[150, 67.5]$
5		$[150, 0] + [150, 45]$
6		$[150, 22.5] + [150, 67.5]$
1	180	$[180, 0]$
2		$[180, 22.5]$
3		$[180, 45]$
4		$[180, 67.5]$
5		$[180, 0] + [180, 45]$
6		$[180, 22.5] + [180, 67.5]$

**Note: As described in Section 6.2, polar coordinates represent 4 orthogonal clamps defined by the first angle θ, where the '+' notation is assigned, 8 clamps were deployed with 4 orthogonal clamps per polar coordinate.*

6.4.2 METRIC FOR WRINKLING SEVERITY

After photogrammetry reconstruction, see *Figure. 6.13,* calculation of the metric, δ, was modified to deal with geometries that cannot be described analytically. Specifically, in those instances, a triangular mesh representing the tool surface, β, was used in *Matlab* to obtain normal vectors, $\vec{n}$ at each node. The tool mesh was constructed using a purpose built *Matlab* script with a 1 – 1.5 mm target mesh size. The intersection of the normal, $\vec{n}$, with the scanned or simulated final shape, α, was used to calculate δ through a triangle-ray intersection algorithm [138, 139]. The intersection algorithm, developed for ray tracing in computer graphics, solves:

$$\begin{bmatrix} -d_x & v1_x - v0_x & v2_x - v0_x \\ -d_y & v1_y - v0_y & v2_y - v0_y \\ -d_z & v1_z - v0_z & v2_z - v0_z \end{bmatrix} \cdot \begin{bmatrix} t \\ u \\ v \end{bmatrix} = \begin{bmatrix} o_x - v0_x \\ o_y - v0_y \\ o_z - v0_z \end{bmatrix}$$

for,

$$\begin{bmatrix} t \\ u \\ v \end{bmatrix}.$$

Barycentric coordinates u and v, are given at point T, so that $T(u, v)$. The ray is $R(t)$ and $t/_{|d|}$ is the distance between the intersection point and the ray's origin, o. The ray and triangle thus intersect if $u \geq 0$, $v \geq 0$ and $u + v \leq 1$.

Through this algorithm, the severity of wrinkling can be evaluated for any input tooling and any scanned point cloud. In this work, photogrammetry was used to capture the 3D point cloud as described previously. However, in practice, techniques such as X-ray CT, infrared imaging, white light or laser scanning could be used to reconstruct the point cloud for subsequent analysis. This technique does not capture the complexity of wrinkles that included multiple folds, but it produced a simple estimate of defects. We further leveraged the metric, δ, by calculating δ_{max} and δ_{75th} for a given instance of the test, allowing for further analysis of the distribution of results. Here, δ_{75th} is defined as the 75th percentile of δ. Similarly δ_{max} is the maximum of δ.

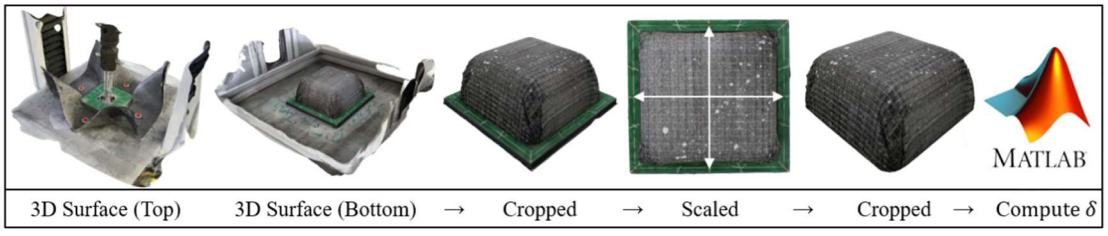

Figure 6.13. Experimental photogrammetry and post-processing workflow. (Left to right) Raw images are converted into a 3D surface, cropped and aligned to a plane, scaled via calibration markings to the known distance (132 mm -white arrows), further processed to remove the radial insert and calibration markings. Finally, conversion to .ply file for computation of δ in Matlab, from the intersection of the tool surface normal, $\vec{n}$, and triangulated formed material surface, α.

6.4.3 RESULTS AND DISCUSSION

Distributions of δ, *Figure 6.14*, revealed that some points were below the original material thickness of 1 mm. This is likely due to intraply deformation and small gaps between tows as described in *Chapter 4*. This means that values of $\delta \geq 1$ mm represent material thickening, via shear deformation, and defects such as wrinkles and folds. From *Figure 6.15*, it is seen that all of the experiments where $\theta = 0°$ result in the lowest mean value of δ (Test 1 where r = 120/150/190 mm). This is due to the increased tension as a result of fibre mode deformation, resulting in greater material to tool conformity. However, to allow subsequent comparison with FE data, which by definition in *Chapter 5* is homogenised as a single 1 mm thick continuum, δ values had a threshold applied to satisfy $\delta \geq 1$ mm. The plots pre- and post- threshold confirm there is no change in δ_{max}, as expected, and show δ_{75th} is adjusted with a comparative minimum value of δ.

The point clouds for all cubic experiments are presented in *Figure. 6.16*. Here, δ is applied to the colour map for visualisation. These visual representations of the forming process allow simple assessment of the photogrammetry scaling and alignment procedure. In Test 4 (r = 120) some points were below the threshold value and were therefore cut. These show as white gaps in the cloud, which were minimally present. The results show no significant difference in changing the clamp radii and still reveal shear mode deformation, where $\theta = 45°$, as the best result. Analysis of the 8 clamp examples also show that the major clamping angles were more beneficial than

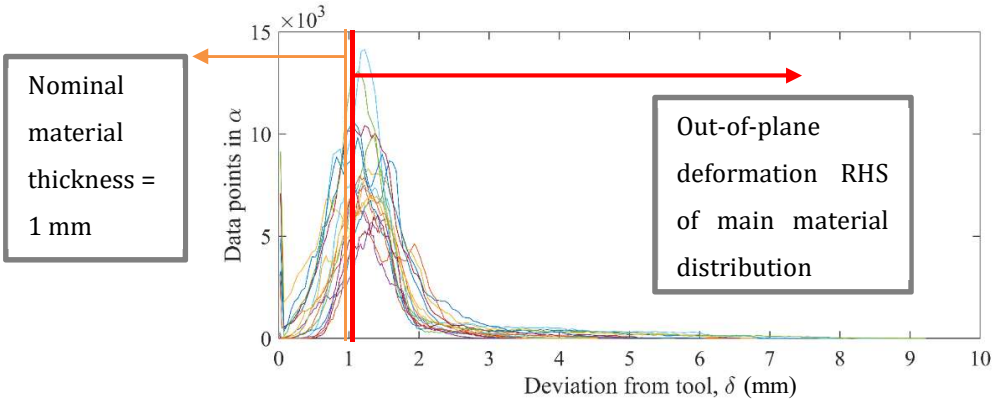

Figure 6.14: Distributions of δ for all cubic experiments revealing the coherence of the 18 histograms and regions of defects.

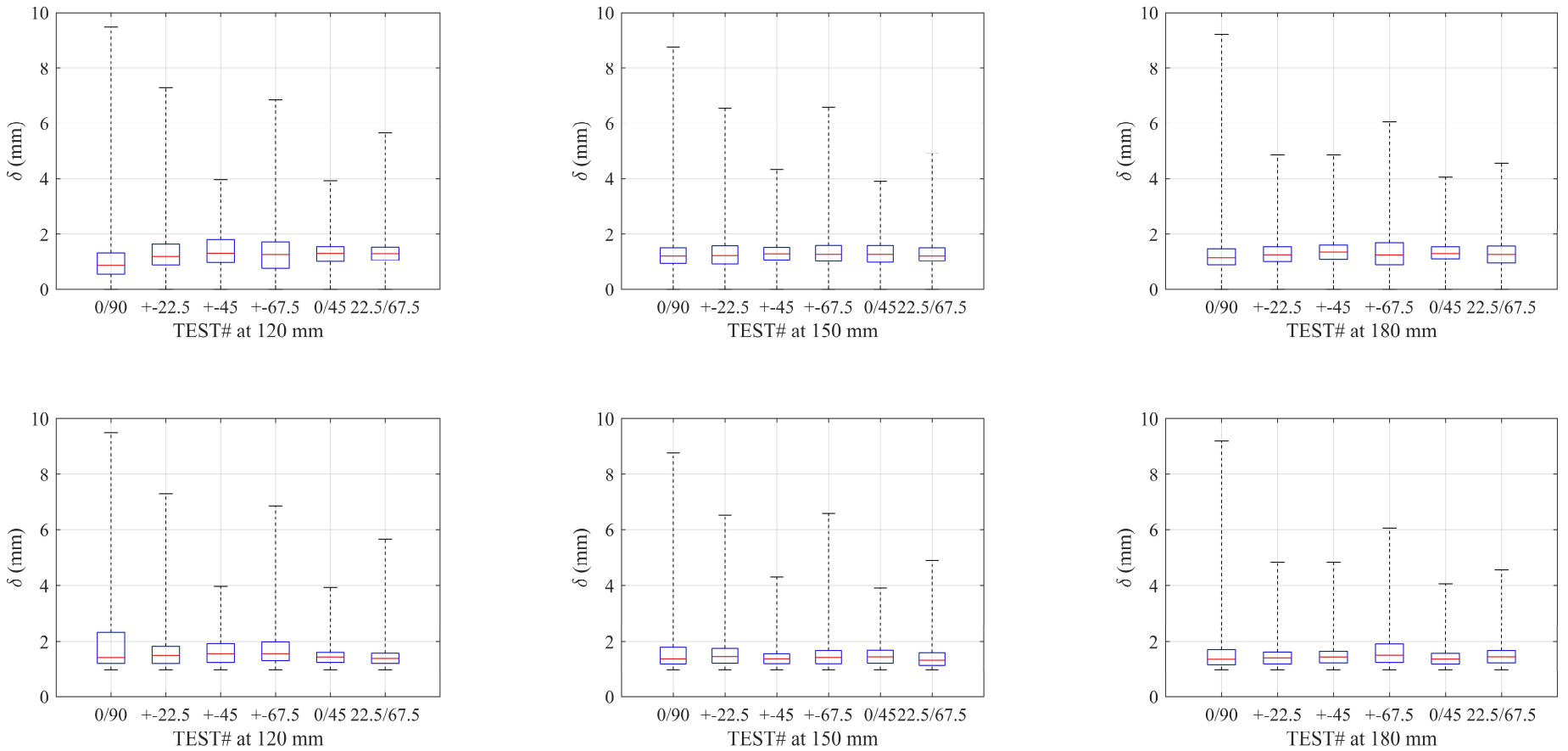

Figure 6.15: Top, left-right show δ boxplots for three indicated radii before applying the threshold. Bottom, left-right show the same distributions after applying $\delta = \ \delta \geq 1\ mm$.

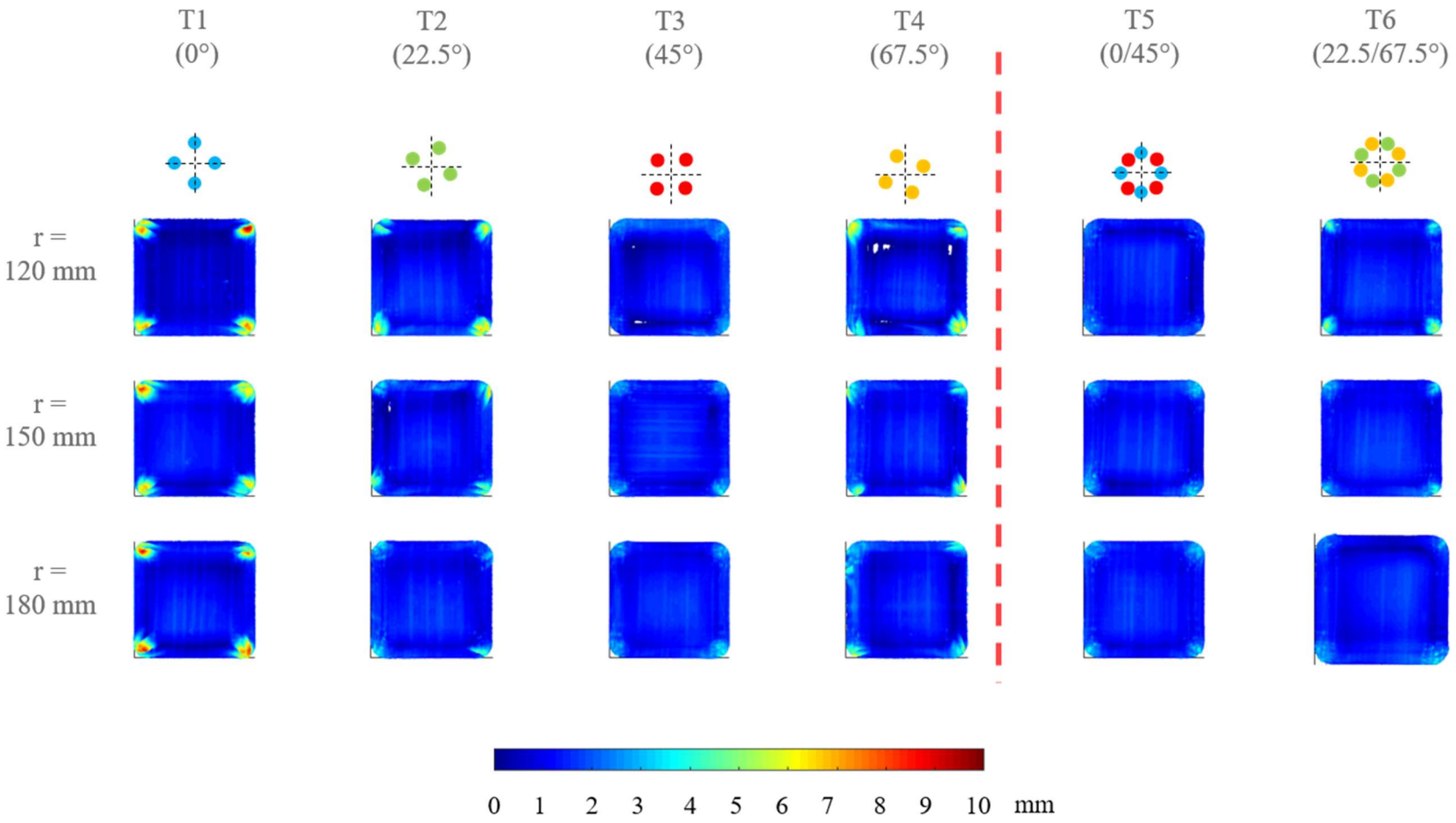

Figure 6.16: Resulting point clouds with appended δ values for each of the cubic results.

the minor angles. Major angles refers to Test 5, and minor angles to Test 6. Test 2 and Test 5 confirm that the material exhibits a balanced shear stiffness , with δ_{max} values showing good correlation.

To allow comparison between the cubic and hemisphere geometries, the hemispherical examples from the proof of concept study were tested again with the new protocols. Following the deductions about the clamping radii, only experiments at a clamping radius of 150 mm are discussed in more detail, for brevity. For the hemisphere geometry (*Figure. 6.17* and *Table 6.3*), large wrinkles were mitigated when $\theta = 45°$. In the fibre mode example (when $\theta = 0°$) large macroscale wrinkles were present in low tensile regions. As discussed in *Section 6.3*, low-tensile regions do not allow shear deformation as the material is drawn in, causing the initiation of compression-folding which prevents conformity. In the mixed-mode experiments, when $\theta = 22.5°$ or $\theta = 67.5°$, twist of the fibre tows was observed. Wrinkles however, were again largely mitigated in comparison with the 0° case, although both showed evidence of tow slip.

In the case of the cubic geometry, *Figure. 6.18* and *Table 6.3*, when $\theta = 45°$, forming over the complex geometry highlighted the plausibility of the forming technique, with wrinkles above 2 mm reserved to the bottom of the formed part. The 75th percentile of deformation shows the majority still conformed. When examining the material qualitatively, wrinkles were reduced over the main section of the geometry, with a wrinkle-free region over 55 mm of stroke depth (St). Fibre tow bunching was also present, *Figure. 6.18b*, due to the large strain required to form the corner. This is likely due to the tricot stitch. When $\theta = 0°$ wrinkles were largely symmetric over each corner. This represents two areas of material which fold back in on themselves as the shear mode is not activated. When $\theta = 22.5°$or $\theta = 67.5°$, twist was again observed, with less impact on the fibre direction. This is possibly due to a decoupling or reduced dominance of in-plane tension, with the contact point from each magnet not coincident, as it is in the hemisphere (pole). Wrinkling differs, with major macroscale folds now asymmetric on each corner. Again, both mixed-mode experiments showed more evidence of fibre slip, as is to be expected from tension-shear coupling (see magnified images in *Figure 6.18).*

Table 6.3: Experimental results. Note: pre-deformed material thickness is 1 mm.

Magnet Angle, θ (°)	Hemisphere, δ (mm)		Cubic, δ (mm)	
-	δ_{75th}	δ_{max}	δ_{75th}	δ_{max}
0	*1.8*	*6.0*	*1.8*	*9.0*
22.5	1.3	2.9	1.7	6.6
45	1.3	2.4	1.6	4.3
67.5	1.5	3.1	1.8	6.5

It is evident from the experiments that distributed magnetic clamping had a strong effect on forming for both hemisphere and cubic geometries. In-plane radial tension was generated between magnetic clamps and points of contact on the tool. Tangential forces around each magnet were also present, however these seemed to be less dominant as they induce bending, which relieves the corresponding stresses. Magnetic clamping was also shown to control the material draw-in when activating the shear mode, ($\theta = 45°$), for both the hemisphere and the more complex cubic geometry. Discontinuous blank clamping, unlike continuous blank holder clamping [115], allowed the material to deform with out-of-plane bending (*Figure. 6.17-6.18*), hence reducing the available energy that could induce mesoscale wrinkling. This may indicate an important method of facilitating optimum shear in a similar way to manual folding and tension shearing in hand lay-up [140]. FEA models that incorporate bending behaviour could therefore be critical to fully unlock the forming potential of NCFs in this manner.

As the experiment progressed, the horizontal offset between tool and the radial insert decreased. During the final stages, this resulted in compaction of the fabric between tool and radial insert. This effectively clamped the material, promoting increased tensile forces that draw the material closer to the tool surface, allowing small wrinkles to re-orientate. *Figure. 6.17c* and *6.18c* show that in the mixed-mode experiments, $\theta = 22.5°$, fibres slip to accommodate the differential force induced by the unbalanced boundary conditions. Whilst this could lead to defects, particularly post-cure, this does highlight that magnets could be utilised to induce steered fibre tows and non-standard deformation.

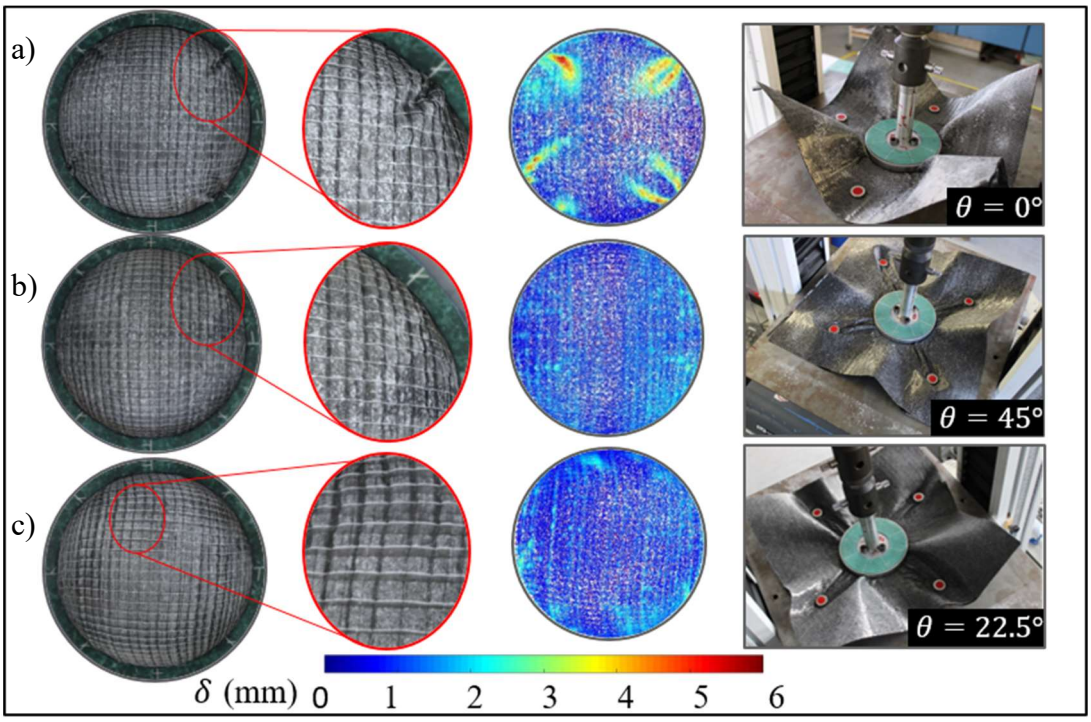

Figure. 6.17: Hemisphere experimental results for three representative clamping configurations: a) fibre mode with magnets at 0°, b) shear mode magnets at 45°, c) mixed-mode 22.5° showing the 's' shaped twist steered fibres induced through tension shear coupling and slip. Oval magnifications show contrast enhanced inspection of major deformation, including evidence of slip. Colour maps show the distance of the material from the tool, δ. The top surface highlights the promotion of out-of-plane bending as an important forming behaviour.

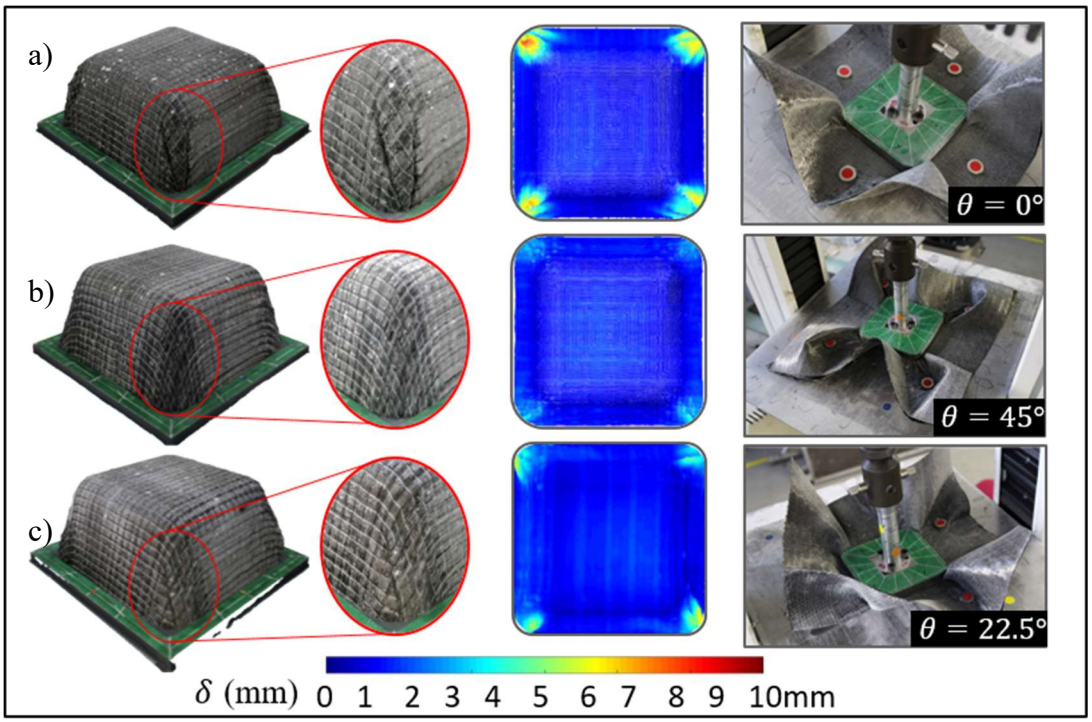

Figure. 6.18: Cubic experimental results for three representative clamping configurations: a) fibre mode with magnets at 0°, b) shear mode magnets at 45°, c) mixed-mode 22.5° showing the twist induced through tension shear coupling and slip. Oval magnifications show contrast enhanced inspection of major deformations. Colour maps show the distance of the material from the tool, δ. The top surface highlights the promotion of out-of-plane bending as an important forming behaviour.

6.5 DISTRIBUTED MAGNETIC CLAMPING – CONCLUDING REMARKS

A novel approach to apply BCs and control deformation in preform production of NCFs has been demonstrated. The use of magnetic clamps has shown results similar with those produced from continuous blank holders, and offered further understanding of the mechanics of forming while providing additional manufacturing flexibility. These results offer a novel approach to forming that is accessible to small scale part production and scalable to industrial applications.

Distributed magnetic clamping successfully induced in-plane tension to alter the deformation mechanics in single ply forming scenario. Promotion of out-of-plane bending in the material, because of discontinuous blank clamping, enabled a reduction in defects when the shear mode was activated. A complex cubic geometry with industrial applicability was successfully shown through experiment to have good material conformity.

DIMAC also highlighted the benefits of extrinsic process control. By facilitating quick adjustment of local boundary conditions, a large data set, that uses minimal hardware, was developed. This not only fuels the diversity of data, but also allows the deformation mechanics to be efficiently probed.

The non-fixed non-stereo photogrammetry technique was successful at capturing the surface morphology of the material and allows further flexibility and evaluation of otherwise inaccessible regions and could be used in industrial settings.

The metric for wrinkling severity, δ,was developed and validated for discrete geometries. Through this metric, a wide range of preforming operations can be assessed which use complex tooling. Further, the metric was not specific to photogrammetry data, and can therefore be ubiquitously used in conjunction with techniques such as XRCT, infrared imaging, white light scanning and DIC.

DIMAC offers more flexible, scalable and industrially relevant processing opportunities for manufacturers. The method would also compliment many existing processes and facilitates integration and extension of data sets.

CHAPTER 7

GAUSSIAN PROCESS MODELLING AND BAYESIAN OPTIMISATION

In this chapter, a brief background to Bayesian optimisation first introduces the context of the method before considering the applicability to DIMAC. After, an optimisation problem and methodology are set out. An FE virtual model, representative of the experimental process, was next developed and validated to serve as the evaluator. Bayesian optimisation and Gaussian process modelling were then applied to guide the optimisation of magnet position. Results highlight the efficacy of these predictive modelling tools and the benefits in designing a system that can efficiently adapt boundary conditions.

7.1 INTRODUCTION

Through simple adjustment of the local boundary conditions, DIMAC demonstrated the benefits of extrinsic process control. Parametric studies presented in *Chapter 6,* further revealed DIMAC as an ideal candidate in generating diverse preform data sets. However, predicting the deformation of dry biaxial fabrics typically requires complex three-dimensional finite element (FE) models. These models must not only account for non-linear shear behaviour and out-of-plane stress, but also complicated contact interactions. Industrial production of NCFs takes place at all scales, from small secondary components, to expansive primary structures which require a large number of elements. This further adds to the computational burden when developing virtual process models and renders global optimisation methods intractable.

Machine learning has already been shown to be powerful in the context of composite materials. Chen *et al.* [93, 94, 109] recently demonstrated that genetic algorithms and artificial neural networks (ANNs) can successfully optimise component in-plane properties for a chosen geometry. Optimisation in this manner is often expensive to evaluate for new geometries, with large numbers of objective function evaluations [141]. Hence, others have explored alternative techniques which reduce computational requirements, such as Bayesian optimisation with Gaussian process modelling. Here, a surrogate of the FE model guides the optimisation and reduces the number of FE evaluations [141], alternative to expensive optimisation of the objective function itself.

Bayesian optimisation can become particularly powerful when coupled with convolutional neural networks (CNNs) [96, 99, 112], or for hyperparameter tuning. Zimmerling *et al.* [112] highlight that significant computational savings can be made in feature and process level optimisation through optimised offline CNNs. These are, however, still limited by the size of training data sets, with features sufficiently separated [96]. Future approaches utilising feature and process level optimisation in a single package consequently seem likely. Bayesian optimisation [142-145], when coupled with Gaussian process modelling [146], allows efficient optimisation that balances exploration and exploitation of the search space whilst outperforming

stochastic gradient based methods in uncertainty quantification.

7.2 BAYESIAN OPTIMISATION METHODOLOGY

In a general Bayesian optimisation framework, the aim is to minimise a so-called black-box function, denoted by $f(\theta)$, of varying inputs θ. A black-box function refers to the situation in which the process for obtaining the function output at a given input is unknown or difficult to model. In this thesis $f(\theta)$ denotes the material conformity at magnet angle θ, in the absence of any noise. Bayesian optimisation is able to minimise such functions by maintaining a statistical model representing our prior belief about the function based on data, $\delta_1, \dots, \delta_n$, from past experiments, corresponding to noisy versions of the function $f(\theta)$ at tested inputs $\theta_1, \dots, \theta_n$. An extensive background to Bayesian optimisation can also be found in [145] and [147]. The statistical model is updated sequentially with the acquisition of new data, and the next test input is proposed based on improved knowledge of the minimiser, *Figure 7.1*. The model used in this paper is a Gaussian process model, described in more detail later.

In the specific case of DIMAC, the inputs are the parameters of the experiment, such as the position of the magnets and the clamping force, and the output is the deviation from the target shape, δ. The objective is therefore to choose the inputs that give the least defects.

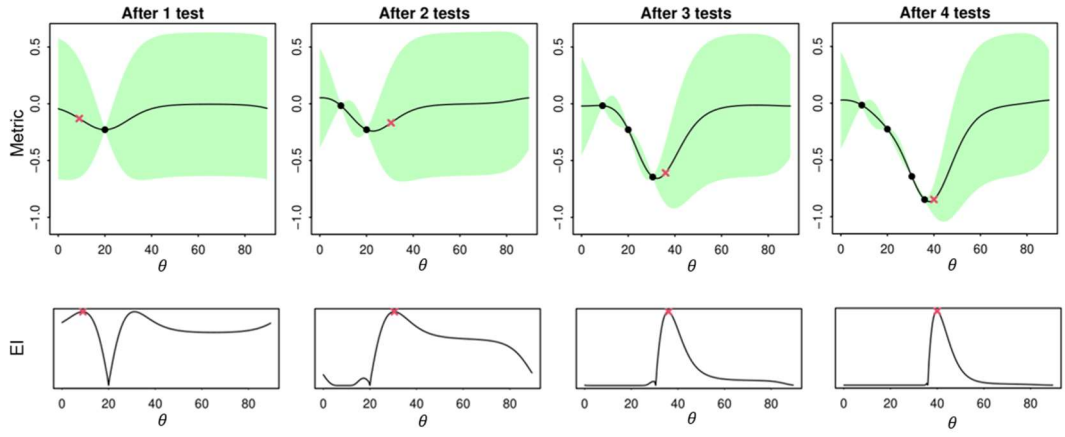

Figure. 7.1. An example periodic Gaussian process model (top) and expected improvement (bottom). The mean of the distribution is represented by the black line and uncertainty by the green area, which denotes the 95% confidence interval for the value of the function.

The data observed also provides information about the overall shape of the function, which reduces the uncertainty in the model, but at the same time, as the simulations are expensive, resources should be dedicated to locating the minimum accurately. In practice, this method is not bespoke to only computational evaluation of the objective function, but could also be used with physical experiments in a parametric trial. The learning of the function is known as *exploration* and the locating of the minimum as *exploitation*. A decision about which input to test next is made in a way that balances exploration and exploitation. At the early stage, when not enough observations are available, exploration is more desirable. The statistical model carries some uncertainty about the value of the function at untested inputs. As more data is obtained, the uncertainty is reduced, leaving the focus to become exploitation.

7.2.2 STATISTICAL MODELLING

In regard to DIMAC, we can dictate four magnets are placed at angles, θ, θ + 90°, θ + 180°, and θ + 270°, where $\theta \in [0, 90°)$ is the input. Denoting the output of the experiment, at input θ, by $\delta(\theta)$. If n experiments have been performed at inputs θ_1, θ_2, . . . , θ_n, the outputs are δ_1, δ_2,, . . . , δ_n, respectively. A statistical model is a relationship between inputs θ and their corresponding random outputs, $\delta(\theta)$. In this thesis, it is assumed $\delta(\theta) = f(\theta) + e(\theta)$, where $f(\theta)$ denotes a structured component and $e(\theta)$ denotes a random perturbation around the value $f(\theta)$ that is assumed to be normally distributed with mean 0 and standard deviation τ_1.

Here, a non-parametric Bayesian approach is taken. Non-parametric means that the function/model $y = f(x)$ is not assumed to have a specific parametric form. Polynomials, such as $\alpha + \beta x$, are parametric functions because they are determined by a finite set of parameters, which in this example are the intercept α and the slope β. In other words, once α and β are set, the function is determined. There are examples where using parametric functions makes sense, if, for example, we have good intuition through experimentation on the relationship between x and y.

The advantage of using parametric models is that there are few variables to learn so learning the function is quick, however, they are less flexible. Non-parametric models

do not prescribe a specific functional form but they define the class of functions in other ways, as explained below. The Bayesian approach means that the function $f(x)$ is given a *prior* probability distribution, i.e. an initial probability distribution not based on any data that captures the uncertainty about the function, which is then updated online as data is observed, yielding what is called the *posterior* probability distribution.

7.2.3 GAUSSIAN PROCESS SURROGATE MODEL

In this work, a non-parametric Gaussian process (GP) model [32] was used to represent the prior distribution of the function $f(\theta)$.

The Gaussian process model is a class of statistical models that contains functions with normally distributed outputs. A Gaussian process model is characterised by a mean and a covariance function (also called the *kernel*); the former corresponds to an average value in the absence of any data, and the latter models the correlation between different inputs. We denote the mean by μ and the kernel by $K(\theta, \theta')$, where θ and θ' are two inputs. The kernel can be used to impose a certain behaviour to $f(\theta)$. For example, the choice

$$K_p(\theta, \theta') = \tau_2^2 \exp\left\{-\frac{2\sin^2(\pi|\theta-\theta'|/\omega)}{\phi^2}\right\}, \tag{7.1}$$

imposes periodicity to the function with period ω. The notation $|\theta - \theta'|$ means the distance between the inputs, τ_2 is the standard deviation of the normally distributed output, and ϕ is a scaling parameter which determines how much the function is allowed to fluctuate, and generally, the further apart θ and θ' are, the less information about $f(\theta')$ is provided by $f(\theta)$.

7.2.4 LEARNING FROM DATA

Suppose n experiments at inputs $\theta_1, \dots, \theta_n$ gave corresponding outputs $\delta_1, \dots, \delta_n$. The Gaussian process model can be used to provide a prediction for an arbitrary input θ. As mentioned at the beginning of this section, the objective is to propose the next

experiment/input θ_{n+1} that would help locate the minimum of the function. This is determined by evaluating what is known as an acquisition function at untested inputs and choosing the input with the highest value. Suppose that the current minimum value after the n experiments is $\hat{\delta}_n$. Then when a new test at θ is conducted, the acquisition function calculates how much the minimum value is expected to decrease after seeing the new outcome $\delta(\theta)$. Of course, the tested input θ must be decided before the experiment, i.e. before seeing $\delta(\theta)$, which is why it can be regarded as the expected decrease, or more commonly, the expected improvement. Mathematically, the expected improvement (EI) at a test input θ is given by,

$$\mathrm{EI}(\theta) = \mathbb{E}\big[\max\{0, \hat{\delta}_n - \delta(\theta)\}\big]. \tag{7.2}$$

Here, $\mathbb{E}$ stands for "expected value", *i.e.* an average over all possible outcomes of the term in the square brackets over the uncertain output $\delta(\theta)$ for fixed θ. Since the outcome is unknown, all possible outcomes are considered and then averaged. The term $\max\{0, \hat{\delta}_n - \delta(\theta)\}$ is the improvement over the current minimum value, assuming that $\delta(\theta)$ is observed. If it turns out that $\delta(\theta)$ is smaller than the current minimum ($\delta(\theta) < \hat{\delta}_n$), then we have improved by an amount $\hat{\delta}_n - \delta(\theta)$. However, if $\delta(\theta)$ turns out to be larger than or equal to the current minimum ($\delta(\theta) \geq \hat{\delta}_n$), then there is no gain, so the improvement is 0. This proceeds sequentially for $n = 1,2, \ldots$, each time computing *Equation 7.2* for all available experiments, and choosing the one that corresponds to the largest value, i.e., $\theta_{n+1} = \mathrm{argmax}\,\mathrm{EI}(\theta)$. This is illustrated in *Figure 7.1*. In each case it was proposed to test close to the existing minimum, taking into account the function uncertainty.

In this chapter, the preceding optimisation approach was applied to DIMAC through a virtual FE model. The hemispherical and cubic geometries from *Chapter 6* are studied, allowing validation against the experimental results. In the context of Bayesian optimisation, the magnetic clamping process is treated as a black-box function, with the input θ corresponding to the angle, $\theta \in (0°, 90°]$, and the output being the wrinkle metric $\delta_{\max}(\theta)$. This metric was chosen as it was less susceptible to the exclusion of slip in the model. Angles considered were at $2.5°$ steps , *i.e.* chosen amongst $\theta \in$

$\{2.5°, 5°, 7.5°, \ldots, 90°\}$, with the first experiment being at $\theta_1 = 2.5°$. For the statistical model, we set the noise standard deviation to $\tau_1 = 0.5$. Due to the inherent periodicity at 90° due to the magnet positions and the symmetrical shear properties leading to material symmetry at 45° (discussed in *Chapter 4)*, the following kernel was chosen:

$$K(\theta, \theta') = \tau_2^2 \frac{K_p(\theta,\theta') + K_p(\theta,90-\theta')}{\sqrt{\left(K_p(\theta,\theta)+K_p(\theta,90-\theta)\right)\left(K_p(\theta',\theta')+K_p(\theta',90-\theta')\right)}}, \tag{7.3}$$

where $K_p(\theta, \theta')$ is the periodic kernel given in *Equation 7.1*. The Gaussian process standard deviation was set to $\tau_2 = 2$, the period to $\omega = 90$, and the scale parameter to $\phi = 0.5$. A sensitivity analysis of τ_1, $\tau_2$and ϕ revealed the global optima had little sensitivity to these parameters, *Figure 7.2-7.4*. The Gaussian process mean was set to $\mu = 4$ for the hemispheric geometry and to $\mu = 10$ for the cubic geometry using the experimental data. *Figure 7.5* shows the optimisation algorithm deployed in this work as a flowchart.

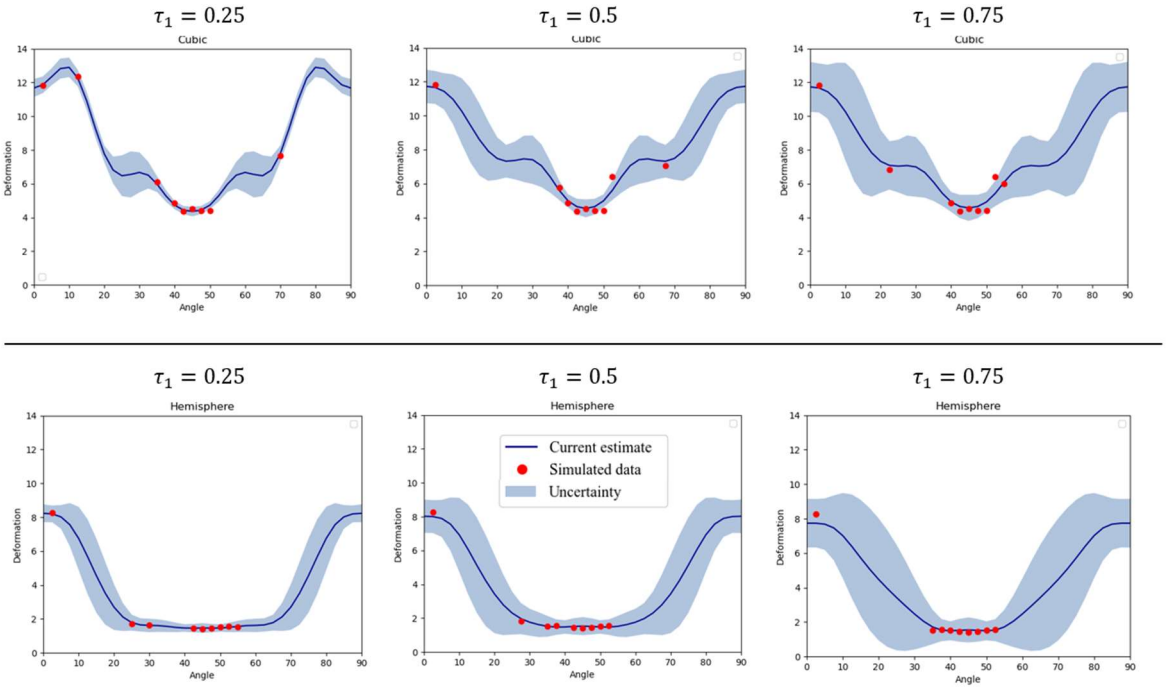

Figure 7.2: Sensitivity analysis of τ_1, with values ±50% of the value used in the study (central), for both cubic and hemisphere geometries.

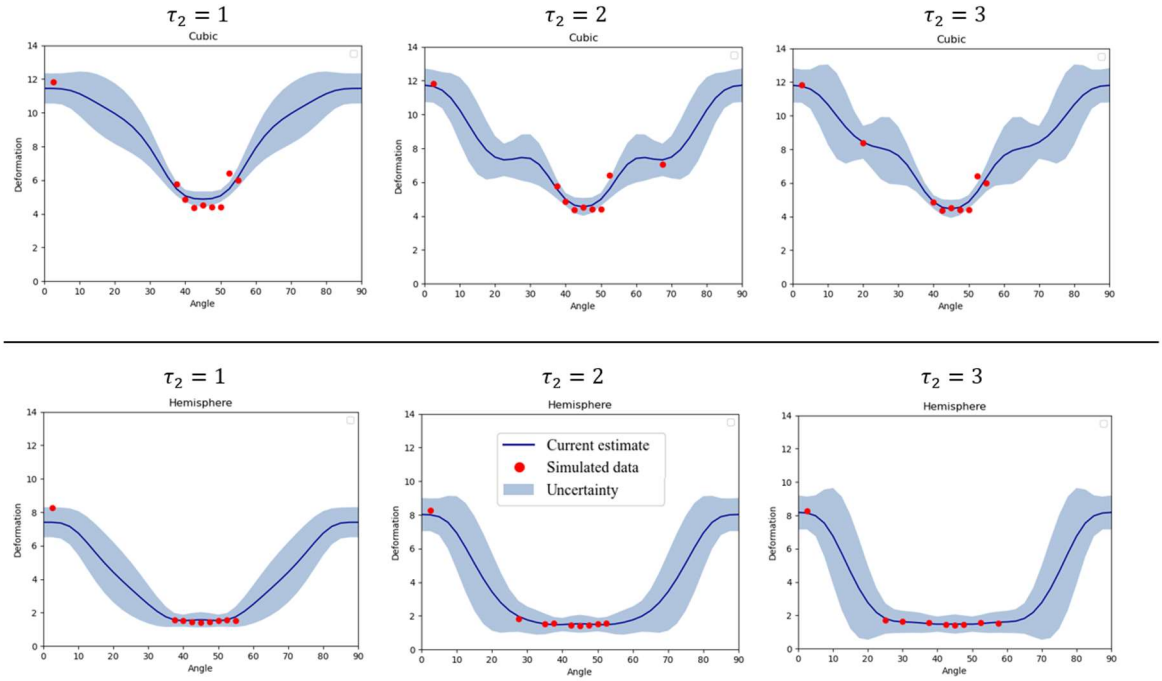

Figure 7.3: Sensitivity analysis of τ_2, with values ±50% of the value used in the study (central), for both cubic and hemisphere geometries.

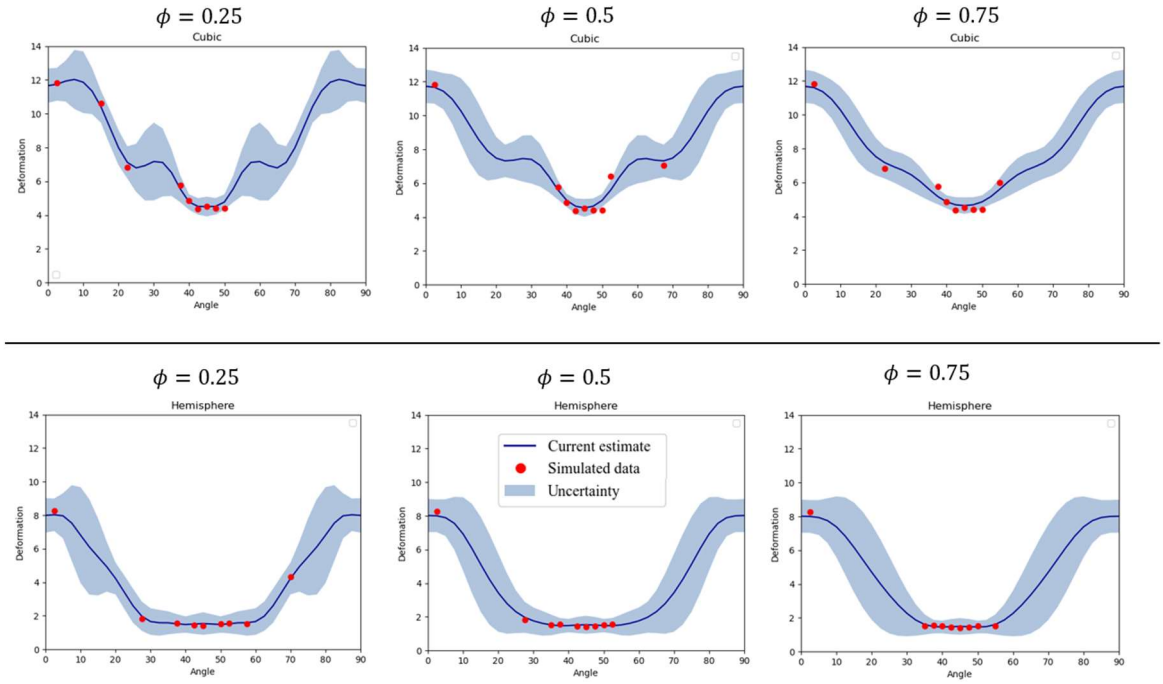

Figure 7.4: Sensitivity analysis of ϕ, with values ±50% of the value used in the study (central), for both cubic and hemisphere geometries.

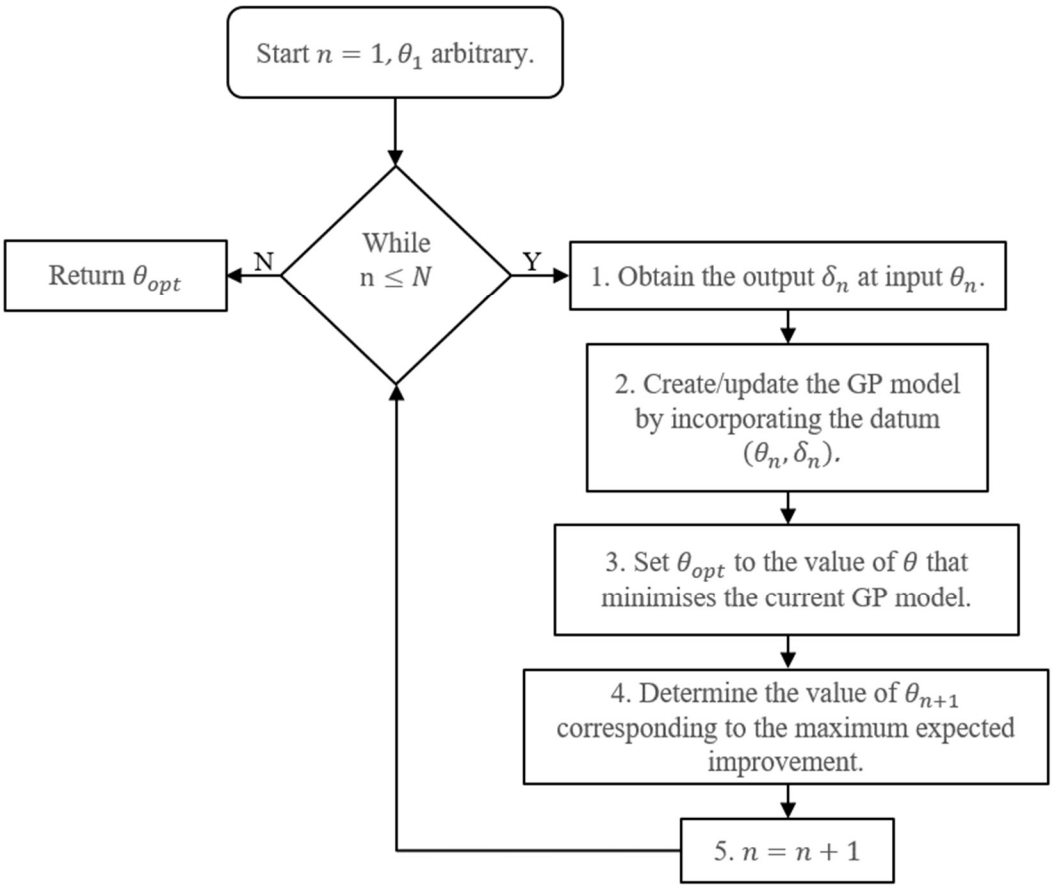

Figure 7.5: Flowchart of the Bayesian optimisation algorithm for finding θ_{opt}, the minimiser of the function $f(\theta)$, after N iterations.

7.3 VIRTUAL PROCESS MODEL

Non-parametric Bayesian optimisation, as discussed previously, offers efficient evaluation of the objective function. In the case of DIMAC, this is to find the optimal magnet position that gives the lowest magnitude of δ. Adding the capability for virtual modelling allows assessment of many more magnet positions. Therefore, first, a virtual process model must be developed that employs the FE material model developed in *Chapter 4*.

7.3.1 METHODOLOGY

A dynamic explicit analysis was again chosen to model the distributed magnetic clamping experimental procedure. This allowed for better contact stabilisation in comparison with a standard analysis and allowed the use of the Abaqus VFABRIC material subroutine (*Chapter 5*). In pursuit of a model that could easily be adapted, a parametrised Python script was written that allows the user to modify many of the key variables, such as: magnet position, clamping force, geometry and stroke depth.

The magnets were modelled as analytical rigid parts with a mass equal to 35 g, a radius of 10 mm, a 0.5 mm fillet and a height of 5 mm. The penalty contact method was chosen, following a Coulomb friction model, with the magnets free to slide relative to the forming bed, whilst allowing the material to also slip. A coefficient of friction equal to 0.2 was used for all surface interactions, except for the interaction between the magnets and the veiled upper surface of the NCF [148] – where instead 0.22 was used. The higher coefficient represents the higher frictional response of the magnet compacting the upper material surface. While highly anisotropic frictional properties of the material were discovered in *Chapter 4*, the addition of a further non-linear material subroutine, such as VFRIC, would dramatically increase computation time. Hence, an isotropic Coulomb approximation was deemed necessary.

The model has two steps: the first initialises the clamping forces to promote numerical stability in the initial increment; the second step is the lowering of the tool, which emulates the tool stroke in the physical experiment for either geometry. On completion, the nodal coordinates are exported for subsequent post-processing in

Matlab. The procedure then follows the same method as the experimental data, calculating the fabric deviation from the tool surface, δ.

With the natural time scale preserved, a small stable time increment could ensue due to the relatively small elastic modulus used for the shell elements impacting the wave speed propagation, thus fixed mass scaling was applied at 10^6. All simulations were terminated after 361 s, indicating successful draw. The simulations were run on the University of Bath's high performance computing (HPC) service Balena, utilising 1 Intel Ivybridge node (7 cpus with 2.6GHz).

7.3.2 VIRTUAL PROCESS MODEL VALIDATION

Axial force values, F_a, from the experimental studies were compared to the virtual process model; *Figure 7.6* shows the comparison when $\theta = 45°$. Here, it is seen that the general trend and magnitude of forces are comparable. Slight deviation could be due to the homogenisation procedure, particularly neglecting compaction and slip in the macroscale model, and including hyperelastic shear behaviour. Further analysis of the internal energy vs. the kinetic energy, validated the model as quasi-static with kinetic energy below 5%.

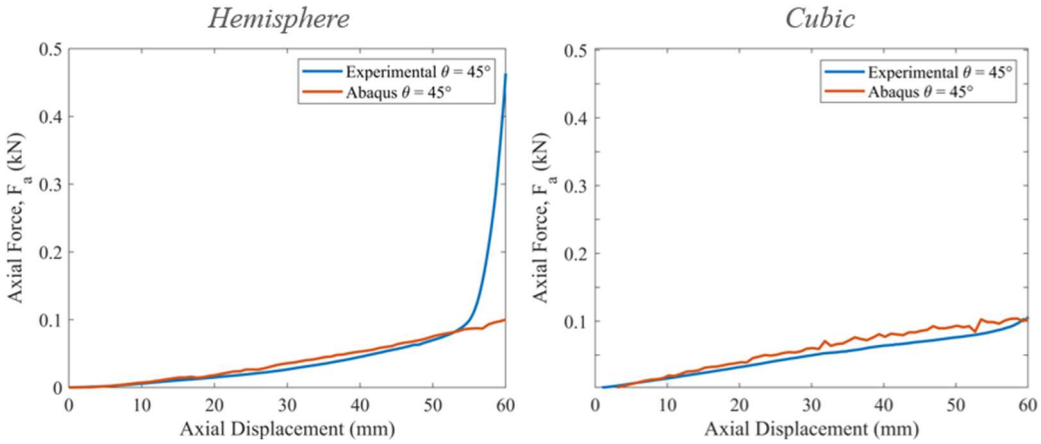

Figure 7.6: Comparison of experimental vs Abaqus results for axial force. Left, hemisphere tool when $\theta = 45°$ and right, cubic tool when $\theta = 45°$.

Inspection of the FEA (*Figure 7.7-7.9*) revealed that wrinkle locations and δ were a good representation of the experimental results. Comparing the wrinkle pattern in the cubic case when $\theta = 0°$ and $\theta = 45°$, shows the major deformation has been represented.

Comparison with the experimental results was undertaken for $\theta = [0, 22.5, 45, 67.5°]$, *Figure 7.8.* The results indicate that the macroscale forming mechanics have been successfully reproduced. In the optimal cases, when $\theta = 45°$, the hemisphere FE results show excellent agreement with the experiment, however the cubic case shows some wrinkles are present on the faces which were not in the experiment. This may be a result of not including slip in the model, instead the model must accommodate the curvature of the corner by pulling more material over the faces. Comparisons when $\theta = 22.5°$ and $\theta = 67.5°$ again reveal that the dominant deformation mechanics have been reproduced. The 's' shape present in these experiments was not as clear in FE, although again this is mainly driven by slip in the physical experiments. The direction of the folds and the locations of material thickening in both geometries do remain good experimental matches. When $\theta = 0°$, for the hemisphere, the locations of the wrinkles approximately matched, however the wrinkle pattern differs. The FE model here appears to highlight the symmetrical shear property that was assigned to the macroscale model that prevents the model capturing these slight material asymmetries. In the cubic example, $\theta = 0°$, the key deformation has been reproduced, albeit the wrinkle pattern on the corner shows differences in folding. *Figure 7.8* does show these differences in macroscale folding, which is possibly due to not modelling the through thickness bending anisotropy.

In NCFs, bending is complex and often nucleates at the mesoscale, hence it may be necessary to further develop the bending model if high fidelity wrinkle patterns are required. In this work, these simplifications allow faster computation, while still representing the key material deformation modes as highlighted previously.

For the hemisphere, when $\theta = 45°$, optimum shear was induced, resulting in parts with minimum wrinkling ($\delta_{75t} = 1.0$ mm and $\delta_{max} = 1.4$ mm). Whereas when $\theta = 0°$, placement resulted in macroscale compression fold wrinkling ($\delta_{75th} = 2.6$ mm and

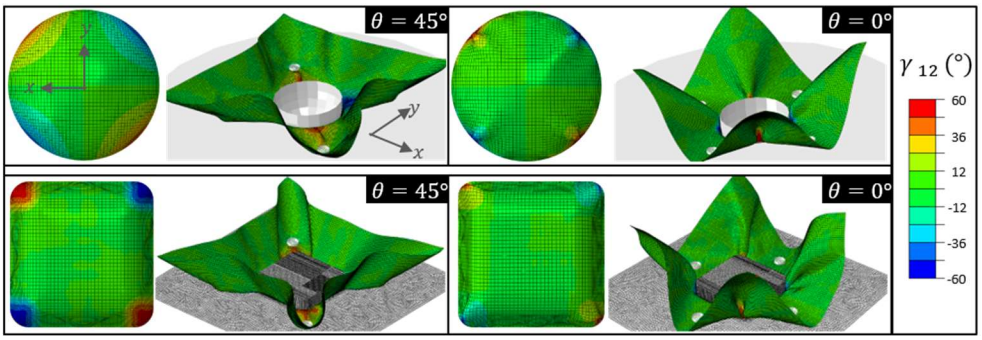

Figure 7.7. Abaqus simulation results showing the shear angle distribution through the material for both the clamped surface and the target part. First magnet at a) 45° and b) 0° for the hemisphere, and c) 45° and d) 0° for the cubic.

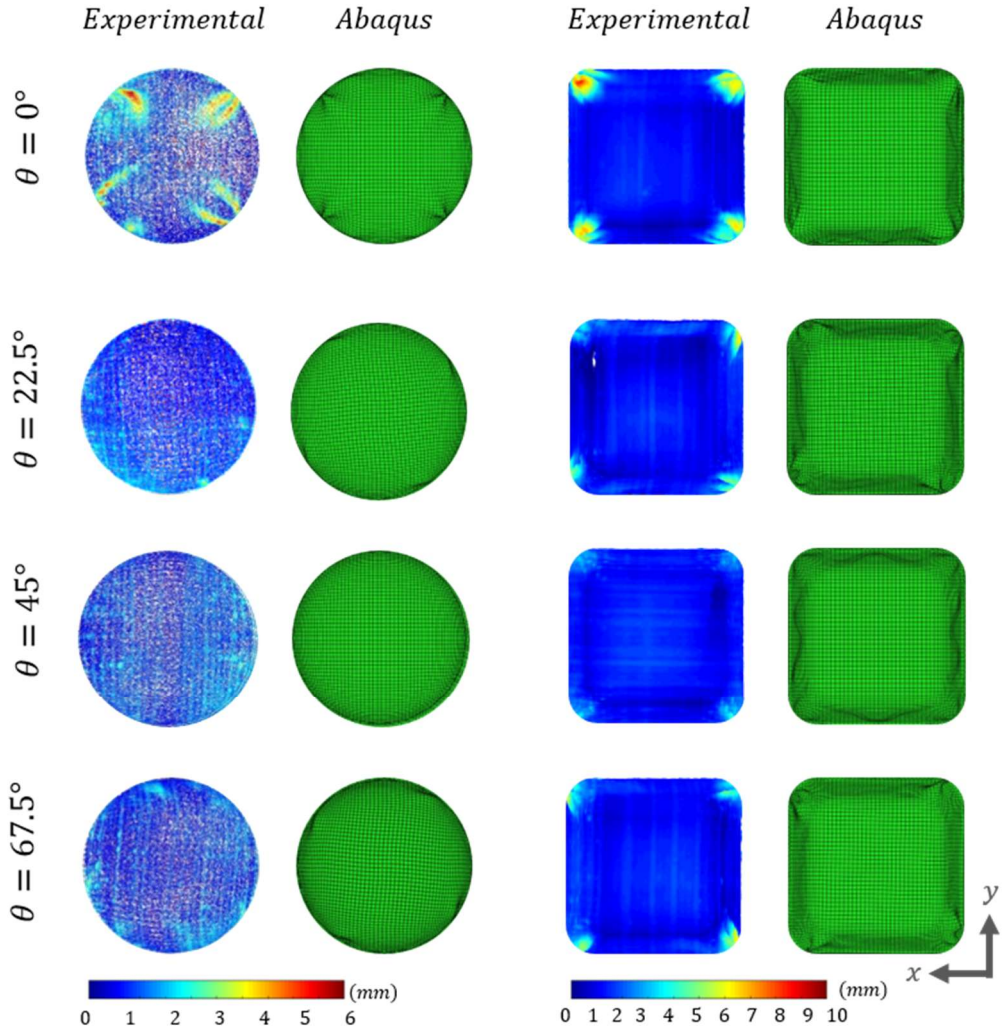

Figure 7.8: Comparison of the experimental and FE results for four example cases. Highlights the macroscale mechanics have been reproduced, showing twist and small wrinkles around the equator, with slight deviations attributed to the homogenisation procedure.

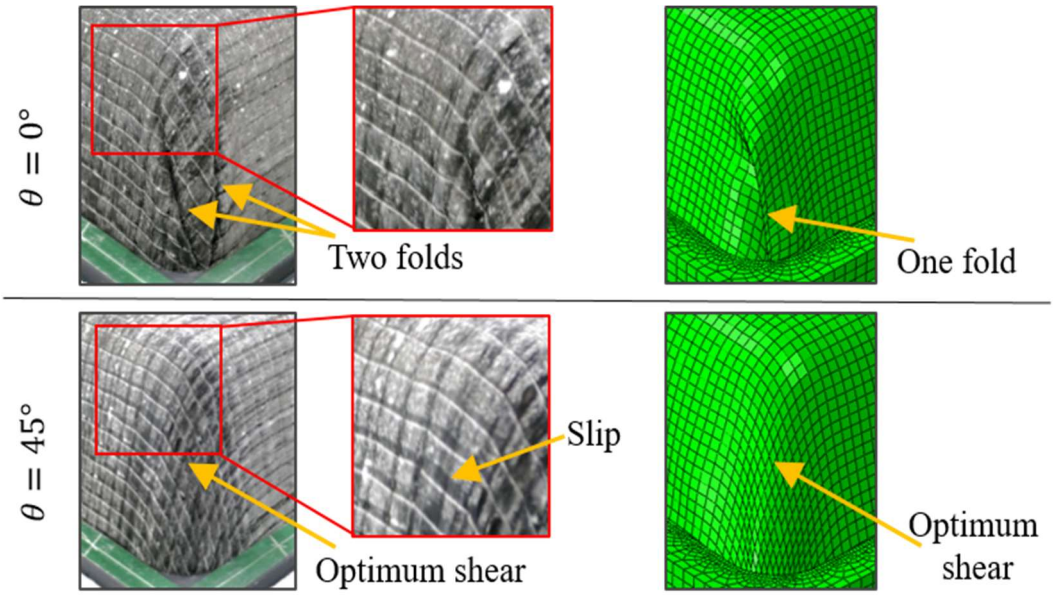

Figure 7.9: Comparisons of the wrinkling patterns for $\theta = 0°$ and $\theta = 45°$ reveal good agreement for the optimal case. When $\theta = 0°$ the macroscale model captures only one fold, opposed to two, due to the efficient homogenisation procedure. When $\theta = 45°$ there was evidence of tow slip in the experiment (indicated), that cannot be captured by the FE model.

$\delta_{max} = 8.3$ mm). For the cubic geometry, when $\theta = 45°$, shear was also induced, resulting in parts with minimum macroscale folds, $\delta_{75th} = 2.2$ mm and $\delta_{max} = 4.5$ mm. Whereas when $\theta = 0°$, macroscale compression fold wrinkling dominated around the corners, $\delta_{75th} = 1.7$ mm and $\delta_{max} = 11.9$ mm.

Further simulations were performed with $\theta \in [0°, \dots, 45°]$, in increments of 5°. The nodal coordinates were plotted in *Matlab* and show the evolution of bending as a result of the adapted boundary conditions, *Figure 7.10.* Confirming the behaviour was as expected.

The in-plane shear stress results for the hemispherical tool configurations when $\theta = 45°$ are shown in increments of 15 mm of stroke depth, *Figure 7.11*. It is evident that magnets activated the shear deformation modes. Here, shear stress initiating from the change in curvature at the forming bed radius increased (by $St = 30$ mm) as the tension induced by the magnets increased. Subsequently, in-plane shear modes were

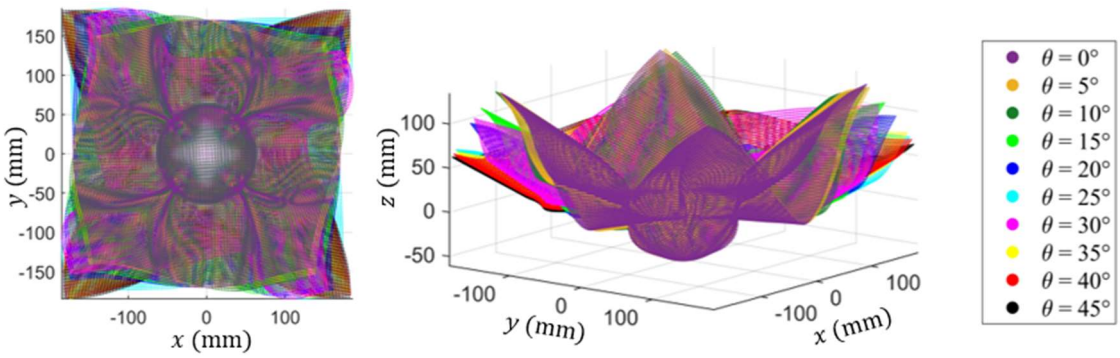

Figure 7.10: FE results for the hemisphere geometry showing the evolution of out-of-plane bending for θ values between 0° *and* 45° *in increments of* 5°.

tension induced by the magnets increased. Subsequently, in-plane shear modes were promoted as the tension between the magnet and hemisphere pole continued to increase. At the same time, out-of-plane bending outside of the magnetic tensile region was initiated, allowing the material to accommodate the shear deformation. This facilitated the material to stretch and develop positive Gaussian curvature. When $\theta = 45°$, the direct fibre modes [119] have relatively little tension, hence these conform to the tool with direct fibre stresses, σ_{11} and σ_{22}.

Mild wrinkling was observed at locations with no wrinkling in the experiment. We hypothesise that slight deviations represent some of the homogenisation strategy for the material model, particularly the exclusion of tow slip and the coarseness of the mesh imposed by computational limitations. Here compaction was not modelled efficiently and has been shown to be significant in similar heavy, thick stitched NCFs [149]. This cannot be represented by standard plane-stress elements. Further, from the out-of-plane bending behaviour, we did not model the through-thickness anisotropy. These factors however did not alter the major characteristics of the deformation, particularly in the membrane-driven deformation area around the tool geometry.

In the physical experiment, the compaction of the fabric between the radial insert and the tool is thought to drive the final important stage in inducing peak in-plane tension and shear. In the simulation this was also present, but to a lesser extent due to

a reduction in compressibility. This may have led to an underestimation of the effect of compression at this interface, reducing the in-plane tension generated across the material, and reducing conformity to the tool. Albeit the optimisation results presented later show the model is effective at indicating the optimal solution.

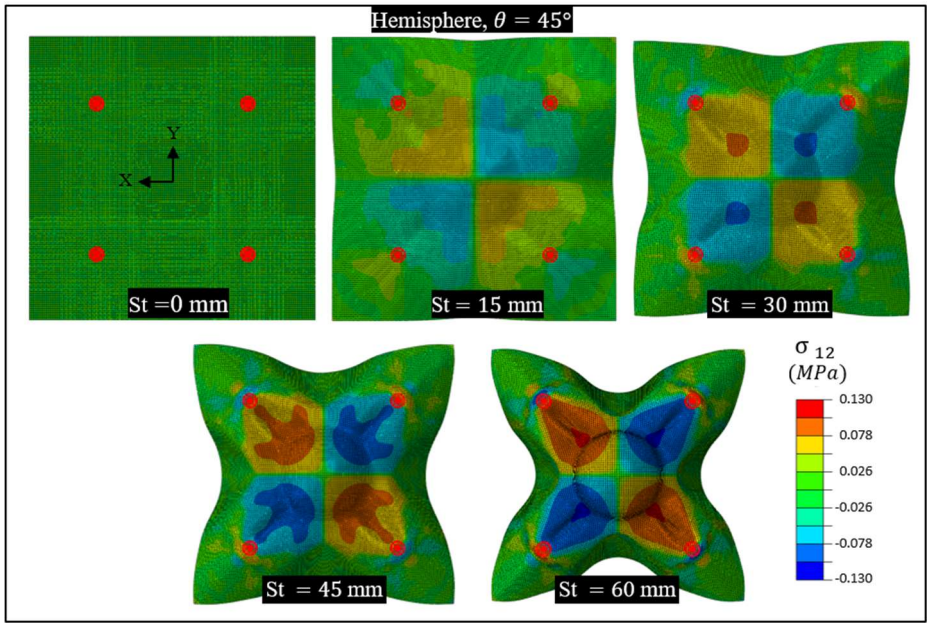

*Figure 7.11: Abaqus in-plane shear stress, σ_{12} , results for the full blank when $\theta = 45°$ at 15 mm stroke depth (*St*) intervals. Magnet positions superimposed (red).*

7.4 BAYESIAN OPTIMISATION APPLIED TO DIMAC

The optimisation procedure for the two geometries took 5.25 days (hemisphere) and 9 days (cubic) to complete 9 simulations ($n = 9$), (*Figure 7.12-7.13)*. The discrete rigid description of the cubic tool explains the increased computational demands. It is noted that after 5 simulated experiments, both the cubic and hemisphere geometry results already exploit the area around $\theta = 45°$, indicating this as the optimum. After 9 tests, the hemisphere and cubic geometries minimum is clear, with relatively little uncertainty

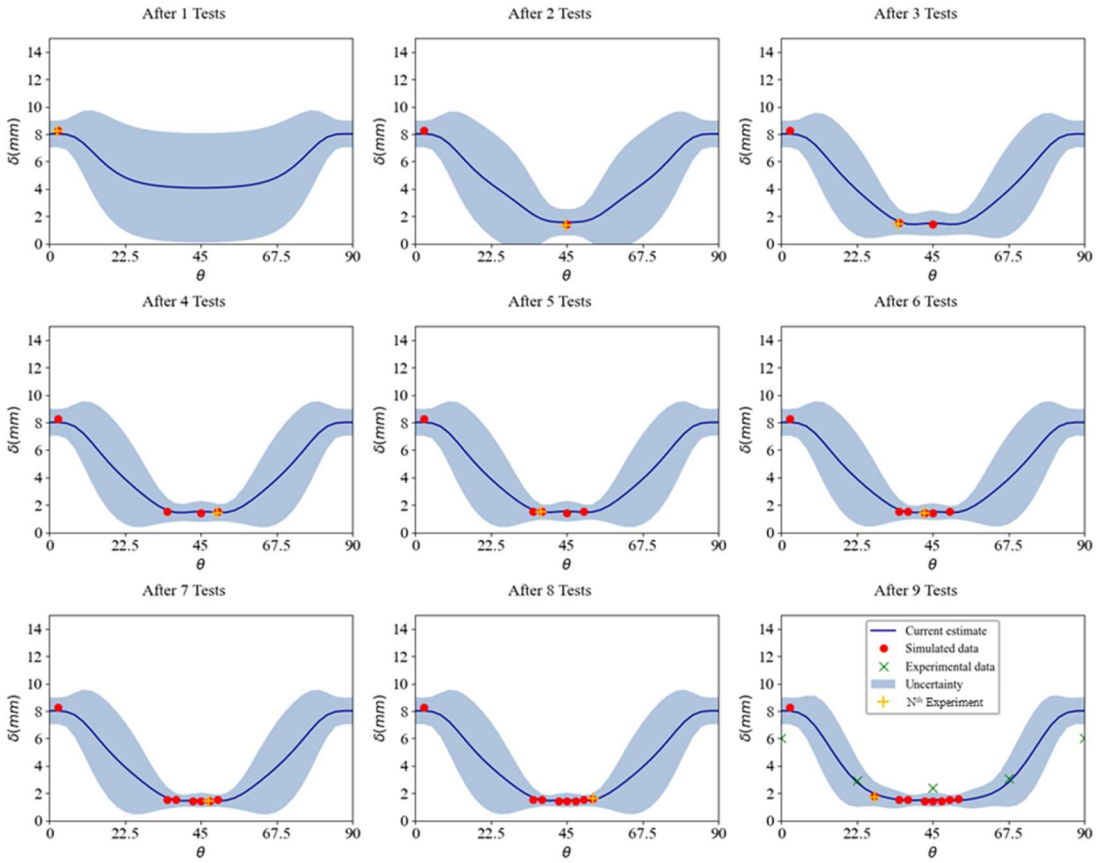

Figure 7.12. Bayesian optimisation stages for the hemispherical tool using FE simulation results, δ_{max} (red), and comparison with experimental δ_{max} (green) after 9 tests. The mean of the distribution is represented by the thick blue line (current estimate) and the uncertainty denotes the 95% confidence interval for the value of the function.

around this point. The initial six iterations were spent learning about the overall shape of the function, while the last two are more focused around what is believed to be the lowest value. Thus the algorithm balances exploration and exploitation as discussed in the previous sections. Note that the 9th experiment is proposed to be away from the minimum as the algorithm understands that there is not much more to gain in that region and instead chooses to explore the function some more. So far, the number of optimisation iterations, n, is set by the user. In more complex geometries this may mean more than nine iterations is necessary. From *Figure 7.14,* where the optimisation was run with $n = 19$, it can be seen that there was little gain for this geometry. Hence, $n = 9$ was valid for this study. The approach highlighted an intrinsic ability to balance

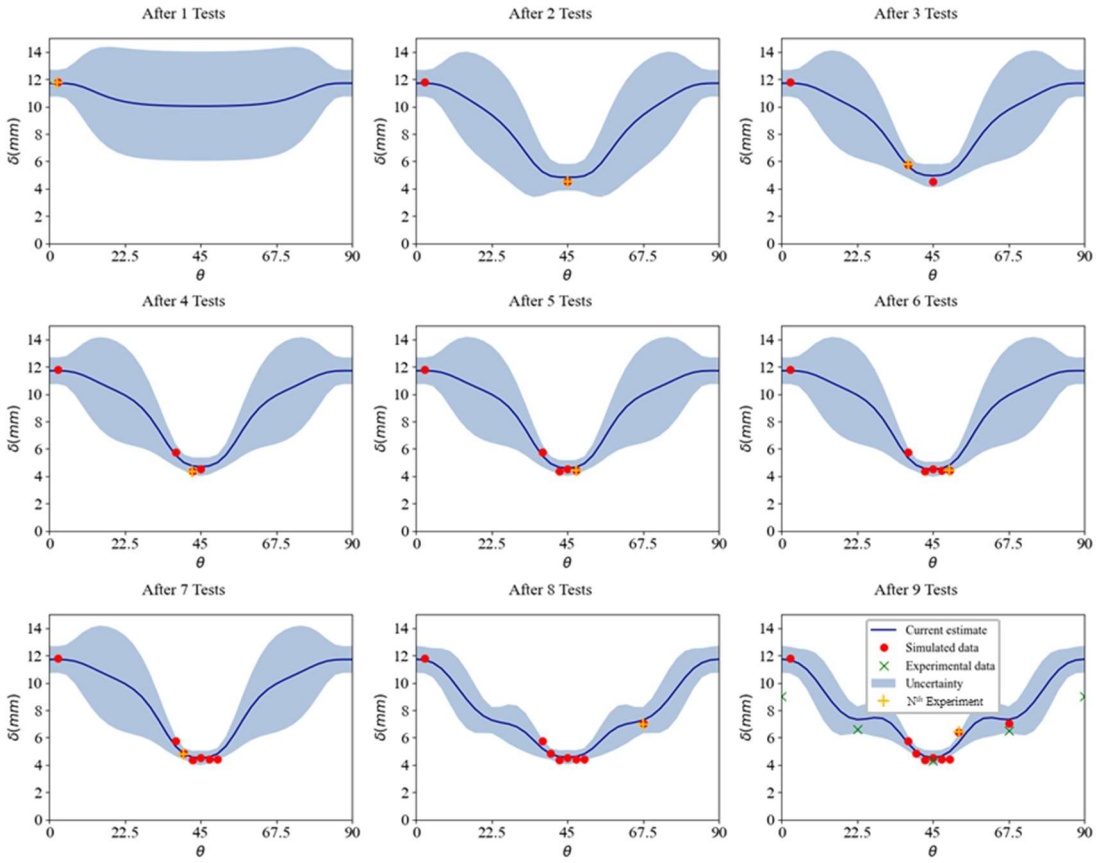

Figure 7.13: Bayesian optimisation stages for the cubic tool using FE simulation results, δ_{max} (red), and comparison with experimental δ_{max} (green) after 9 tests. The mean of the distribution is represented by the thick blue line (current estimate) and the uncertainty denotes the 95% confidence interval for the value of the function.

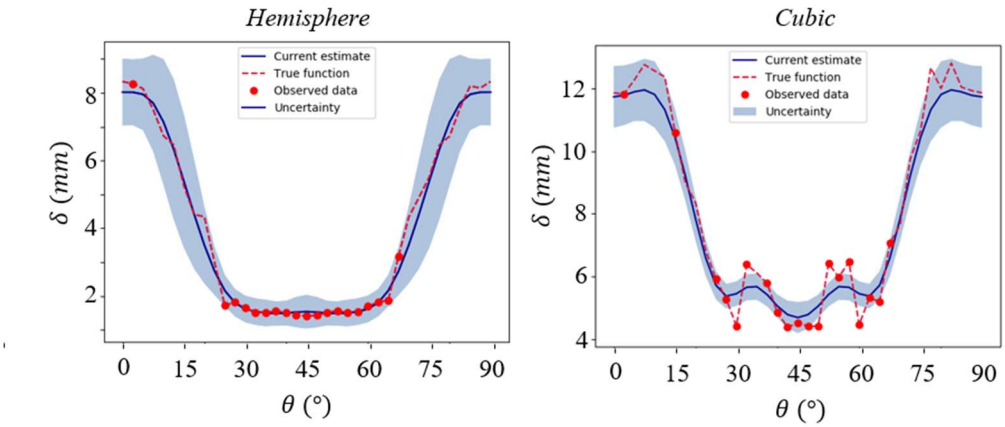

Figure 7.14: Bayesian optimisation results for the cubic and hemisphere geometries after 19 iterations.

exploration and exploitation and through each stage it demonstrated the ability of the algorithm to select the magnet location that offered the most probable expected improvement.

The final panel of *Figure 7.12* and *Figure 7.13* also illustrate δ_{max} for the experimental results, plotted for comparison after 9 tests. There appears to be phase changes in response throughout the domain, particularly in the cubic case. This could indicate where wrinkles changed between a larger amplitude wrinkle and multiple smaller wrinkles. To further assess the metric, δ, simulations were performed for thirty-six values of θ, where $\theta = [2.5°, \dots, 90]°$. Results were subsequently post-processed to calculate the 55^{th} to 100^{th} percentiles in *Matlab* in increments of 10. *Figure 7.15* documents the results, where the global minima indicates an optimal result around $\theta = 45°$. Note that $\delta_{100\text{th}}$ is equivalent to δ_{max}. The clearest minima in both geometries appears to be δ_{max}. The cubic geometry also appears to have more fluctuation in δ, than for the hemisphere. This may be due to the added geometrical complexity, and these areas may still indicate local minima. Further statistical evaluation may be beneficial in future studies.

This eludes to the need for a metric or set of metrics that would be able to encompass many more statistics to fully characterise the forming behaviour and resulting deformation. Metrics such as wrinkle area and curvature have previously been demonstrated in [150]. Statistical inference models could therefore allow combinations

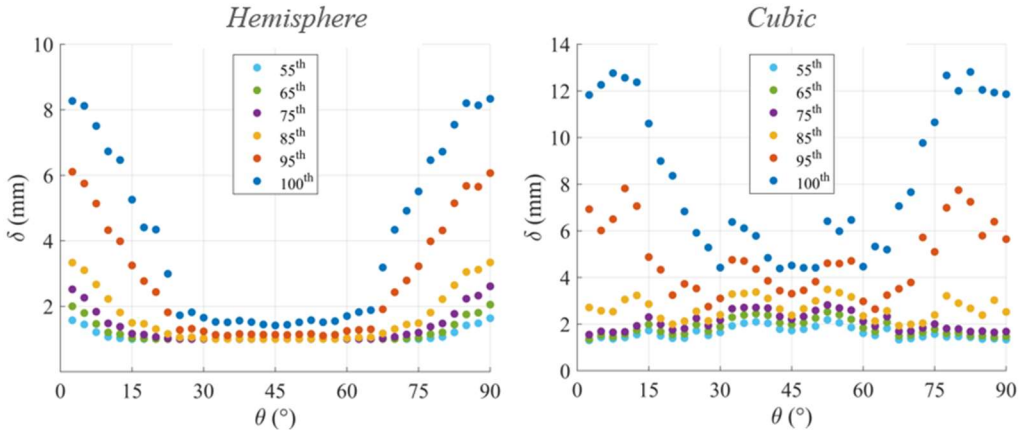

Figure 7.15: Results for $\theta = [2.5, \dots, 90°]$ for both tested geometries showing the 55^{th}-100^{th} percentiles of δ.

of metrics in an automated post-processing application. Whilst the optimisation had a feasible run-time, this could be further reduced to improve the utility and allow efficient global optimisation models based on process segmentation and image analysis.

7.5 CONCLUDING REMARKS

This chapter further highlighted the advantages of DIMAC, particularly the ease of applying powerful optimisation strategies. Some final remarks:

- The macroscale FE strategy used in this study was an efficient and effective approach. The coupled idealised shell and membrane elements approach, where two element sets shared mutual node sets, was validated.
- Validation of the FE model revealed it could capture the primary material deformation. This was particularly good in the optimal cases, however, when complex compression folding occurred in sub-optimal cases, the patterns had some differences. With the employed macroscale homogenisation this was to be expected, as bending often initiates on the mesoscale.
- Gaussian process modelling of the deviation from the target shape, using a periodic kernel, and the use of Bayesian optimisation to find the optimal angle, were demonstrated. Results highlight that surrogate modelling and Bayesian optimisation were effective strategies for distributed magnetic clamping.
- The developed metric for preform quality, δ, was effective, with the maximum value showing the greatest correlation with preform quality. Statistical inference could be beneficial to reduce unexpected noise, which otherwise may result in local minima in more complex geometries.

CHAPTER 8

MULTIPLE PLY PREFORMING OF NON-CRIMP FABRICS WITH DISTRIBUTED MAGNETIC CLAMPING

A major barrier to high-rate manufacture of non-crimp fabric (NCF) preforms is the relatively low volume of research evaluating multiple ply forming strategies. This study presents an extension to the Distributed Magnetic Clamping (DIMAC) method towards establishing flexible process control measures for multiple ply forming. The measure of wrinkling, δ, is adjusted to allow comparison across different stack thicknesses and the distributions of wrinkles are shown to correlate with process parameters in an experimental parametric study. Further, ply-bending mechanics are shown to have a dominant effect on the draw-in of compression folds, particularly when increasing the number of equivalent biaxial plies. However, by deploying targeted distributed clamps, three-ply, single-stroke strategies over a complex positive curvature geometry become viable. DIMAC is shown to facilitate the local adjustment of boundary conditions whilst offering flexibility in improving component quality.

8.1 INTRODUCTION

High-rate automated resin transfer moulding (RTM) remains a challenge in the production of fabric composites. Non-crimp fabrics (NCF) in particular, due to complex material structure, represent the state-of-the-art in highly engineered materials. Manual processes still dominate production, with complex geometrical features representing challenges for automation. For example, automated tape lay-up (ATL) is hindered by minimum turning radii [50] and is only capable of intermediate geometrical complexity [151]. Drape forming has offered the most promise to date towards reduced cycle times and flexible tooling. However, drape forming processes offer little opportunity to control boundary conditions, greatly reducing the flexibility to influence the deformation and react to process-induced defects. What is more, composite forming processes can be highly variable which adds uncertainty and reduces the viability of machine learning and statistical inference towards process optimisation. Formability control approaches range from the addition of risers in double diaphragm forming (DDF) [109] to an operator manually pulling and relaxing the membrane over the tool in single diaphragm forming (SDF) protocols. These measures often further exacerbate variability. As discussed in the introduction, continuous development of material systems and product geometries demand a solution that is highly repeatable, has adaptable process control measures, is translatable to different materials and offers process flexibility at different length scales. Despite the complexity of NCF materials, their architectures typically result in orthotropic properties and distinct energetically-favourable deformation modes. Hence, there is an opportunity to improve multiple ply forming through tailored control during forming operations.

Most manufacturing processes still rely on a ply-by-ply approach, which is time-consuming and resource-intensive, thus motivating industry to push towards the capability to lay down multiple ply stacks in one forming operation. Multiple ply forming of NCFs remains a challenge with relatively little research in this area [94, 129, 152, 153]. Interply friction is a key manufacturing barrier when aiming to increase stack size, due to the high frictional anisotropy governing the complex surface interaction which can initiate wrinkling [7, 11-12]. Contact effects however are often exacerbated

when using process control measures that limit bending and force surface interactions, such as DDF, SDF and processes employing full circumferential blank holders. Reducing the constraints imposed on the material away from the target part, can facilitate out-of-plane deformation, which partly compensates for interply frictional effects.

DIMAC was designed to work towards an automated, intelligent, RTM system. Results were previously discussed in *Chapter 6* that highlighted its applicability in activating shear stretching modes to increase formability over single-ply forming scenarios. It was also demonstrated, through a validated FE homogenisation scheme (*Chapter 5)*, that Bayesian optimisation was effective in finding the optimal boundary conditions (*Chapter 7)*. The process is similar to press forming but a conventional blank holder is replaced with permanent magnets. These can be easily distributed across the surface of the sheet to affect boundary conditions and to influence local deformation mechanics. The intention is to improve component quality by preventing the emergence of wrinkles. However, to further validate DIMAC as a candidate for industrial development, increased understanding of single-stroke multiple ply forming is needed. Increasing the rate of production is antecedent to reducing the high cost of composite material part manufacture, allowing further added value not only to the aerospace and automotive sectors, but also to the national productivity strategy. Here, DIMAC is used to form multiple-ply stacks of NCF. The efficacy of increasing the number of plies formed in one operation is demonstrated and highlights some of the defect mechanisms that can be avoided through the addition of distributed magnetic clamps.

8.2 METHOD

8.2.1 DISTRIBUTED MAGNETIC CLAMPING PROCESS FOR MULTIPLE PLY FORMING

Experiments were performed with the [90v0v] biaxial NCF as set out in *Chapter 4.* For the purposes of this study, the front was again defined as the 'fibre side' with stitches orthogonal to the 90° fibre and the back is defined as the 'veil side'. The Distributed Magnetic Clamping test apparatus was also adapted to facilitate multiple plies. This required six additional forming beds to accommodate the extra material. The radial inserts took the geometry of the tools widest circumference on the xy plane, plus the nominal material thickness. This meant that for the NCF material studied here, 1 mm was added to each of the radial inserts central exclusion offset, from the tool perimeter, with each ply. After the deductions made in *Chapter 6,* where it was concluded the blank size could be reduced, blank sizes used in this chapter were 300 x 300 mm.

The NCF blank was placed on top (veil side up) of the forming bed and clamped in place using the magnets. The material was aligned with respect to x and y (*Figure 8.1-8.2*), except for the offset (OS) and quasi-isotropic (QI) cases. In the OS test, each ply was spiral stacked undergoing a 22.5° rotation about z. In the QI example, the central two plies were instead both rotated 45° about z. Four magnetic clamps per ply, were the minimum required to promote orthotropic in-plane shear deformation. Polar coordinates $[r, \theta]$ are used to indicate the location of the magnets. This arrangement was defined with the coordinates $[150\ \text{mm},\ \theta + i90°]$, where $i = 0, 1, 2, 3$. As biaxial materials exhibit four key deformation modes [119], these were split into shear mode and fibre mode. Shear mode represents stretching at the midline between the NCF's fibre axis, through tow rotations about the pillar stitch. Fibre mode refers to boundary

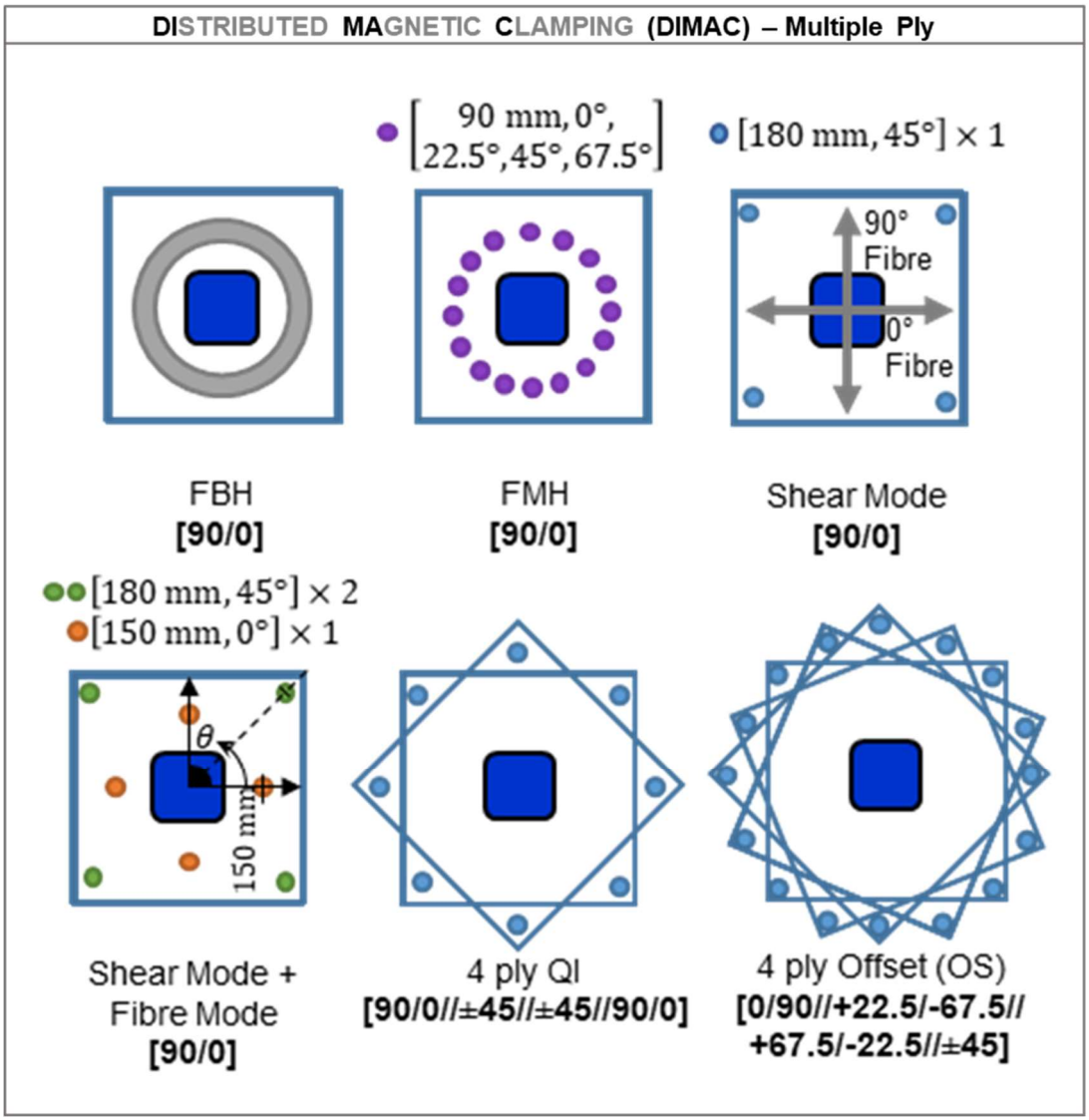

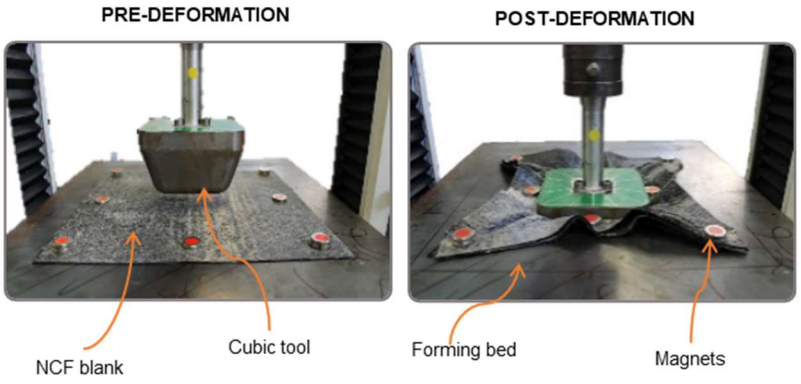

Figure 8.1: (Top) The boundary conditions tested in this study with the origin of the coordinate system at the centre of the tool and polar coordinate definition. (Bottom) Distributed magnetic clamping method showing the process pre- and post- deformation.

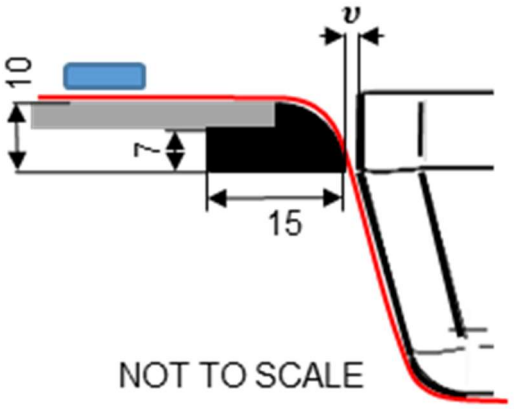

Figure 8.2: Cross section of the radial insert and forming bed showing the 3D printed radius bonded to the forming bed occlusion.

control along the fibre length. All fibre mode magnets were placed at radius 150 mm, with all shear mode magnets at 180 mm. Hence, a *shear mode* distribution of four magnets is given as [180 mm, 45°], and a *fibre mode* distribution of four magnets as [150 mm, 0°] for brevity. Further experiments doubled the magnetic clamping force by doubling the number of magnets at each location. To define these, a multiplication factor is indicated, hence a *2 × shear mode only* configuration indicates two magnets were stacked at each of the polar coordinates.

A further set of experiments was undertaken using a conventional full circumference blank holder (FBH) to reveal wrinkling differences to DIMAC. This was made from mild steel and had an annular geometry (2.13 kg, 180 mm inside-diameter, 198 mm outside-diameter, 48 mm depth). To facilitate comparison, experiments using a "full *magnetic* holder" (FMH) were also conducted by placing 16 magnets as

described in *Figure 8.1* at a radius of 90 mm. Permanent cylindrical magnets (N42) were employed in this study (diameter = 20 mm, thickness = 5 mm) with a clamping force of 90 N. In all cases the tool was lowered at a constant rate of 20 mm/min and began at the top of the material stack. This required stroke adjustment to accommodate the varying stack thicknesses and was calculated through the addition of the tool depth, radial insert depth and stack thickness, υ.

8.2.2 ADJUSTED MULTIPLE PLY DEFECT METRIC

Photogrammetry was used to capture the final surface and produce a representative point cloud. The wrinkle metric δ, developed in *Chapter 6*, does not allow comparisons of different ply thicknesses in its current form. Hence, development of an adjusted wrinkling metric for multiple ply preforms was achieved by subtracting the stack thickness. This not only facilitates comparison in this study, but also feeds into the generation of diverse data sets where learning can be shared across different forming procedures.

The process allowed comparison across different ply thicknesses, and utilised the software package CloudCompare [154]. This open-source software was selected to perform part of the calculation, in place of the algorithm developed in *Chapter 6.* This not only increased the computational efficiency, with CloudCompare four times faster than the method in *Chapter 6,* but also allows simple visualisation of the process. First the tool was re-meshed with target size of 1 mm. The distance of the outer surface of the material from the tool along the normal to the tool surface, δ, was calculated with the software package CloudCompare. Finally, to adjust for various ply thicknesses, the idealised ply thickness υ, was subtracted from δ. This calculation was performed at every node of the tool's mesh and is represented by the metric δ_N. Positive values of indicate thickening or the emergence of wrinkles, while negative values represent stretching and thinning of the material as it is pressed against the tool. Calculating δ_N at each point in the point cloud (~1 million points), also allows assessment of the spatial distribution of defects.

8.3 RESULTS AND DISCUSSION

The distributions of δ_N for all experiments are shown in *Figure 8.3* and the point clouds in *Figure 8.4-8.7* The metric produced a comparable data set with all medians close to 0. Analysis of these results is presented in three subsequent sections: *increasing the number of equivalent biaxial plies*, *increasing blank holder force (BHF)*, *varying magnet placement*, and finally *varying fibre angle*. First, the standard control method using a FBH revealed that by fully constraining the fabric in-plane, the median and maximum of δ_N were consistently higher than for the FMH cases up to three plies. For FMH at four plies, the maximum of δ_N was ~1 mm larger than for FBH, however the median was still reduced. This revealed that the metric could distinguish some process-induced secondary deformation modes, such as fabric compaction, caused by tricot stitch deformation, fibre nesting, and the increased in-plane tension imparted by the magnets.

Increasing the number of biaxial plies

Initiating only shear mode boundary control led to the draw-in of large compression folds. A thickening was observed at the corners, caused by compaction of the fibre bundles. In the single ply trial, thickening is seen in *Figure 8.3* (1 × shear mode only), where the curvature of the fibre path, and subsequent increased thickness, is highlighted by the magnified insert. As the number of plies was increased, compression folds appeared at the lower portion of the corners and on the faces. Observing the top surfaces confirmed that the coupling of plies raised the stiffness of the stack, something that is well understood by the increase in cross-sectional area. This increased stiffness, as well as increased interply shear, led to a draw-in of compression folds. Compression folds occurred when there was a lack of in-plane tension. Buckles on the faces evolved in magnitude with every additional ply. However, the experiment provided a basis from which to adapt boundary conditions in pursuit of high quality two or three ply forming.

Increasing blank holder force

An improvement to formability was found by increasing the BHF, which is consistent with other studies [115, 126]. Doubling the clamping force has brought the median of

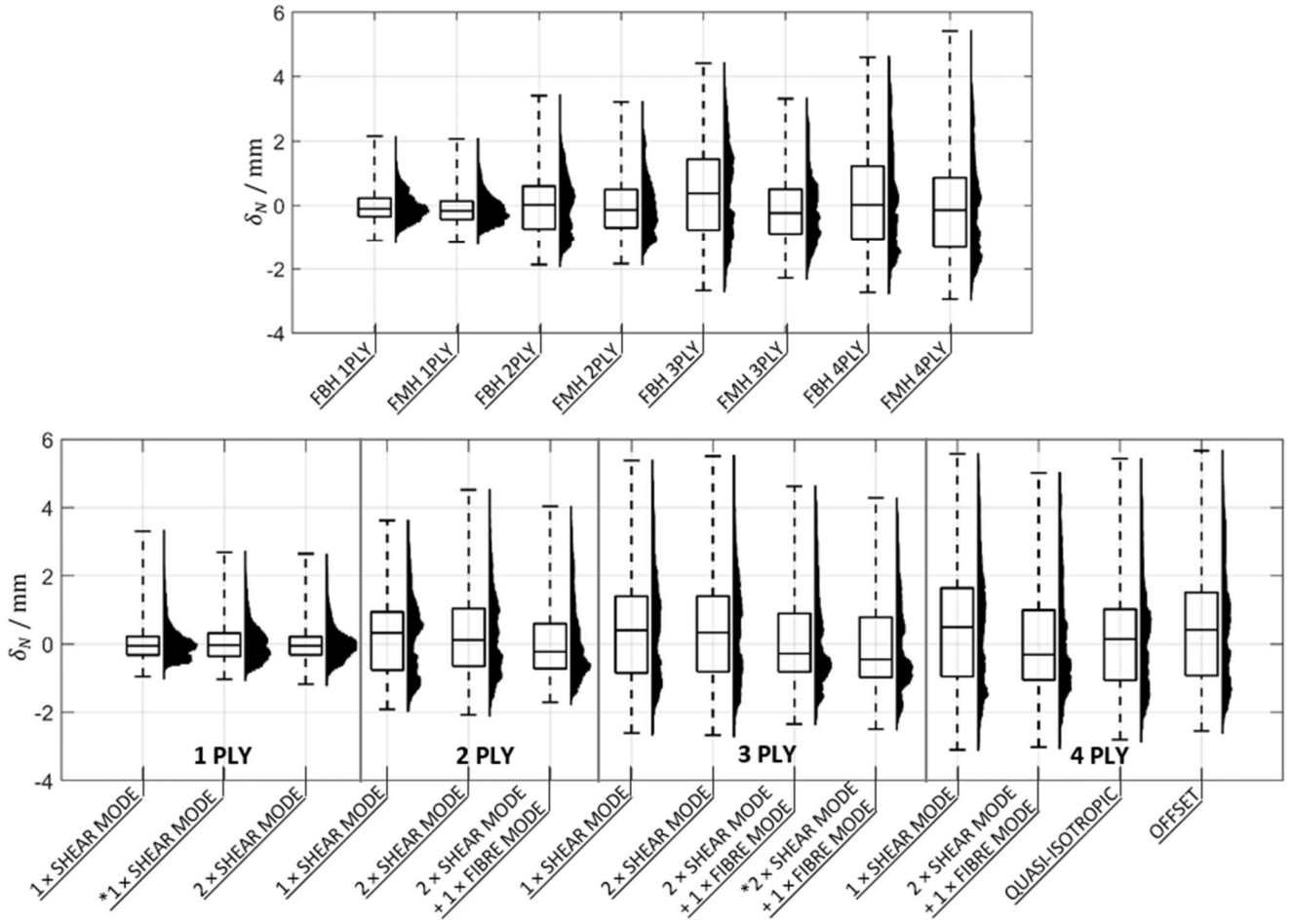

*Figure 8.3: Resulting histograms and boxplots of δ_N for all experiments showing the impact of boundary conditions to formability and material distribution. Repeated experiments indicated by * showing the low variance between metric statistics.*

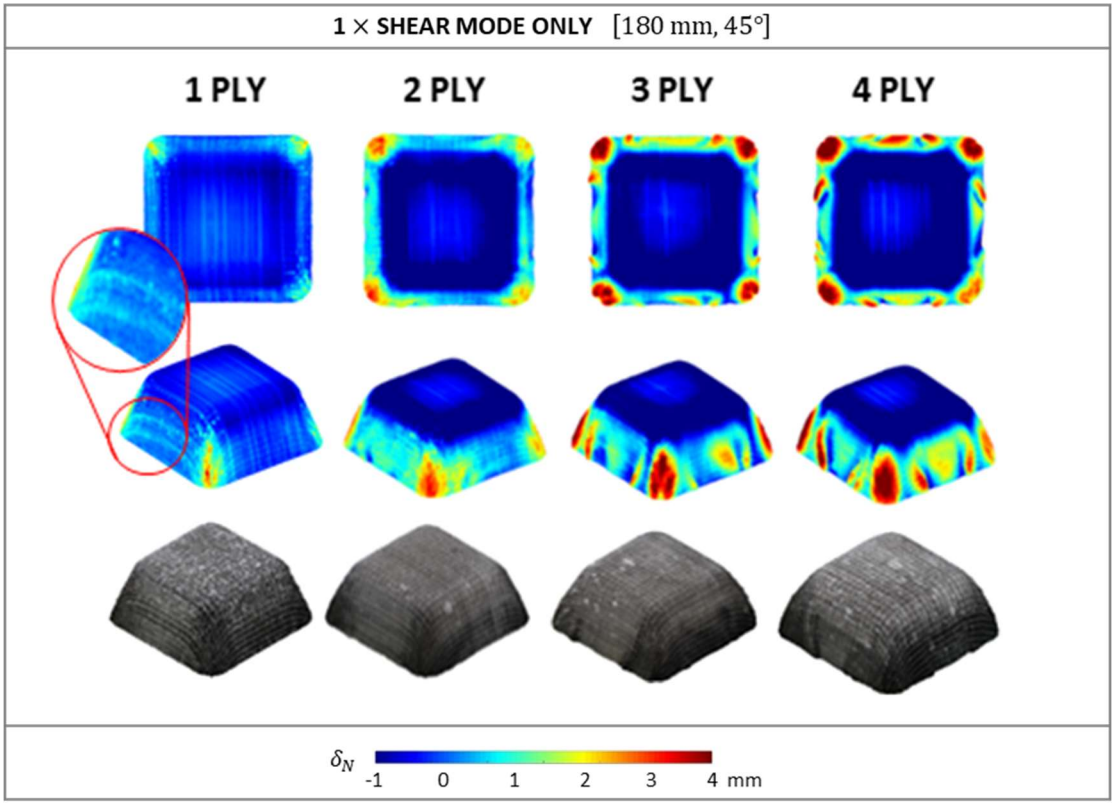

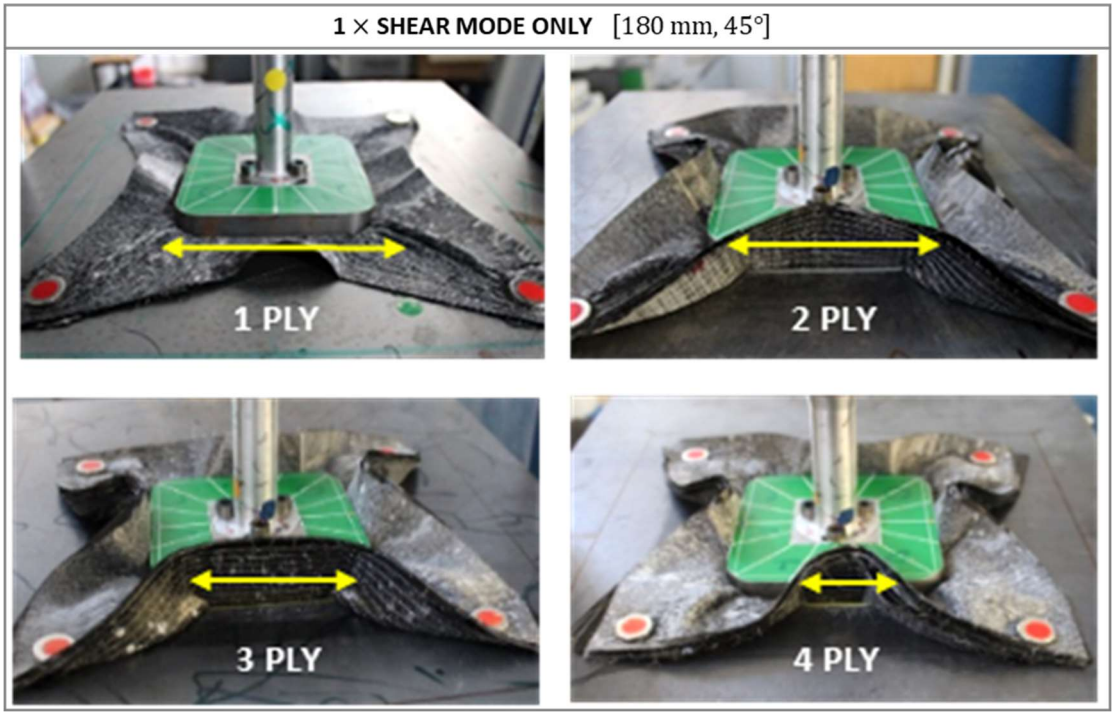

Figure 8.4: Formed shapes for increasing number of biaxial plies with 1 × *shear mode only boundary control and (bottom) top surfaces of the tests show the increasing stack stiffness with increasing plies and its impact on the evolution of bending between magnets and the draw-in point around the radial insert.*

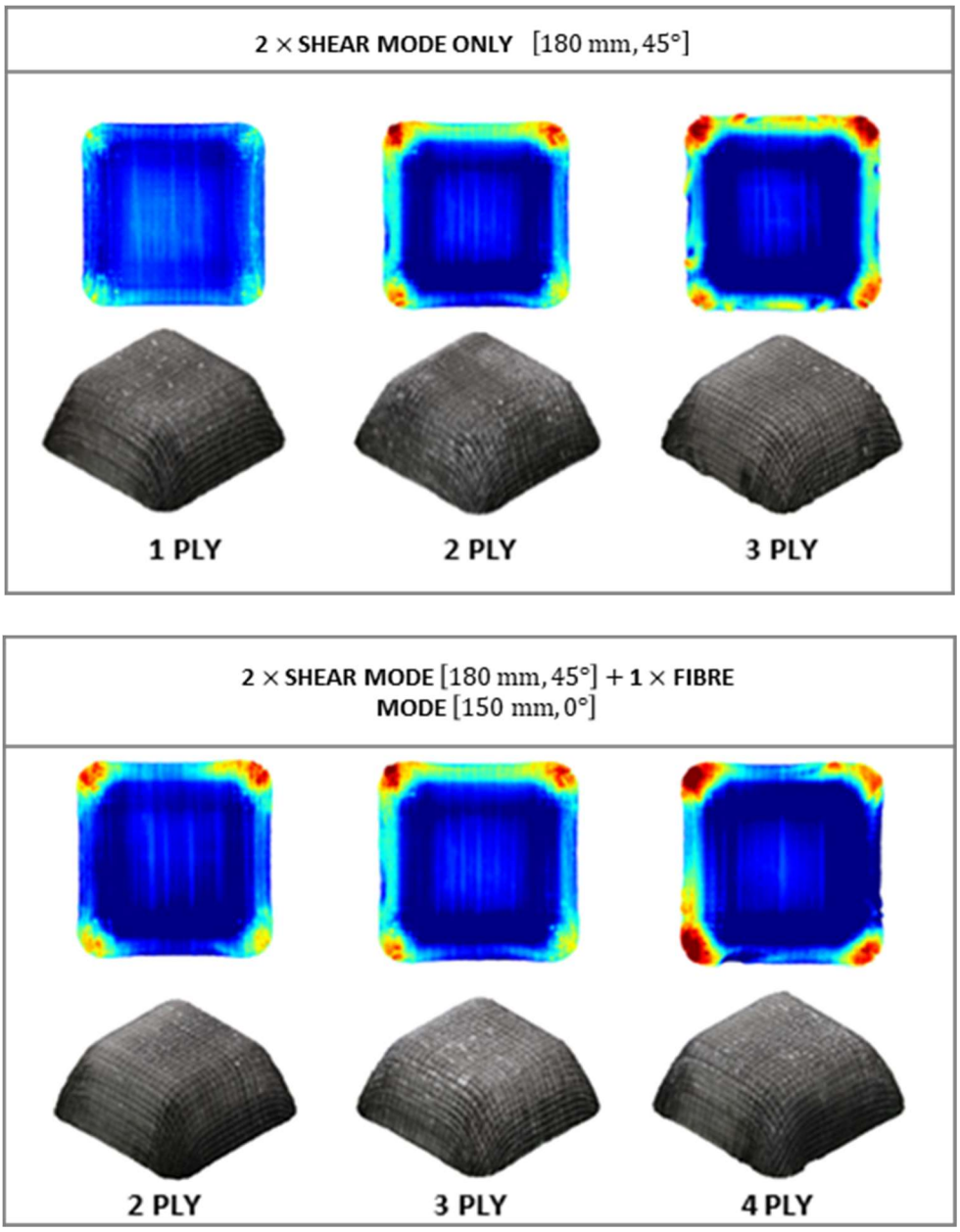

Figure 8.5: Formed shapes for increasing number of biaxial plies with, 2 × *shear mode only, and* , 2 × *shear mode* + 1 × *fibre mode, boundary control parameters.*

δ_N, in every case, closer to zero, indicating reduced wrinkling. By examining the histograms in comparison with the 1 × shear mode forming trials, a frequency reduction of larger δ_N values confirms this improvement. However, increasing the shear stress by doubling the magnet strength had no impact on the large compression folds that appeared at three plies and above.

Varying magnet placement and adapting boundary conditions

Detrimental compression folding and fabric buckling was addressed through additional "fibre mode" magnets. This added boundary condition (1 × fibre mode) as well as the "2 × shear mode magnets", prevented the draw-in of defects on the faces. The hotspots on the corners (see *Figure 8.6*) show that, even up to three plies formed in a single stroke, compression folding was reserved to the lower 10 mm. This leaves much of the geometry at three plies defect free. The histograms confirm that with all δ_N median results negative, most material adhered to the tool surface. The lengths of the positive tails have reduced and the range of δ_N is smaller.

Adding the second boundary condition initiated fibre mode tension between each magnetic clamp and the material's area of contact on the tool. This reduces the draw-in of the unconstrained material between clamps by increasing the in-plane tension. The fibre mode boundary condition also reduced the distance between each consecutive set of magnetic clamps. As the magnets slide in towards the tool, the fibre tow passing between the magnets must undergo compressive stress. Once this reaches a critical load, the fabric must buckle. However, by reducing this distance with the addition of another magnetic clamp, the critical load is increased. This reduced the effect of increased bending stiffness and produced two smaller amplitude buckles on the top surface while at the same time leading to a reduction in compression folding on the planar faces. This is highlighted in the three ply example in *Figure 8.4*. Reduced wrinkling offers promise in optimising production, allowing the manufacture of complex geometries at multiple times the rate as previously possible.

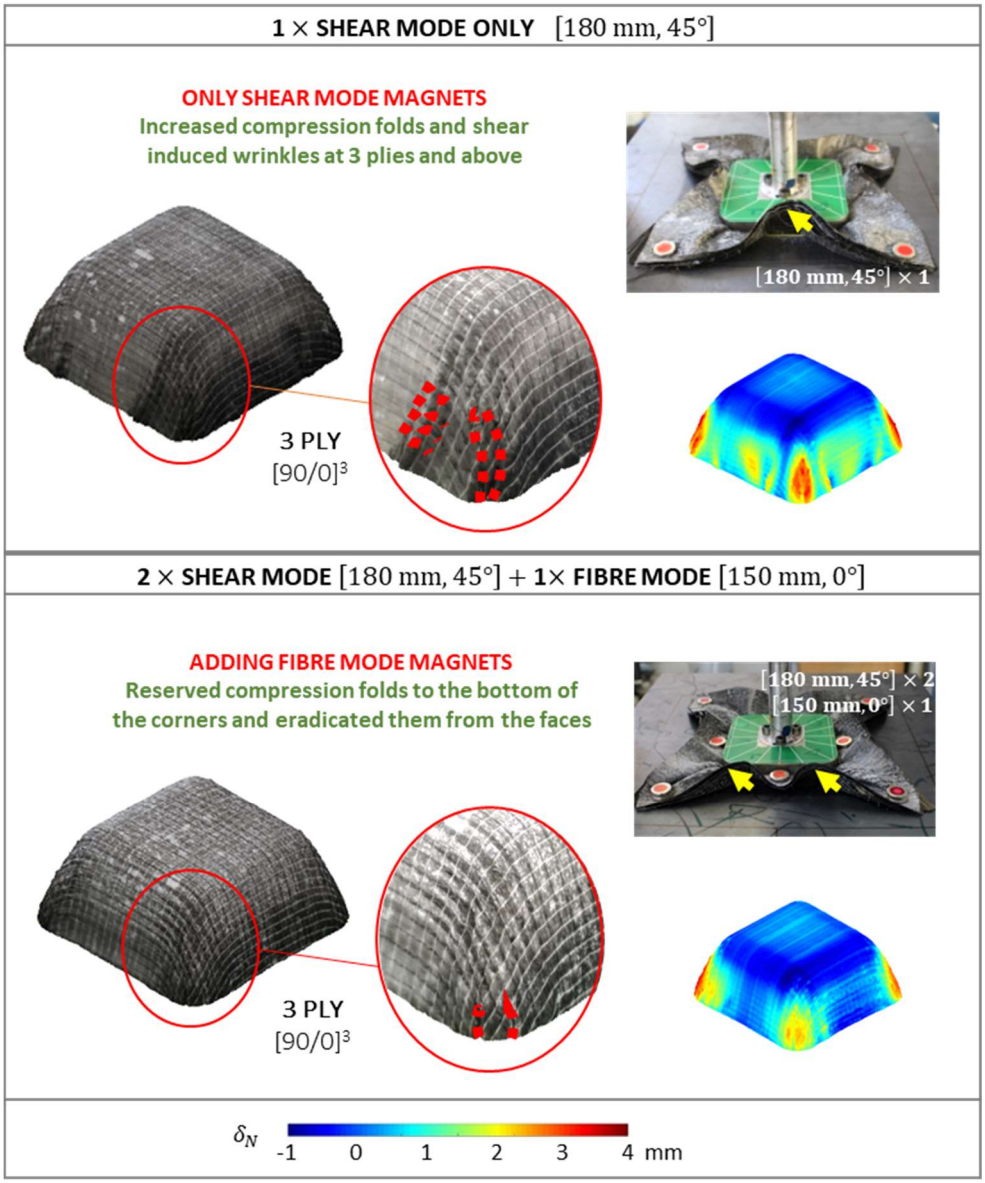

Figure 8.6: Three ply example of the increase in formability and reduction in the draw-in of defects that can be attained through adding magnets and adapted boundary conditions.

Varying fibre orientation

From the two examples shown in *Figure 8.7*, blank offsetting facilitated efficient arrangement of diverse fibre angles. Results further indicate that defects were primarily caused by compression folding. In the QI experiment, the ±45 plies are sandwiched between two $[0°, 90°]$ NCF layers, resulting in the draw-in of large sub-surface compression folds at the radius. This effect is reduced in the OS test as none of the 4 plies are duplicated. Frictional coupling of the interply region is also increased in the QI example, with the relative angle between stitch and fibre increasing the contact area. This confirms that for complex geometrical features such as corners, fibre mode deformation does not allow adequate material shearing to conform to the geometry.

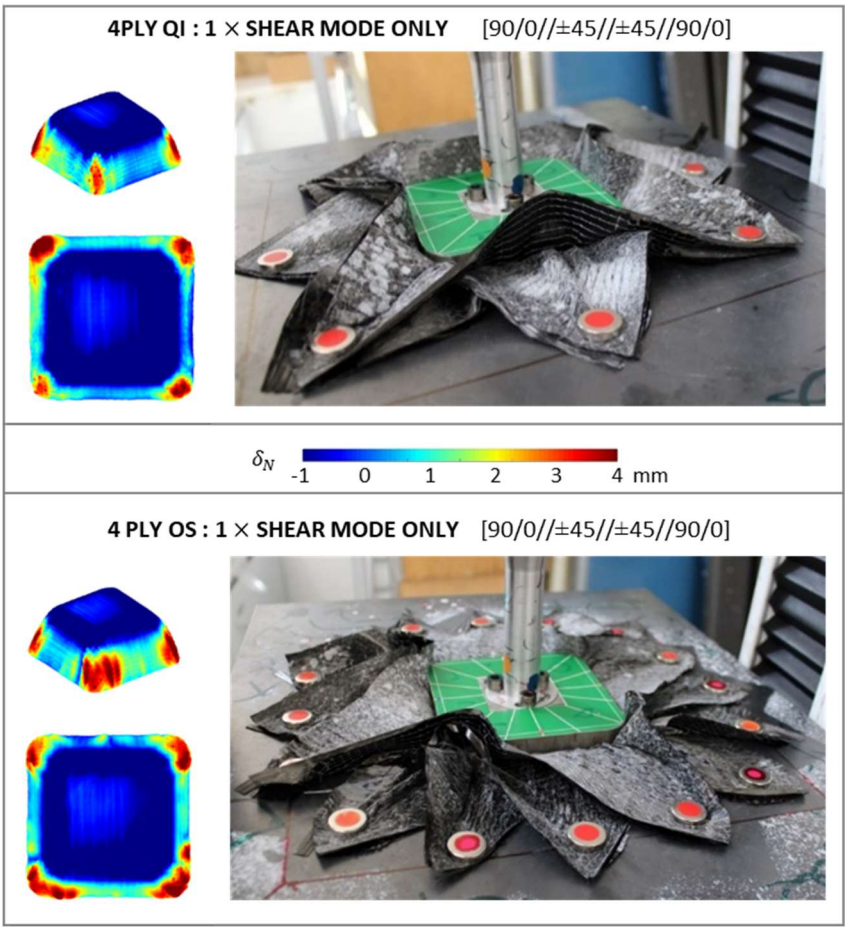

Figure 8.7: Four ply examples of varying fibre orientation highlighting process control flexibility offered through DIMAC.

However, the faces of the formed part are much better in the QI and OS examples than for four equivalent plies. Therefore, DIMAC is suitable for forming larger parts with more typical ply stacks, at a high rate. This includes aerospace parts such as large spars, secondary structures and panels.

8.4 CONCLUDING REMARKS

Distributed magnetic clamping was shown to be a viable extrinsic control measure for multiple ply forming which reinforces the flexible nature of the platform. A measure of wrinkling correlated well with observed defects and allowed comparison between different ply stacks and boundary control arrangements. The outcomes of this work are summarised below:

- Increasing the number of biaxial plies formed in one stroke is possible by adapting the boundary conditions
- Increasing the BHF by doubling the magnetic clamping force reduces shear induced wrinkling and brings our measure of conformity, δ_N, closer to zero in all cases.
- Moving to multiple plies increased the stack bending stiffness, particularly when there was a repetition of fibre angles. Using only shear mode magnets caused the draw-in of large macroscale wrinkles on the faces. Adding a second set of fibre mode magnets eradicated these wrinkles from the faces.
- Varying the fibre orientations of each biaxial ply within the stack, whilst deploying tailored boundary control, showed potential to influence individual ply deformation while retaining control over the global deformation of the material stack.
- Magnetic clamping offered a multitude of process control parameters that can be readily tailored to the forming operation. This revealed more boundary condition control than the full blank holder benchmark cases studied.

CHAPTER 9

CONCLUSIONS AND FUTURE WORK

9.1 CONCLUSIONS

Manufacture of NCF composite components suffers from a lack of process control parameters, resulting in little opportunity to influence boundary conditions during preforming. Moreover, without efficient means of tailoring material deformation, there is little gain in implementing feasible predictive models. For instance, evaluating a new geometry as only ‘formable’ or ‘un-formable’ when implementing powerful ANNs to drape forming. In this thesis, Distributed Magnetic Clamping was presented as a novel concept for widening the ‘formable’ window, producing an industrially scalable method, that can alter both local and global boundary conditions.

In an experimental study, the mechanical properties of a veiled biaxial carbon non-crimp fabric were characterised. It was found that the veil increased anisotropy in the transverse direction. This affected not only the frictional response of the material, where the veil and tricot stitch pattern influenced interface nesting, but also the out-of-plane bending stiffness. In bending, the veil was shown to act as a stiffener, impeding tow rotations when placed below the midline. Bias-extension experiments were also performed, using a rate-independent normalisation method, to evaluate the non-linear shear behaviour. Here, it was found that the peak shear stiffness was five orders of magnitude lower than the in-plane stiffness. This highlighted the energetically favourable deformation mode as a key aspect in pursuit of local process control.

Subsequent development of a macroscale FE material model implemented the deformation characteristics of the NCF in a computationally efficient approach. The streamlined model included non-linear shear stiffness and homogenised isotropic bending stiffness, in a mutually constrained shell-membrane approach, whilst also implementing high tensile stiffness in the fibre directions. Comparison of the model, with the bias-extension and cantilever experimental results, revealed the virtual representation captured the major deformation modes of the NCF.

A proof-of-concept study first explored the feasibility of applying distributed magnetic clamping to preforming. Initially on an axisymmetric hemisphere, the method investigated the influence of local adjustments to boundary conditions and revealed high levels of repeatability. It was shown that through clamping four positions that fixed the ±45° direction, wrinkling was mitigated. Further tests confirmed the material propensity to deform through intraply shear behaviour, thus facilitating this mechanism to remove excess material from double curvature and allowing the material to feed more gradually in the fibre directions.

For the first time, magnets revealed that they could effectively manipulate boundary conditions during preforming. It was shown that they offer high levels of repeatability and can be deployed in numerous ways to influence deformation. These findings are important to industrialists and academics alike, revealing a method that can be scaled up and down to a range of process methodologies.

In pursuit of developing an industrially relevant geometry, a second cubic geometry was developed. Using the initial finding of the proof-of-concept investigation, the method was developed in a parametric study for discrete geometries and quantitative analysis. Photogrammetry was deployed to generate high-fidelity 3D reconstructions of the experiments and provided a scalable sensing method that was capable of sub-mm precision. The post processing included a metric for wrinkling severity and preform quality, δ, applicable to both discrete and analytically described geometries.

A virtual process model was constructed in *Abaqus* to replicate the capabilities of the established experimental DIMAC method. The model allowed evaluation of untested clamping positions and geometries, and was implemented via an adaptable parametric python script. The model was further validated against the physical preforming trials and, in an approach that balanced accuracy and computational efficiency, was shown to accurately predict wrinkle locations and approximate wrinkle patterns.

Using the aforementioned virtual model, an optimisation framework was next established. The severity of wrinkling, δ, was predicted for a given boundary condition by deploying a Gaussian process model with a periodic kernel, to act as a surrogate. The function was updated as new information was learned about the process, to facilitate accurate predictions from the Gaussian process model. Here, this learning was achieved through Bayesian optimisation of the objective function. Bayesian optimisation was deployed to infer the sequence of tests, choosing the next boundary conditions to evaluate based on probabilistic reasoning. The results demonstrated that Bayesian optimisation could intrinsically balance exploration and exploitation of the search domain. Results were compared to the experimental findings, validating the chosen optima.

Further extension to multiple ply preforming was developed to further leverage DIMAC as a candidate for industrial development. Here, it was shown that insights established through the preceding techniques facilitated quick development and extension of the forming capabilities. The metric, δ, was adjusted to provide a robust measure of wrinkling, δ_N, to allow valid comparison of preforms with variable numbers

of plies. Through analysis of the spatial distributions, the metric was shown to correlate with observed defects and highlighted that increasing the number of biaxial plies formed in one stroke was possible. DIMAC also showed potential to influence both individual ply deformation and global deformation of the material stack. This was supported by a study that investigated varying the fibre orientations of each ply within the stack.

A novel preforming control method that harnessed predictive modelling and statistical inference was presented through the work discussed in this thesis. DIMAC demonstrated a highly repeatable method for adjustment of local boundary conditions and facilitated the creation of diverse data sets. DIMAC can be readily scaled to industrial geometries and academic investigations. Whilst other process control measures are available, few offer industry the same ease of application as magnets. Thus, the methodologies presented in this thesis precede the development of comprehensive data banks, fuelling predictive modelling capabilities of the future, whilst also improving component quality and productivity.

9.2 LIMITIATIONS

Distributed Magnetic Clamping and the associated methods presented in this thesis, carry some limitations that should be considered when developing this work. Magnets themselves offer advantageous process control during preforming, however, removing permanent magnets after forming can result in added defects if the preform is uncured. There are different options when scaling this method into industrial settings; an elegant solution is to use permeant switching magnets. Switching magnets themselves work by coupling two dipole magnets together to allow the magnetic field to be switched off mechanically. Alternatively, when considering the use of robotics and assembly automation, electromagnets could offer benefits. As the DIMAC process involves clamping around the periphery of a material blank, material wastage could be exacerbated in large parts. This can be detrimental in sustainable lean manufacturing environments, although when using dry fabrics, recycling is simpler and more efficient. This could be integrated into the process. Further consideration of industrial geometries is also necessary, with the geometries studied here having at least four transverse planes

of symmetry. While this offered many advantages in the design of the study, transferring this learning to separate features would allow further understanding of the deformation mechanics in more complex geometries. The FE model deployed in this study represented an efficient homogenisation strategy, but does not include some of the vast material anisotropy that was found during characterisation. When developing further complex forming protocols, features such as the veil, stitch and bending anisotropy could garner more realistic wrinkle morphology, although this may have a detrimental effect on computation time. The biaxial material studied in this thesis represents an exemplar aerospace NCF, further work should be conducted that looks at the effects of other material architectures and careful consideration to the deformation mechanics should be made before translating this work into bidiagonal, asymmetric shear or multiaxial fabrics.

9.3 FUTURE WORK

Future work should include an exploration of the scalability of DIMAC to industrial size components and production environments. There is also scope to investigate if it is possible to relieve process induced defects as they occur, such that clamps are placed to remove defects *during* preforming. At the same time, the ability to locally influence formability for isolated features in a large part is potentially a powerful aspect of the process – including by clamping against the tool itself or changing the clamping during the forming process.

The macroscale model implementation was efficient for process modelling, however, in more complicated forming operations this may not be sufficient to capture all preform defects. NCFs are, however, highly anisotropic. To allow feasible simulation times, there is a need to balance current computational power and modelling precision. In the current implementation, an isotropic bending model was included. A parametric study should first assess and compare the associated computational costs and gains in precision, as a result of including further anisotropy. One method that could be evaluated is global to local modelling, which would facilitate higher precision results around particular areas of concern. Similar considerations, of computational expense

and precision, will require future research to critically assess the advantages of adding frictional anisotropy or compaction behaviour.

Virtual process modelling is not the only method to apply Bayesian optimisation. One key attribute of DIMAC, is that powerful predictive modelling tools can be readily applied to experimental parametric studies. In particular, the ability to merge data sets from experiments and virtual modelling is an attractive feature and should be explored further. To unlock further potential, the wrinkling metric could also be advanced. Aspects such as wrinkle curvature and area have previously been reported, and could facilitate added statistical inference between metrics.

A further aspect to consider is that of alternative materials and material modifications. It may seem plausible that the methods in this thesis are only applicable to the specific material studied. However, through evaluating an asymmetric NCF, research should ascertain if material asymmetry can be overcome by using different clamping forces in positive and negative shear. This could dramatically increase the learning shared across different material systems, providing a process that could remove some material differences. The Distributed Magnetic Clamping process, in combination with powerful non-parametric models, could facilitate the creation of large databanks, leading to dramatically improved flexibility in design and manufacturing. Magnetic clamps have been shown to offer broad possibilities that warrant future investigation including more complex geometries, fibre angle offsetting, magnetic clamping on the tool rather than the boundary, multi-stage variable clamping, active magnetic shear actuation and diverse magnet sizes.

REFERENCES

[1] Advanced Composites Materials and their Manufacture Technology Assessment. US Deparetment of Energy. p. 9.

[2] Centea T, Grunenfelder LK, Nutt SR. A review of out-of-autoclave prepregs – Material properties, process phenomena, and manufacturing considerations. Composites Part A: Applied Science and Manufacturing. 2015;70:132-54,

[3] Ridgard C. Advances in low temperature curing prepregs for aerospace structures. SAMPE 2000: 45th International SAMPE Symposium and Exhibition2000. p. 1353-67.

[4] Repecka L, Boyd J. Vacuum-bag-only-curable prepregs that produce void-free parts. 47th International SAMPE Symposium and Exhibition2002. p. 1862-74.

[5] Mallick PK. Fiber-reinforced composites: materials, manufacturing and design. London: CRC Press - Taylor & Francis Group; 2008

[6] Steele M, Corden T, Gibbs A. The development of out-of-autoclave composite prepreg technology for aerospace applications. Proc SAMPE conf, Society for the Advancement of Material and Process Engineering. CA2002.

[7] Truong TC, Vettori M, Lomov S, Verpoest I. Carbon composites based on multi-axial multi-ply stitched preforms. Part 4. Mechanical properties of composites and damage observation. Composites Part A: applied science and manufacturing. 2005;36(9):1207-21,

[8] Goren A, Atas C. Manufacturing of polymer matrix composites using vacuum assisted resin infusion molding. Archives of materials Science and Engineering. 2008;34(2):117-20,

[9] Vallons K. The Behaviour of Carbon Fibre - Epoxy NCF Composites under Various Mechanical Loading Conditions. Leuven2009.

[10] Boisse P, Zouari B, Daniel JL. Importance of in-plane shear rigidity in finite element analyses of woven fabric composite preforming. Composites Part A. 2006;37(12):2201-12.,

[11] Erland S. Characterisation of uncured carbon fibre composites [PhD Thesis]: University of Bath; 2016.

[12] Schnabel A, Gries T. Production of non-crimp fabrics for composites. Non-Crimp Fabric Composites: Woodhead Publishing; 2011. p. 3-41.

[13] Habboush A, Sanbhal N, Shao H, Jiang J, Chen N. Characterization and Analysis of In-Plane Shear Behavior of Glass Warp-Knitted Non-Crimp Fabrics Based on Picture Frame Method. Materials. 2018;11(9):1550,

[14] Kaufmann M, Zenkert D, Åkermo M. Material selection for a curved c-spar based on cost optimization. Journal of Aircraft. 2011;48(3):797-804,

[15] Kruse F, Gries T. Standardisation of production technologies for non-crimp fabric composites. Non-Crimp Fabric Composites Woodhead Publishing; 2011. p. 42-66.

[16] Elkington M, Bloom D, Ward C, Chatzimichali A, Potter K. Hand layup: understanding the manual process. Advanced Manufacturing: Polymer & Composites Science. 2015;1(3):138-51,

[17] Ward C, Hazra K, Potter K. Development of the manufacture of complex composite panels. nternational Journal of Materials and Product Technology. 2011;42(3-4):131-55,

[18] Bhat P, Merotte J, Simacek P, S.G. A. Process analysis of compression resin transfer molding. Composites Part A: Applied science and manufacturing. 2009;40(1):431-41,

[19] Advanced Composites Materials and their Manufacture Technology Assessment. 2015.

[20] Lightfoot JS, Wisnom MR, Potter K. Defects in woven preforms: Formation mechanisms and the effects of laminate design and layup protocol. Composites Part A: Applied Science and Manufacturing. 2013;51:99-107,

[21] Chen S, McGregor OPL, Harper LT, Endruweit A, Warrior NA. Defect formation during preforming of a bi-axial non-crimp fabric with a pillar stitch pattern. Composites Part A: Applied Science and Manufacturing. 2016;91:156-67,

[22] Lomov S, Barburski M, Stoilova T, Verpoest I, Akkerman R, Loendersloot R, et al. Carbon composites based on multiaxial multiply stitched preforms. Part 3: Biaxial tension, picture frame and compression tests of the preforms. Composites Part A: Applied Science and Manufacturing. 2005;36(9):1188-206,

[23] Lee J, Hong S, Yu W, TJ K. The effect of blank holder force on the stamp forming behavior of non-crimp fabric with a chain stitch. Composites science and technology. 2007;67(3-4):357-66,

[24] Marsh G. Bombardier throws down the gauntlet with CSeries airliner. Reinforced Plastics. 2011;55(6):22-6,

[25] Roberts A. Curvature attributes and their application to 3D interpreted horizons. First break. 2001;19(2):85-100,

[26] Gauss CF. General investigations of curved surfaces. United States of America: The Princeton university library; 1902

[27] Mack C, Taylor H. The fitting of woven cloth to surfaces. Journal of the Textile institute Transactions. 1956;47(9):477-88,

[28] Bel S, Hamila N, Boisse P. Analysis of Non-Crimp Fabric Composite Reinforcements Forming. Key Engineering Materials. 2012;504:219-24,

[29] Jordan M, Mitchell T. Machine learning: Trends, perspectives, and prospects. Science. 2015;349(6245):255-60,

[30] Alpaydin E. Introduction to Machine Learning. Michigan, United States of America: MIT Press; 2009

[31] Mnih V, Kavukcuoglu K, Silver D, Graves A, Antonoglou I, Wierstra D, et al. Playing atari with deep reinforcement learning. arXiv:1312.5602; 2013.

[32] Wang Y, Soutis C. Fatigue behaviour of composite T-joints in wind turbine blade applications. Applied Composite Materials. 2017;24(2):461-75,

[33] Mulvihill DM, Smerdova O, Sutcliffe MP. Friction of carbon fibre tows. Composites Part A: Applied Science and Manufacturing. 2017;93:185-98,

[34] Ivanov DS, Lomov SV, Verpoest I. Predicting the effect of stitching on the mechanical properties and damage of non-crimp fabric composites: finite element analysis. Non-Crimp Fabric Composites: Woodhead publishing; 2011. p. 360-85.

[35] Lundström TS. The permeability of non-crimp stitched fabrics. Composites Part A: Applied Science and Manufacturing. 2000;31(12):1345-53,

[36] Long AC, Clifford MJ. Composite forming mechanisms and materials characterisation. In: Long AC, editor. Composites forming technologies. United Kingdom: Woodhead Publishing; 2014. p. 1-21.

[37] Hivet G, Duong AV. A contibution to the analyis of the intrinsic shear behavior of fabrics. Journal of Composite Materials. 2010;45(6):695-716,

[38] Milani A, Nemes J, Abeyaratne R, Holzapfel G. A method for the approximation of non-uniform fiber misalignment in textile composites using picture frame test. Composites Part A: Applied Science and Manufacturing. 2007;38(6):1493-501,

[39] Lomov S, Willems A, Verpoest I, Zhu Y, Barburski M, Stoilova T. Picture frame test of woven composite reinforcements with a full-field strain registration. Textile Research Journal. 2006;76(3):243-52,

[40] Cao J, Akkerman R, Boisse P, Chen J, Cheng H, De Graaf E, et al. Characterization of mechanical behavior of woven fabrics: Experimental methods and benchmark results. Composites Part A: Applied Science and Manufacturing. 2008;39(6):1037-53,

[41] Launay J, Hivet G, Duong A, Boisse P. Experimental analysis of the influence of tensions on in plane shear behaviour of woven composite reinforcements. Composites science and technology. 2008;68(2):506-15,

[42] Harrison P, Wiggers J, Long AC. Normalization of shear test data for rate-independent compressible fabrics. Journal of composite materials. 2008;42(22):315-2344,

[43] Potluri P, Perez Ciurezu DA, Ramgulam RB. Measurement of meso-scale shear deformations for modelling textile composites. Composites Part A: Applied Science and Manufacturing. 2006;37(2):303-14 https://doi.org/10.1016/j.compositesa.2005.03.032.

[44] Avgoulas E, Mulvihill D, Endruweit A, Sutcliffe M, Warrior N, De Focatiis D, et al. Frictional behaviour of non-crimp fabrics (NCFs) in contact with a forming tool. Tribology International. 2018;121:71-7,

[45] Åkermo M, Larberg Y, Sjölander J, Hallnader P. Influence of interply friction on the forming of stacked prepreg. 19th International Conference on Composite Materials (ICCM19). Montreal2013. p. 919-28.

[46] Larberg Y, Åkermo M. On the interply friction of different generations of carbon/epoxy prepreg systems. Composites Part A: Applied Science and Manufacturing. 2011;42(9):1067-74,

[47] Heinecke F, Willberg C. Manufacturing-Induced Imperfections in Composite Parts Manufactured via Automated Fiber Placement. Journal of Composites Science. 2019;3(2) 10.3390/jcs3020056.

[48] Liu Y-N, Yuan C, Liu C, Pan J, Dong Q. Study on the resin infusion process based on automated fiber placement fabricated dry fiber preform. Scientific Reports. 2019;9(1):7440 10.1038/s41598-019-43982-1.

[49] Zhang W, Liu F, Jiang T, Yi M, Chen W, Ding X. Overview of current design and analysis of potential theories for automated fibre placement mechanisms. Chinese Journal of Aeronautics. 2021 https://doi.org/10.1016/j.cja.2021.04.018.

[50] Culliford LE, Scarth C, Maierhofer T, Jagpal R, Rhead AT, Butler R. Discrete Stiffness Tailoring: Optimised design and testing of minimum mass stiffened panels. Composites Part B: Engineering. 2021;221:109026 https://doi.org/10.1016/j.compositesb.2021.109026.

[51] Dirk H, Ward C, Potter K. The engineering aspects of automated prepreg layup: History, present and future. Composites Part B: Engineering. 2012;43(3):997-1009,

[52] Mills A. Development of an automated preforming technology for resin infusion processing of aircraft components. Proceedings of the Institution of Mechanical Engineers, Part G: Journal of Aerospace Engineering 2006;220(5),

[53] Reinhart G, Ehinger C. Novel robot-based end-effector design for an automated preforming of limb carbon fiber textiles. Future Trends in Production Engineering. Berlin: Springer; 2013. p. 131-42.

[54] Gerngross T, Nieberl D. Automated manufacturing of large, three-dimensional CFRP parts from dry textiles. CEAS Aeronautical Journal. 2016;7(2):241-57,

[55] Eckardt M, Buchheim A, Gerngross T. Investigation of an automated dry fiber preforming process for an aircraft fuselage demonstrator using collaborating robots. CEAS Aeronautical Journal. 2016;7(3):429-40,

[56] Tai K, El-Sayed A-R, Shahriari M, Biglarbegian M, Mahmud S. State of the Art Robotic Grippers and Applications. Robotics. 2016;5(2) 10.3390/robotics5020011.

[57] Fauster E, Schillfahrt C, Hueber C, Schledjewski R. Automated profile preforming for structural components. Science and Engineering of Composite Materials. 2017;24(5):631-50 doi:10.1515/secm-2015-0377.

[58] Schillfahrt C, Fauster E, Schledjewski R. Influence of process pressures on filling behavior of tubular fabrics in bladder-assisted resin transfer molding. Advanced Manufacturing: Polymer & Composites Science. 2017;3(4):148-58 10.1080/20550340.2017.1389048.

[59] Schillfahrt C, Fauster E, Schledjewski R. A methodology for determining preform compaction in bladder-assisted resin transfer molding with elastomeric bladders for tubular composite parts. International Journal of Material Forming. 2019;12(1):1-15 10.1007/s12289-018-1398-3.

[60] Bhudolia SK, Gohel G, Leong KF, Joshi SC. Damping, impact and flexural performance of novel carbon/Elium® thermoplastic tubular composites. Composites Part B: Engineering. 2020;203:108480 https://doi.org/10.1016/j.compositesb.2020.108480.

[61] Rozant O, Bourban PE, Manson JAE. Drapability of dry textile fabrics for stampable thermoplastic preforms. Composites Part A. 2000;31(11):1167-77,

[62] Boisse P, Gasser A, Hivet G. Analyses of fabric tensile behaviour: determination of the biaxial tension–strain surfaces and their use in forming simulations. Composites Part A. 2001;32(10):1395-414,

[63] Hamila N, Boisse P. Simulations of textile composite reinforcement draping using a new semi-discrete three node finite element. Composites Part B. 2008;39(6):999-1010,

[64] Li XK, Bai SL. Sheet forming of the multi-layered biaxial weft knitted fabric reinforcement. Part I: On hemispherical surfaces. Composites Part A. 2009;40(6):766-77,

[65] Lin H, Wang J, Long AC, Clifford MJ, Harrison P. Predictive modelling for optimization of textile composite forming. Composites Science and

Technology. 2007;67(15):3242-52
https://doi.org/10.1016/j.compscitech.2007.03.040.

[66] Allaoui S, Boisse P, Chatel S, Hamila N, Hivet G, Soulat D, et al. Experimental and numerical analyses of textile reinforcement forming of a tetrahedral shape. Composites Part A. 2011;42(6):612-22,

[67] Hamila N, Boisse P, Sabourin F, Brunet M. semi-discrete shell finite element for textile composite reinforcement forming simulation. International journal for numerical methods in engineering. 2009;79(12):1443-66,

[68] Vanclooster K, Lomov SV, Verpoest I. Experimental validation of forming simulations of fabric reinforced polymers using an unsymmetrical mould configuration. Composites Part A. 2009;40(4):530-9,

[69] Khan MA, Mabrouki T, Vidal-Sallé E, Boisse P. Numerical and experimental analyses of woven composite reinforcement forming using a hypoelastic behaviour. Application to the double dome benchmark. Journal of materials processing technology,. 2010;210(2):378-88,

[70] Peng X, Rehman ZU. Textile composite double dome stamping simulation using a non-orthogonal constitutive model. Composites Science and Technology. 2011;71(8):1075-81,

[71] Zhang Z, Friedrich K. Artificial neural networks applied to polymer composites: a review. Composites Science and technology. 2003;1(63):2029-44,

[72] El Kadi H. Modeling the mechanical behavior of fiber-reinforced polymeric composite materials using artificial neural networks—A review. Composite structures. May;73(1):1-23,

[73] Zhao M, Li Z, He W. Classifying Four Carbon Fiber Fabrics via Machine Learning: A Comparative Study Using ANNs and SVM. Applied Sciences. 2016;6(8):2076-3417,

[74] Nielsen D, Pitchumani R. Intelligent model-based control of preform permeation in liquid composite molding processes, with online optimization. Composites Part A: Applied Science and Manufacturing. 2001;32(12):1789-803,

[75] Rai N, Pitchumani R. Rapid cure simulation using artificial neural networks. Composites Part A: Applied Science and Manufacturing. 1997;28(9-10):847-59,

[76] Erzurumlu T, Oktem H. omparison of response surface model with neural network in determining the surface quality of moulded parts. Materials & design. 2007 28(2):459-65,

[77] Heider D, Piovoso MJ, Gillespie Jr JW. Application of a neural network to improve an automated thermoplastic tow-placement process. Journal of Process Control. 2001;12(1):101-11,

[78] Long A, Souter B, Robitaille F, CD R. Effects of fibre architecture on reinforcement fabric deformation Plastics, rubber and composites. 2002;31(2):87-97,

[79] Long A, Souter B, Robitaille F, CD R. Effects of fibre architecture on deformation during preform manufacture. Advanced Composites Letters. 1999;8(6):333-44,

[80] Yu WR, Harrison P, Long A. Finite element forming simulation for non-crimp fabrics using a non-orthogonal constitutive equation. Composites Part A: Applied Science and Manufacturing. 2005;36(8):1079-93,

[81] Tanaka K, Ushiyama R, Katayama T, Enoki S, Sakamoto H. Formability evaluation of carbon fiber NCF by a non-contact 3D strain measurement system and the effects of blank holder force on its formability. WIT Transactions on The Built Environment. 2014;137:317-26,

[82] Wieleba W. The statistical correlation of the coefficient of friction and wear rate of PTFE composites with steel counterface roughness and hardness. Wear. 2002;252(9-10):719-29,

[83] Boisse P, Colmars J, Hamila N, Naouar N, Steer Q. Bending and wrinkling of composite fiber preforms and prepregs. A review and new developments in the draping simulations. Composites Part B: Engineering. 2018;141:234-49 https://doi.org/10.1016/j.compositesb.2017.12.061.

[84] BS EN ISO 9073-7:1998: Textiles. Test methods for nonwovens. Determination of bending length. British Standards Institute; 1998.

[85] de Bilbao E, Soulat D, Hivet G, Gasser A. Experimental Study of Bending Behaviour of Reinforcements. Experimental Mechanics. 2010;50(3):333-51 10.1007/s11340-009-9234-9.

[86] Yu F, Chen S, Viisainen JV, Sutcliffe MPF, Harper LT, Warrior NA. A macroscale finite element approach for simulating the bending behaviour of biaxial fabrics. Composites Science and Technology. 2020;191:108078 https://doi.org/10.1016/j.compscitech.2020.108078.

[87] Harrison P. Modelling the forming mechanics of engineering fabrics using a mutually constrained pantographic beam and membrane mesh. Composites Part A: Applied Science and Manufacturing. 2016;81:145-57 https://doi.org/10.1016/j.compositesa.2015.11.005.

[88] Yu F, Chen S, Harper LT, Warrior NA. Simulating the effect of fabric bending stiffness on the wrinkling behaviour of biaxial fabrics during preforming. Composites Part A: Applied Science and Manufacturing. 2021;143:106308 https://doi.org/10.1016/j.compositesa.2021.106308.

[89] Harrison P, Alvarez MF, Anderson D. Towards comprehensive characterisation and modelling of the forming and wrinkling mechanics of engineering fabrics.

International Journal of Solids and Structures. 2018;154:2-18 https://doi.org/10.1016/j.ijsolstr.2016.11.008.

[90] Harrison P, Härtel F. Corrigendum to 'Evaluation of normalisation methods for uniaxial bias extension tests on engineering fabrics'. Composites Part A: Applied Science and Manufacturing. 2016;80:104-6 https://doi.org/10.1016/j.compositesa.2015.10.013.

[91] Härtel F, Harrison P. Evaluation of normalisation methods for uniaxial bias extension tests on engineering fabrics. Composites Part A: Applied Science and Manufacturing. 2014;67:61-9 https://doi.org/10.1016/j.compositesa.2014.08.011.

[92] Schneider CA, Rasband WS, Eliceiri KW. NIH Image to ImageJ: 25 years of image analysis. Nature Methods. 2012;9(7):671-5 10.1038/nmeth.2089.

[93] Chen S, Harper LT, Endruweit A, Warrior NA. Formability optimisation of fabric preforms by controlling material draw-in through in-plane constraints. Composites Part A: Applied Science and Manufacturing. 2015;76:10-9 https://doi.org/10.1016/j.compositesa.2015.05.006.

[94] Chen S, Endruweit A, Harper LT, Warrior NA. Inter-ply stitching optimisation of highly drapeable multi-ply preforms. Composites Part A: Applied Science and Manufacturing. 2015;71:144-56 https://doi.org/10.1016/j.compositesa.2015.01.016.

[95] Yu F, Chen S, Harper LT, Warrior NA. Double diaphragm forming simulation using a global-to-local modelling strategy for detailed defect detection in large structures. Composites Part A: Applied Science and Manufacturing. 2021;147:106457 https://doi.org/10.1016/j.compositesa.2021.106457.

[96] Zimmerling C, Dörr D, Henning F, Kärger L. A machine learning assisted approach for textile formability assessment and design improvement of composite components. Composites Part A: Applied Science and Manufacturing. 2019;124:105459 https://doi.org/10.1016/j.compositesa.2019.05.027.

[97] Schirmaier FJ, Dörr D, Henning F, Kärger L. A macroscopic approach to simulate the forming behaviour of stitched unidirectional non-crimp fabrics (UD-NCF). Composites Part A: Applied Science and Manufacturing. 2017;102:322-35 https://doi.org/10.1016/j.compositesa.2017.08.009.

[98] Thompson AJ, Belnoue JPH, Hallett SR. Modelling defect formation in textiles during the double diaphragm forming process. Composites Part B: Engineering. 2020;202:108357 https://doi.org/10.1016/j.compositesb.2020.108357.

[99] Pfrommer J, Zimmerling C, Liu J, Kärger L, Henning F, Beyerer J. Optimisation of manufacturing process parameters using deep neural networks as surrogate

models. Procedia CIRP. 2018;72:426-31 https://doi.org/10.1016/j.procir.2018.03.046.

[100] Boisse P, Hamila N, Helenon F, Hagege B, Cao J. Different approaches for woven composite reinforcement forming simulation. International Journal of Material Forming. 2008;1(1):21-9 10.1007/s12289-008-0002-7.

[101] Bussetta P, Correia N. Numerical forming of continuous fibre reinforced composite material: A review. Composites Part A: Applied Science and Manufacturing. 2018;113:12-31 https://doi.org/10.1016/j.compositesa.2018.07.010.

[102] Boisse P, Hamila N, Vidal-Sallé E, Dumont F. Simulation of wrinkling during textile composite reinforcement forming. Influence of tensile, in-plane shear and bending stiffnesses. Composites Science and Technology. 2011;71(5):683-92 https://doi.org/10.1016/j.compscitech.2011.01.011.

[103] Peng X, Rehman ZU. Textile composite double dome stamping simulation using a non-orthogonal constitutive model. Composites Science and Technology. 2011;71(8):1075-81 https://doi.org/10.1016/j.compscitech.2011.03.010.

[104] Liang B, Boisse P. A review of numerical analyses and experimental characterization methods for forming of textile reinforcements. Chinese Journal of Aeronautics. 2021;34(8):143-63 https://doi.org/10.1016/j.cja.2020.09.027.

[105] Dangora LM, Mitchell CJ, Sherwood JA. Predictive model for the detection of out-of-plane defects formed during textile-composite manufacture. Composites Part A: Applied Science and Manufacturing. 2015;78:102-12 https://doi.org/10.1016/j.compositesa.2015.07.011.

[106] Bel S, Hamila N, Boisse P, Dumont F. Finite element model for NCF composite reinforcement preforming: Importance of inter-ply sliding. Composites Part A: Applied Science and Manufacturing. 2012;43(12):2269-77 https://doi.org/10.1016/j.compositesa.2012.08.005.

[107] Boisse P, Hamila N, Guzman-Maldonado E, Madeo A, Hivet G, dell'Isola F. The bias-extension test for the analysis of in-plane shear properties of textile composite reinforcements and prepregs: a review. International Journal of Material Forming. 2017;10(4):473-92 10.1007/s12289-016-1294-7.

[108] Samir D, Hamid S. Determination of the in-plane shear rigidity modulus of a carbon non-crimp fabric from bias-extension data test. Journal of Composite Materials. 2013;48(22):2729-36 10.1177/0021998313502063.

[109] Chen S, McGregor OPL, Harper LT, Endruweit A, Warrior NA. Optimisation of local in-plane constraining forces in double diaphragm forming. Composite Structures. 2018;201:570-81 https://doi.org/10.1016/j.compstruct.2018.06.062.

[110] Nosrat-Nezami F, Gereke T, Eberdt C, Cherif C. Characterisation of the shear–tension coupling of carbon-fibre fabric under controlled membrane tensions for precise simulative predictions of industrial preforming processes. Composites Part A: Applied Science and Manufacturing. 2014;67:131-9 https://doi.org/10.1016/j.compositesa.2014.08.030.

[111] Komeili M, Milani AS. On effect of shear-tension coupling in forming simulation of woven fabric reinforcements. Composites Part B: Engineering. 2016;99:17-29 https://doi.org/10.1016/j.compositesb.2016.05.004.

[112] Zimmerling C, Poppe C, Kärger L. Estimating Optimum Process Parameters in Textile Draping of Variable Part Geometries - A Reinforcement Learning Approach. Procedia Manufacturing. 2020;47:847-54 https://doi.org/10.1016/j.promfg.2020.04.263.

[113] Khan MA, Mabrouki T, Vidal-Sallé E, Boisse P. Numerical and experimental analyses of woven composite reinforcement forming using a hypoelastic behaviour. Application to the double dome benchmark. Journal of Materials Processing Technology. 2010;210(2):378-88 https://doi.org/10.1016/j.jmatprotec.2009.09.027.

[114] Dassault Systèmes S. Shell Section Behavior. Dassault Systèmes Abaqus 2017 Documentation. 2017,

[115] Yu W-R, Harrison P, Long A. Finite element forming simulation for non-crimp fabrics using a non-orthogonal constitutive equation. Composites Part A: Applied Science and Manufacturing. 2005;36(8):1079-93 https://doi.org/10.1016/j.compositesa.2005.01.007.

[116] Middendorf P, Metzner C. 18 - Aerospace applications of non-crimp fabric composites. Non-Crimp Fabric Composites: Woodhead Publishing; 2011. p. 441-9.

[117] Sköck-Hartmann B, Gries T. 20 - Automotive applications of non-crimp fabric composites. Non-Crimp Fabric Composites: Woodhead Publishing; 2011. p. 461-80.

[118] Chen S, Harper LT, Endruweit A, Warrior NA. Optimisation of forming process for highly drapeable fabrics. 20th International Conference on Composite Materials2015.

[119] Jagpal R, Butler R, Loukaides EG. Towards flexible and defect-free forming of composites through distributed clamping. Procedia CIRP. 2019;85:341-6 https://doi.org/10.1016/j.procir.2019.09.008.

[120] Nosrat Nezami F, Gereke T, Cherif C. Active forming manipulation of composite reinforcements for the suppression of forming defects. Composites Part A: Applied Science and Manufacturing. 2017;99:94-101 https://doi.org/10.1016/j.compositesa.2017.04.011.

[121] Dutta S, Körber M, Frommel C. Automated fixation of dry carbon fibre fabrics with RTM6 for autonomous draping and sensor-aided preforming. Procedia CIRP. 2019;85:329-34 https://doi.org/10.1016/j.procir.2019.10.007.

[122] Nash NH, Young TM, Stanley WF. The influence of a thermoplastic toughening interlayer and hydrothermal conditioning on the Mode-II interlaminar fracture toughness of Carbon/Benzoxazine composites. Composites Part A: Applied Science and Manufacturing. 2016;81:111-20 https://doi.org/10.1016/j.compositesa.2015.11.010.

[123] Schnabel A, Gries T. 1 - Production of non-crimp fabrics for composites. In: Lomov SV, editor. Non-Crimp Fabric Composites: Woodhead Publishing; 2011. p. 3-41.

[124] Long A, Souter B, Robitaille F, Rudd C. Effects of fibre architecture on deformation during preform manufacture. Advanced Composites Letters. 1999;8(6):333-44 https://doi.org/10.1177/096369359900800608.

[125] Long AC, Souter BJ, Robitaille F, Rudd CD. Effects of fibre architecture on reinforcement fabric deformation. Plastics, Rubber and Composites. 2002;31(2):87-97 10.1179/146580102225001391.

[126] Lee JS, Hong SJ, Yu W-R, Kang TJ. The effect of blank holder force on the stamp forming behavior of non-crimp fabric with a chain stitch. Composites Science and Technology. 2007;67(3):357-66 https://doi.org/10.1016/j.compscitech.2006.09.009.

[127] Amirkhosravi M, Pishvar M, Altan MC. Void reduction in VARTM composites by compaction of dry fiber preforms with stationary and moving magnets. Journal of Composite Materials. 2018;53(6):769-82 https://doi.org/10.1177/0021998318791311.

[128] Harrison P, Gonzalez Camacho LF. Deep draw induced wrinkling of engineering fabrics. International Journal of Solids and Structures. 2021;212:220-36 https://doi.org/10.1016/j.ijsolstr.2020.12.003.

[129] Jagpal R, Evangelou E, Butler R, Loukaides EG. Multiple ply preforming of non-crimp fabrics with distributed magnetic clamping. Composites Communications. 2022;31:101107 https://doi.org/10.1016/j.coco.2022.101107.

[130] Jagpal R, Evangelou, E., Butler, R., Loukaides, E. Preforming of non-crimp fabrics with distributed magnetic clamping and Bayesian optimisation. Journal of Composite Materials. 2022;56(18) https://doi.org/10.1177/00219983221103637.

[131] Chen Y, Jagpal R, Loukaides E. Assessment and case studies of UAV photogrammetry for manufacturing applications. International Journal of Mechatronics and Manufacturing Systems. 2022,

[132] Amiri PJ, Gruen A, Cozzani A. High accuracy space structures monitoring by a close-range photogrammetric network. International Archives of the Photogrammetry, Remote Sensing and Spatial Information Sciences. 2006;36(5):236-41,

[133] Fraser CS, Woods A, Brizzi D. Hyper redundancy for accuracy enhancement in automated close range photogrammetry. The Photogrammetric Record. 2005;20(111):205-17 https://doi.org/10.1111/j.1477-9730.2005.00327.x.

[134] Luhmann T. Close range photogrammetry for industrial applications. ISPRS Journal of Photogrammetry and Remote Sensing. 2010;65(6):558-69 https://doi.org/10.1016/j.isprsjprs.2010.06.003.

[135] Setiyadi S, Mukhtar H, Cahyadi WA. A Comparative Study of Affordable Photogrammetry Software for Reconstructing 3D Model of a Human Foot. 2021 IEEE 7th International Conference on Smart Instrumentation, Measurement and Applications (ICSIMA): IEEE; 2021. p. 286-91.

[136] Vacca G. Overview of open source software for close range photogrammetry. 2019 Free and Open Source Software for Geospatial, FOSS4G 2019: International Society for Photogrammetry and Remote Sensing; 2019. p. 239-45.

[137] Johnson KJ, Butler R, Loukaides EG, Scarth C, Rhead AT. Stacking sequence selection for defect-free forming of uni-directional ply laminates. Composites Science and Technology. 2019;171:34-43 https://doi.org/10.1016/j.compscitech.2018.11.048.

[138] Giaccari L. Surface Reconstruction from scattered points cloud (open surfaces). MATLAB Central File Exchange; 2017.

[139] Tuszynski J. Triangle/Ray Intersection. MATLAB Central File Exchange; 2018.

[140] Elkington M, Bloom D, Ward C, Chatzimichali A, Potter K. Hand layup: understanding the manual process. Advanced Manufacturing: Polymer & Composites Science. 2015;1(3):138-51 https://doi.org/10.1080/20550340.2015.1114801.

[141] Chuaqui T, Rhead A, Butler R, Scarth C. A data-driven Bayesian optimisation framework for the design and stacking sequence selection of increased notched strength laminates. Composites Part B: Engineering. 2021;226:109347,

[142] Zhang W, Bostanabad R, Liang B, Su X, Zeng D, Bessa MA, et al. A numerical Bayesian-calibrated characterization method for multiscale prepreg preforming simulations with tension-shear coupling. Composites Science and Technology. 2019;170:15-24 https://doi.org/10.1016/j.compscitech.2018.11.019.

[143] Zhang Y, Apley DW, Chen W. Bayesian Optimization for Materials Design with Mixed Quantitative and Qualitative Variables. Scientific Reports. 2020;10(1):4924 https://doi.org/10.1038/s41598-020-60652-9.

[144] Matveev MY, Endruweit A, Long AC, Iglesias MA, Tretyakov MV. Bayesian inversion algorithm for estimating local variations in permeability and porosity of reinforcements using experimental data. Composites Part A: Applied Science and Manufacturing. 2021;143:106323 https://doi.org/10.1016/j.compositesa.2021.106323.

[145] Greenhill S, Rana S, Gupta S, Vellanki P, Venkatesh S. Bayesian Optimization for Adaptive Experimental Design: A Review. IEEE Access. 2020;8:13937-48 https://doi.org/10.1109/ACCESS.2020.2966228.

[146] Rasmussen CE, Williams CKI. Gaussian Processes for Machine Learning. The MIT Press; 2005.

[147] Shahriari B, Swersky K, Wang Z, Adams RP, Freitas Nd. Taking the Human Out of the Loop: A Review of Bayesian Optimization. Proceedings of the IEEE. 2016;104(1):148-75 10.1109/JPROC.2015.2494218.

[148] Avgoulas EI, Mulvihill DM, Endruweit A, Sutcliffe MPF, Warrior NA, De Focatiis DSA, et al. Frictional behaviour of non-crimp fabrics (NCFs) in contact with a forming tool. Tribology International. 2018;121:71-7 https://doi.org/10.1016/j.triboint.2018.01.026.

[149] Yousaf Z, Potluri P, Withers PJ. Influence of Tow Architecture on Compaction and Nesting in Textile Preforms. Applied Composite Materials. 2017;24(2):337-50 https://doi.org/10.1007/s10443-016-9554-8.

[150] Viisainen JV, Hosseini A, Sutcliffe MPF. Experimental investigation, using 3D digital image correlation, into the effect of component geometry on the wrinkling behaviour and the wrinkling mechanisms of a biaxial NCF during preforming. Composites Part A: Applied Science and Manufacturing. 2021;142:106248 https://doi.org/10.1016/j.compositesa.2020.106248.

[151] Di Francesco M, Hopcraft C, Veldenz L, Giddings P. Preforming Large Composite Aerostructures: A Unique UK Capability. Paper presented at SAMPE Europe Conference 2018, Southampton, United Kingdom. 2018.

[152] Allaoui S, Cellard C, Hivet G. Effect of inter-ply sliding on the quality of multilayer interlock dry fabric preforms. Composites Part A: Applied Science and Manufacturing. 2015;68:336-45 https://doi.org/10.1016/j.compositesa.2014.10.017.

[153] Guzman-Maldonado E, Wang P, Hamila N, Boisse P. Experimental and numerical analysis of wrinkling during forming of multi-layered textile composites. Composite Structures. 2019;208:213-23 https://doi.org/10.1016/j.compstruct.2018.10.018.

[154] CloudCompare. 2.11.3 Anoia ed2020.